

# Incorporating the Loading Dependence of the Maxwell–Stefan Diffusivity in the Modeling of CH<sub>4</sub> and CO<sub>2</sub> Permeation Across Zeolite Membranes

R. Krishna,\*† J. M. van Baten,† E. García-Pérez,‡ and S. Calero‡

*Van't Hoff Institute for Molecular Sciences, University of Amsterdam, Nieuwe Achtergracht 166, 1018 WV Amsterdam, The Netherlands, and Department of Environmental Sciences, University Pablo de Olavide, Ctra de Utrera, Km1, 41013 Seville, Spain*

Molecular dynamics (MD) simulations were carried out in order to gain some generic insights into the loading dependence of the Maxwell–Stefan (MS) diffusivity  $\bar{D}_i$  of CH<sub>4</sub> and CO<sub>2</sub> in different zeolite topologies that can be divided into three classes consisting of (a) intersecting channels, (b) one-dimensional channels, and (c) cages separated by windows. The MD simulations demonstrate that  $\bar{D}_i$  is generally loading dependent and reduces to zero at saturation loading. Furthermore, the loading dependence of  $\bar{D}_i$  shows a qualitatively different trend for CO<sub>2</sub> than for CH<sub>4</sub>. The loading dependence of the MS diffusivity is described using the model of Reed and Ehrlich (*Surf. Sci.* **1981**, *102*, 588–609), which accounts for the reduction in the energy barrier for hopping of molecules between adsorption sites due to intermolecular interactions. A unary permeation model accounting for the loading dependence is developed, and published data on permeation of CH<sub>4</sub> and CO<sub>2</sub> across MFI, CHA, and DDR membranes are used for quantitative validation. Implications for mixture permeation are also discussed.

## 1. Introduction

Zeolite membranes are growing in importance in view of several emerging separation and reaction applications in the process industries.<sup>1</sup> The separation of CO<sub>2</sub> and CH<sub>4</sub> mixtures is an example of one such application.<sup>2–4</sup> For economical separations, CH<sub>4</sub> needs to be retained at high pressures; consequently, the molecular loadings within the zeolite are expected to be high. The permeation fluxes are determined both by the adsorption and diffusion characteristics of CO<sub>2</sub> and CH<sub>4</sub> in the zeolites. In recent years, molecular dynamics (MD) simulations have been carried out to study the loading dependence of the MS diffusivity  $\bar{D}_i$  for a variety of alkanes in several different zeolite structures.<sup>5–14</sup> Some MD simulation results are also available for the diffusion of N<sub>2</sub> and CO<sub>2</sub> in MFI zeolite.<sup>15</sup> All these simulations indicate that  $\bar{D}_i$  is generally a strong function of the occupancy within the zeolite.

Three recent publications have presented valuable data on permeation fluxes of both pure components CO<sub>2</sub> and CH<sub>4</sub>, along with their mixtures, in DDR,<sup>2</sup> CHA (in the form of its isotype SAPO-34),<sup>3</sup> and MFI (silicalite-1).<sup>4</sup> The papers by Li et al.<sup>3</sup> and Zhu et al.<sup>4</sup> also attempt to model their permeation experiments using the Maxwell–Stefan (MS) equations;<sup>16–18</sup> in both papers, the MS diffusivity  $\bar{D}_i$  is assumed to be independent of the loading  $q_i$ . The comparisons between the experimental and model predictions of the permeation fluxes through CHA membrane at 295 K at varying upstream pressures presented by Li et al.<sup>3</sup> in Figure 6 of their paper are particularly interesting. There is poor agreement between the MS permeation model for CH<sub>4</sub>, both for the pure component and in the 50–50 mixture, while for CO<sub>2</sub>, the agreement is good in both cases. The first objective of this paper is to reanalyze these permeation experiments in order to demonstrate that the  $\bar{D}_i$  of CH<sub>4</sub> in CHA

is strongly loading dependent; this is shown to be the root cause of the increasing deviations between model predictions and experimental permeation fluxes with increasing upstream pressures, as presented in Figure 6 of Li et al.<sup>3</sup> Using the Tomita et al.<sup>2</sup> experimental results, we shall show that the MS diffusivity of CH<sub>4</sub> in DDR is even more strongly loading dependent than that in CHA. The corresponding analysis of CO<sub>2</sub> permeation across CHA and DDR shows that the assumption of loading-independent  $\bar{D}_i$  is a reasonable one. For a proper analysis of the published permeation experimental data,<sup>2–4</sup> it is essential to have reliable data on the adsorption isotherm *up to* saturation limits; the required sorption data for CH<sub>4</sub> and CO<sub>2</sub> were determined by Grand Canonical Monte Carlo (GCMC) simulations.

The second objective of this paper is to attempt to gain some generic insights into the loading dependence of  $\bar{D}_i$  of CH<sub>4</sub> and CO<sub>2</sub> in different zeolite topologies by use of MD simulations. The third objective of this paper is to develop a model of unary permeation that takes account of the  $\bar{D}_i$ – $q_i$  dependence using the model developed by Reed and Ehrlich<sup>19</sup> as a basis. Experimentally measured CH<sub>4</sub> and CO<sub>2</sub> permeation fluxes<sup>2–4</sup> for MFI, DDR, and CHA are used to validate the developed model. The GCMC and MD simulation details, including snapshots showing location of CH<sub>4</sub> and CO<sub>2</sub> molecules within the zeolites, along with the detailed derivation of the unary permeation model, have been included in the Supporting Information accompanying this publication.

## 2. Analysis of CH<sub>4</sub> Permeation across Zeolites

We first analyze the pure CH<sub>4</sub> permeation experiments at 303 K in MFI zeolite as reported by Zhu et al.<sup>4</sup> Figure 1a compares the GCMC simulated isotherm with the experimental isotherm data of Zhu et al.<sup>4</sup> The GCMC simulation data are obtained in terms of fugacities, and these are plotted on the *x*-axis, rather than pressures. Up to the range of fugacities used in the experimental isotherms, 1 MPa, there is good agreement

\* Corresponding author. Fax: +31 205255604. E-mail: r.krishna@uva.nl  
† University of Amsterdam.

‡ University Pablo de Olavide.

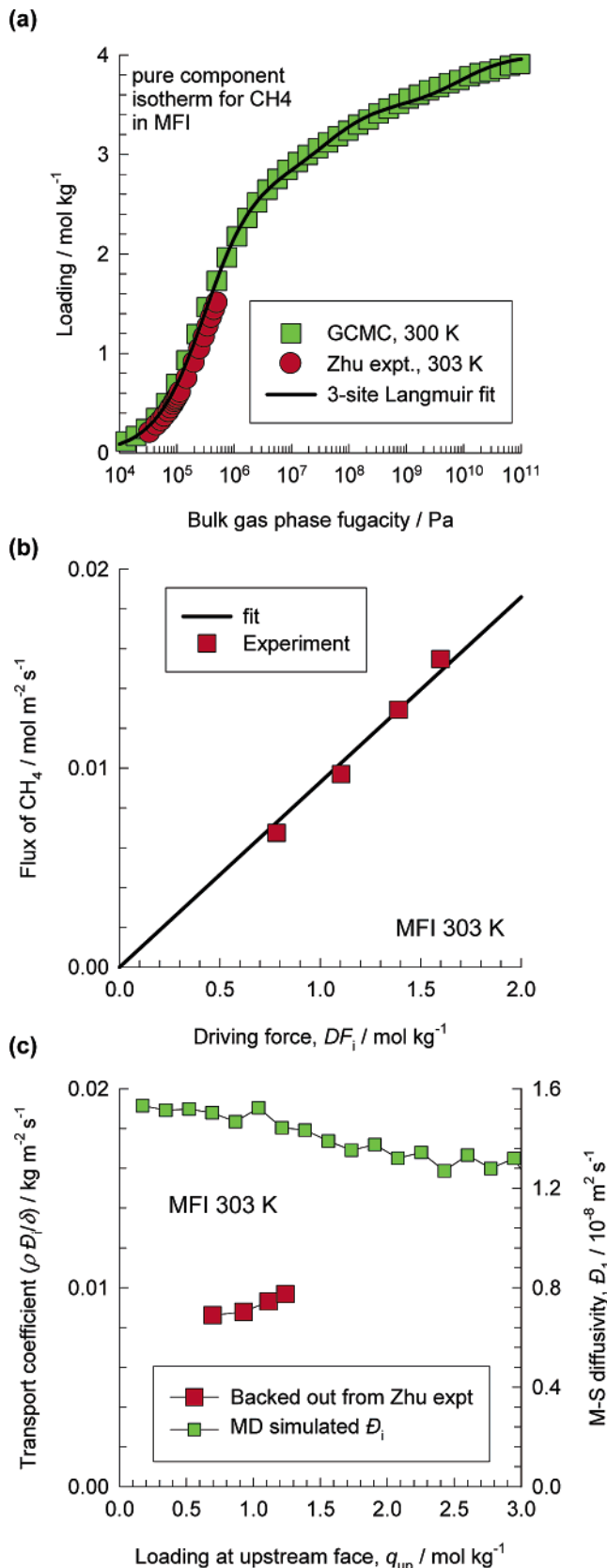


**Figure 1.** (a) Sorption isotherm data for CH<sub>4</sub> in MFI at 303 K. The GCMC simulation results are compared with the experimental data of Zhu et al.<sup>4</sup> Also shown by the continuous line is the three-site Langmuir fit of the GCMC simulated isotherm. (b) The experimental data<sup>4</sup> on permeation flux of CH<sub>4</sub> is plotted against the driving force DF<sub>i</sub>, calculated from eq 3. The straight line in (b) has been drawn taking the fitted value of ρΔ<sub>i</sub>/δ indicated in Table 3. (c) Transport coefficients ρΔ<sub>i</sub>/δ, backed out using eq 2, are shown as a function of the loadings at the upstream face of the membrane, q<sub>up</sub>. Also plotted in (c) are the MD simulated Δ<sub>i</sub> (right y-axis).

between the experiments and the GCMC simulations. The GCMC data could be fitted with a three-site Langmuir model,

$$q_i = \frac{q_{i,\text{sat},A} b_{i,A} f_i}{1 + b_{i,A} f_i} + \frac{q_{i,\text{sat},B} b_{i,B} f_i}{1 + b_{i,B} f_i} + \frac{q_{i,\text{sat},C} b_{i,C} f_i}{1 + b_{i,C} f_i} \quad (1)$$

The values of the fit parameters are given in Table 1. The total saturation capacity  $q_{i,\text{sat}} = q_{i,\text{sat},A} + q_{i,\text{sat},B} + q_{i,\text{sat},C} = 4 \text{ mol kg}^{-1}$  is higher than the value of 2.69 used in the single-site Langmuir fit of Zhu et al.<sup>4</sup> Golden and Sircar<sup>20</sup> discuss the multisite nature of the adsorption process in MFI and the pitfalls in adopting a simple single-site Langmuir model. The precise identification, and location, of the adsorption sites is a complex issue and has been investigated in some detail by Beerdse et al.<sup>11</sup> It is to be noted that, for relatively small molecules such as CH<sub>4</sub>, N<sub>2</sub>, CO<sub>2</sub>, it is not possible to determine the saturation capacity from experimental data on adsorption isotherms. The reason for this is that the pressures required to achieve saturation of the pores within the zeolite are of the order of 10<sup>9</sup> Pa, a value that cannot be approached experimentally. At these pressures, the adsorbent is present in the liquid phase, and therefore, the saturation capacity can be estimated from information on the pore volume and the molar volume of the liquid phase. An alternative approach, as followed in this paper, is to perform GCMC simulations to high enough pressures (strictly fugacities) till saturation is achieved.

If the MS diffusivity in MFI can be taken to be loading independent, we may write the permeation flux as (see Appendix C of Supporting Information for derivation)

$$N_i = \frac{\rho \Delta_i}{\delta} DF_i \quad (2)$$

where DF<sub>i</sub> is the driving force defined as

$$DF_i = q_{i,\text{sat},A} \ln\left(\frac{1 + b_{i,A} f_{i,\text{up}}}{1 + b_{i,A} f_{i,\text{down}}}\right) + q_{i,\text{sat},B} \ln\left(\frac{1 + b_{i,B} f_{i,\text{up}}}{1 + b_{i,B} f_{i,\text{down}}}\right) + q_{i,\text{sat},C} \ln\left(\frac{1 + b_{i,C} f_{i,\text{up}}}{1 + b_{i,C} f_{i,\text{down}}}\right) \quad (3)$$

Figure 1b shows that the experimental permeation flux N<sub>i</sub> varies almost linearly with DF<sub>i</sub>, consistent with the assumption of a constant value of ρΔ<sub>i</sub>/δ = 0.0093. Figure 1c shows the values of the membrane transport coefficients, ρΔ<sub>i</sub>/δ backed out from each experimental point using eqs 2 and 3. We choose to back out ρΔ<sub>i</sub>/δ from the experimental permeation data rather than the diffusivities Δ<sub>i</sub> because of the uncertainties in the determination of the membrane thicknesses used in the permeation experiments.<sup>2-4</sup> The results presented in parts b and c of Figure 1 appear to confirm the validity of the constant Δ<sub>i</sub> assumption for MFI, at least for  $q_{i,\text{up}} < 1.5 \text{ mol/kg}$ .

We turn to analysis of CH<sub>4</sub> permeation in CHA, in the form of its isotype SAPO-34. The GCMC simulation results for the sorption isotherm with all-silica CHA are compared in Figure 2a with the experimental isotherm reported by Li et al.<sup>21</sup> for SAPO-34. The experimental isotherm data is only available up to a pressure of 120 kPa, and there is good agreement with the GCMC simulations for this range. The GCMC simulated isotherms were fitted with the three-site Langmuir model with parameters specified in Table 1. The saturation capacity  $q_{i,\text{sat}} = q_{i,\text{sat},A} + q_{i,\text{sat},B} + q_{i,\text{sat},C} = 8.32 \text{ mol/kg}$  is significantly higher than the value obtained in the single-site Langmuir fit value of 2.7 mol/kg used by Li et al.<sup>21</sup> In Figure 2b, the permeation fluxes reported by Li et al.<sup>3</sup> are plotted against the DF<sub>i</sub> calculated using

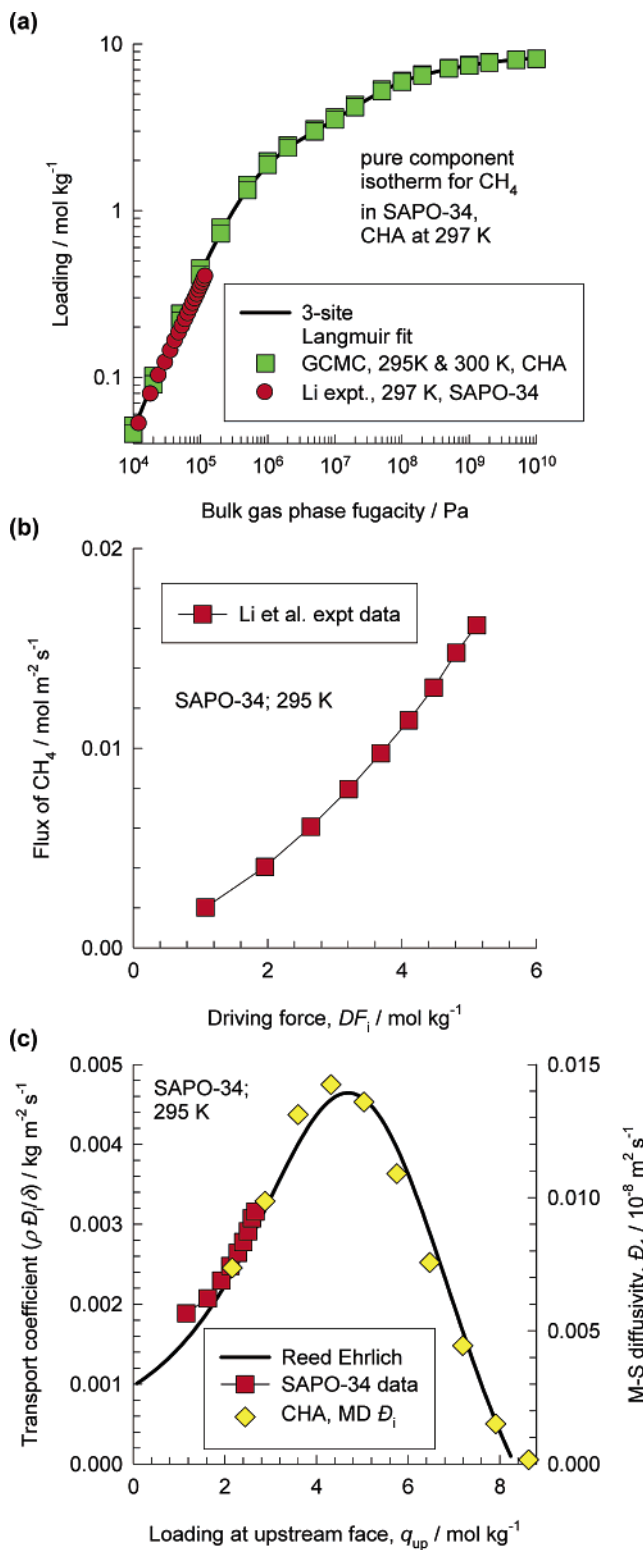


**Figure 2.** (a) Sorption isotherm data for CH<sub>4</sub> in CHA at 297 K. The GCMC simulation results are compared with the experimental data of Li et al.<sup>21</sup> Also shown by the continuous line is the three-site Langmuir fit of the GCMC simulated isotherm. (b) The experimental data<sup>3</sup> on permeation flux of CH<sub>4</sub> is plotted against the driving force DF<sub>i</sub>, calculated from eq 3. (c) Transport coefficients ρΦ/δ, backed out using eq 2, are shown as a function of the loadings at the upstream face of the membrane, q<sub>i,up</sub>. Also plotted in (c) are the MD simulated Φ<sub>i</sub> (right y-axis). The continuous solid line in (c) is drawn with the Reed and Ehrlich parameters listed in Table 2.

eq 3. It is clear that a linear fit, with the line passing through the origin, is not possible, suggesting a breakdown of the constant Φ<sub>i</sub> assumption. The values of the transport coefficients

ρΦ/δ backed out from each experimental point confirm that the Φ<sub>i</sub> increases strongly with loading at the upstream face of the membrane; see Figure 2c. Analysis of the CH<sub>4</sub> permeation experiments of Li et al.<sup>3</sup> at 333 and 373 K leads to a similar conclusion; this information is included in Appendix D of the Supporting Information.

The CH<sub>4</sub> permeation characteristics in DDR are analogous to that in CHA; the results are presented in Figure 3 parts a, b, and c. The sharp increase in the transport coefficients ρΦ/δ, backed out from the Tomita et al.<sup>2</sup> data with q<sub>i,up</sub>, is particularly noteworthy; see Figure 3c. We resort to MD simulations in order to get further insights into the nature of the loading dependence of Φ<sub>i</sub> of CH<sub>4</sub> in different zeolite structures. Figure 4 summarizes the MD simulation results of Φ<sub>i</sub> for CH<sub>4</sub> as a function of the loading q<sub>i</sub> in 14 different zeolite structures divided into 3 broad classes: (a) intersecting channels (MFI, ISV, and BEA), (b) one-dimensional channels (AFI, MOR, MTW, TON, FER, and LTL), and (c) cages separated by windows (LTA, FAU, CHA, DDR, and ERI), following the classification suggested by Beerdse et al.<sup>12</sup> Figure 4 extends our earlier published MD database<sup>7,9,10,13</sup> to include ISV, BEA, CHA, DDR, ERI, and LTL. For every zeolite structure, Φ<sub>i</sub> is seen to be a strong function of the loading q<sub>i</sub>. Without exception, the Φ<sub>i</sub> reduces to zero at saturation loading q<sub>i,sat</sub>; this can be verified by examination of the detailed MD simulation results, along with GCMC simulations of the sorption isotherms up to saturation limits that are available in Appendix B of the Supporting Information accompanying this publication. As the saturation loading is approached, the MS diffusivity Φ<sub>i</sub> and the self-diffusivity D<sub>i,sel</sub> approach each other. Since all the vacant “sites” within the zeolite framework are nearly all occupied, most of the molecular jumps will be unsuccessful and the molecule will invariably return to its original site, resulting in vanishingly small diffusivities. Some qualitative clues to the differences in the nature of the Φ<sub>i</sub>–q<sub>i</sub> dependence in various zeolites can be obtained from the free energy profiles of CH<sub>4</sub> along the direction of molecular transport.<sup>12</sup>

For intersecting channel structures (MFI, ISV, and BEA), the variation of Φ<sub>i</sub> is less than ~10% provided q<sub>i</sub> < 2 mol/kg; see Figure 4a. The loading dependence is also related to the size of the molecules. For N<sub>2</sub>, which is comparable in size to CH<sub>4</sub>, the loading dependence in MFI shows a similar dependence as that for CH<sub>4</sub>. On the other hand for He, which is smaller than CH<sub>4</sub>, the Φ<sub>i</sub> in MFI is practically independent of loading; see Figure 4a.

Both sets of diffusivity data for CH<sub>4</sub> in MFI, membrane permeation experiments and MD simulations, show that the assumption of a constant Φ<sub>i</sub> for values of q<sub>i</sub> < 2 mol/kg is perhaps not unreasonable; this is evidenced in the comparison of the two sets in Figure 1c.

For 1D channel structures, the Φ<sub>i</sub>–q<sub>i</sub> dependence can be related to the loading dependence of the inverse of thermodynamic correction factor Γ<sub>i</sub>:

$$\frac{1}{\Gamma_i} \equiv \frac{d \ln q_i}{d \ln f_i} \quad (4)$$

As has been discussed in an earlier publication,<sup>13</sup> for 1D channel structures, as an approximation, the Φ<sub>i</sub>–q<sub>i</sub> dependence is proportional to 1/Γ<sub>i</sub> – q<sub>i</sub>; verification for this can be found in the detailed information provided in Appendix B of the Supporting Information.

In FAU, which has cages separated by wide windows, the Φ<sub>i</sub> decreases practically linearly with (1 – θ<sub>i</sub>), where

**Table 1.** Three-Site Langmuir Parameters for CH<sub>4</sub> and CO<sub>2</sub> in MFI, CHA, and DDR<sup>a</sup>

zeolite	molecule, temperature	three-site Langmuir parameters				
		<i>b</i> <sub>i,A</sub>	<i>q</i> <sub>i,sat,A</sub>	<i>b</i> <sub>i,B</sub>	<i>q</i> <sub>i,sat,B</sub>	<i>b</i> <sub>i,C</sub>
MFI	CH <sub>4</sub> , 300 K	3.25 × 10 <sup>-6</sup>	2.8	2.2 × 10 <sup>-8</sup>	0.7	1.12 × 10 <sup>-10</sup>
CHA	CH <sub>4</sub> , 300 K	1.72 × 10 <sup>-6</sup>	2.77	2.7 × 10 <sup>-8</sup>	4.16	9.0 × 10 <sup>-10</sup>
DDR	CH <sub>4</sub> , 300 K	3.5 × 10 <sup>-6</sup>	1.66	1.45 × 10 <sup>-8</sup>	1.66	2.7 × 10 <sup>-11</sup>
MFI	CO <sub>2</sub> , 300 K	5.78 × 10 <sup>-6</sup>	3.4	2.76 × 10 <sup>-8</sup>	1.0	1.46 × 10 <sup>-9</sup>
CHA	CO <sub>2</sub> , 300 K	5.21 × 10 <sup>-6</sup>	6.93	1.02 × 10 <sup>-7</sup>	1.73	1.17 × 10 <sup>-9</sup>
DDR	CO <sub>2</sub> , 300 K	7.5 × 10 <sup>-6</sup>	1.66	2.0 × 10 <sup>-6</sup>	1.66	1.2 × 10 <sup>-8</sup>

<sup>a</sup> The saturation capacity *q*<sub>sat</sub> has the units of mol kg<sup>-1</sup>. The Langmuir parameters *b*<sub>i</sub> have the units of Pa<sup>-1</sup>.

is the fractional occupancy of species *i*.<sup>6,7</sup> For cage structures separated by narrow windows (LTA, ERI, CHA, and DDR), there is a sharp initial increase in  $\Phi_i$ , followed by an inevitable decline to zero value as saturation loading is approached. From Figure 4c, we note for CHA there is a 5-fold increase in  $\Phi_i$  at  $q_i \approx 4$  mol/kg. The increase in the MS diffusivity is due to the reduction in the energy barrier for intercage hopping of molecules with increased occupancy within each cage.<sup>12</sup> The MD simulated  $\Phi_i$  for CHA are also plotted in Figure 2c for direct comparison with the corresponding values of the transport coefficients  $\rho\Phi_i/\delta$  backed out from the permeation experiments in SAPO-34 membrane. The loading dependences of the two sets of parameters are similar.

From Figure 4c, we note that for DDR there is a 70-fold increase in  $\Phi_i$  at  $q_i \approx 3$  mol/kg. The MD simulated  $\Phi_i$  are plotted in Figure 3c for direct comparison with the corresponding values of the transport coefficients  $\rho\Phi_i/\delta$  backed out from the permeation experiments in DDR membrane. The loading dependences of the two sets of parameters appear to be similar, but unfortunately, the experiments were carried out with low upstream loadings,  $q_i < 1$  mol/kg, and so the 70-fold increase in  $\Phi_i$ , anticipated by the MD simulations, cannot be verified by the permeation experiments.

To quantify the loading dependence, we use the model developed by Reed and Ehrlich<sup>19,22</sup> for surface diffusion of adsorbed molecules. In the Reed–Ehrlich model, as applied earlier by Krishna and van Baten<sup>7</sup> for zeolite structures, the intermolecular interactions *within* a cage are assumed to influence the hopping frequencies of molecules *between* cages, by a factor  $\phi_i = \exp(\delta E_i/RT)$ , where  $\delta E_i$  represents the reduction in the energy barrier for diffusion. The values of  $\delta E_i$  can be calculated from the free energy profiles obtained from molecular simulations.<sup>12</sup> The Reed–Ehrlich model leads to the following expression for the MS diffusivity as a function of the fractional occupancy,  $\theta_i$ ,

$$\Phi_i = \Phi_i(0) \frac{(1 + \epsilon_i)^{z-1}}{(1 + \epsilon_i/\phi_i)^z} \quad (6)$$

where *z* is the coordination number, representing the maximum number of nearest neighbors within a cage. The choice of the value of *z* can be made on the basis of information on the maximum number of molecules that can be accommodated in each cage, i.e., from information on the saturation capacity. The other parameters are defined as (see ref 22 for more detailed discussions and derivations)

$$\epsilon_i = \frac{(\beta_i - 1 + 2\theta_i)\phi_i}{2(1 - \theta_i)}, \quad \beta_i = \sqrt{1 - 4\theta_i(1 - \theta_i)(1 - 1/\phi_i)} \quad (7)$$

The MD simulated  $\Phi_i$  values for LTA, ERI, CHA, and DDR

are used to fit  $\phi_i$ ; the fitted values are reported in Table 2, and the continuous solid lines in Figure 4b represent these fits.

With the Reed–Ehrlich loading dependence, we may define a modified driving force MDF<sub>i</sub> (see Appendix C of Supporting Information),

$$\text{MDF}_i \equiv \int_{f_{i,\text{down}}}^{f_{i,\text{up}}} \frac{(1 + \epsilon_i)^{z-1} q_i}{(1 + \epsilon_i/\phi_i)^z f_i} df_i = \int_{f_{i,\text{down}}}^{f_{i,\text{up}}} \frac{(1 + \epsilon_i)^{z-1}}{(1 + \epsilon_i/\phi_i)^z} \left( \frac{q_{i,\text{sat},A} b_{i,A}}{1 + b_{i,A} f_i} + \frac{q_{i,\text{sat},B} b_{i,B}}{1 + b_{i,B} f_i} + \frac{q_{i,\text{sat},C} b_{i,C}}{1 + b_{i,C} f_i} \right) df_i \quad (8)$$

The integration must be carried out numerically. The modified driving force must be expected to bear a linear relation with the permeation flux

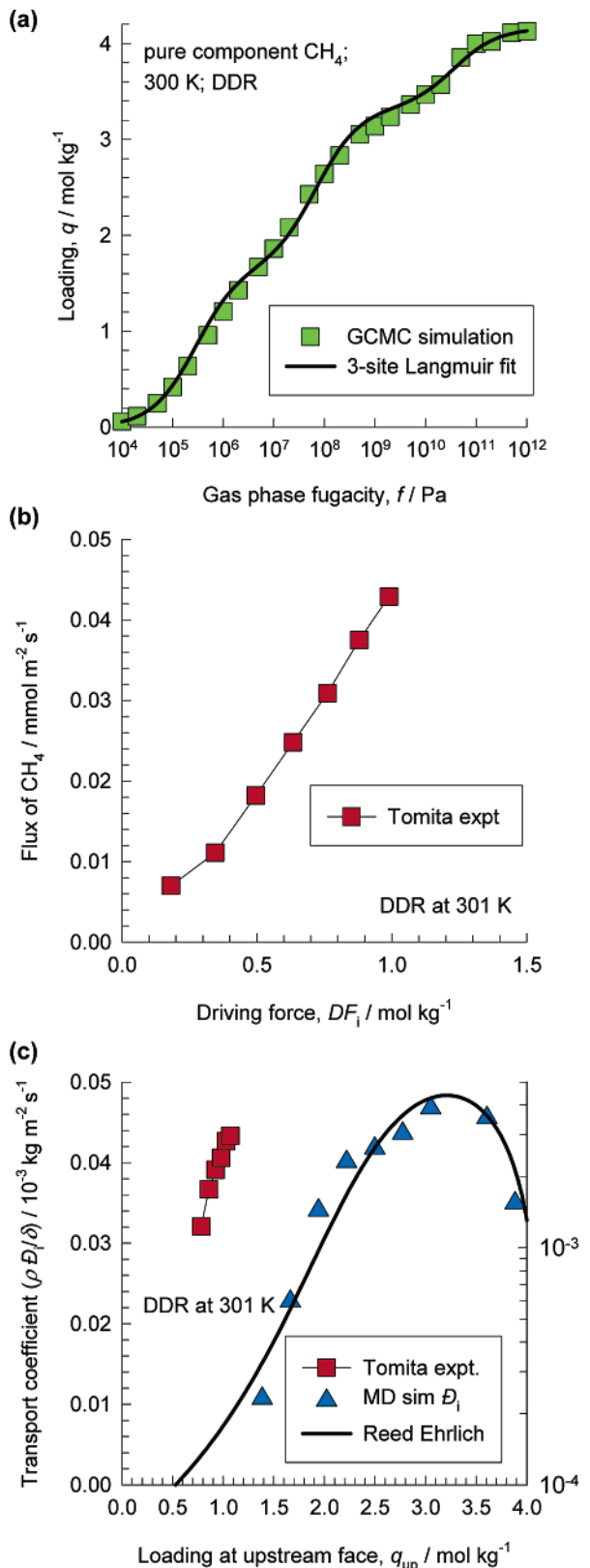
$$N_i = \frac{\rho \Phi_i(0)}{\delta} \text{MDF}_i \quad (9)$$

This expectation is fulfilled for both CHA and DDR; see Figure 5 parts a and b. The results in Figure 5 provide justification for use of the Reed–Ehrlich parameters derived from MD simulations of  $\Phi_i$  for modeling CH<sub>4</sub> membrane permeation. It must be stressed that the Reed–Ehrlich parameters *f* and *z* cannot be backed out from membrane permeation experiments, except perhaps by trial and error.

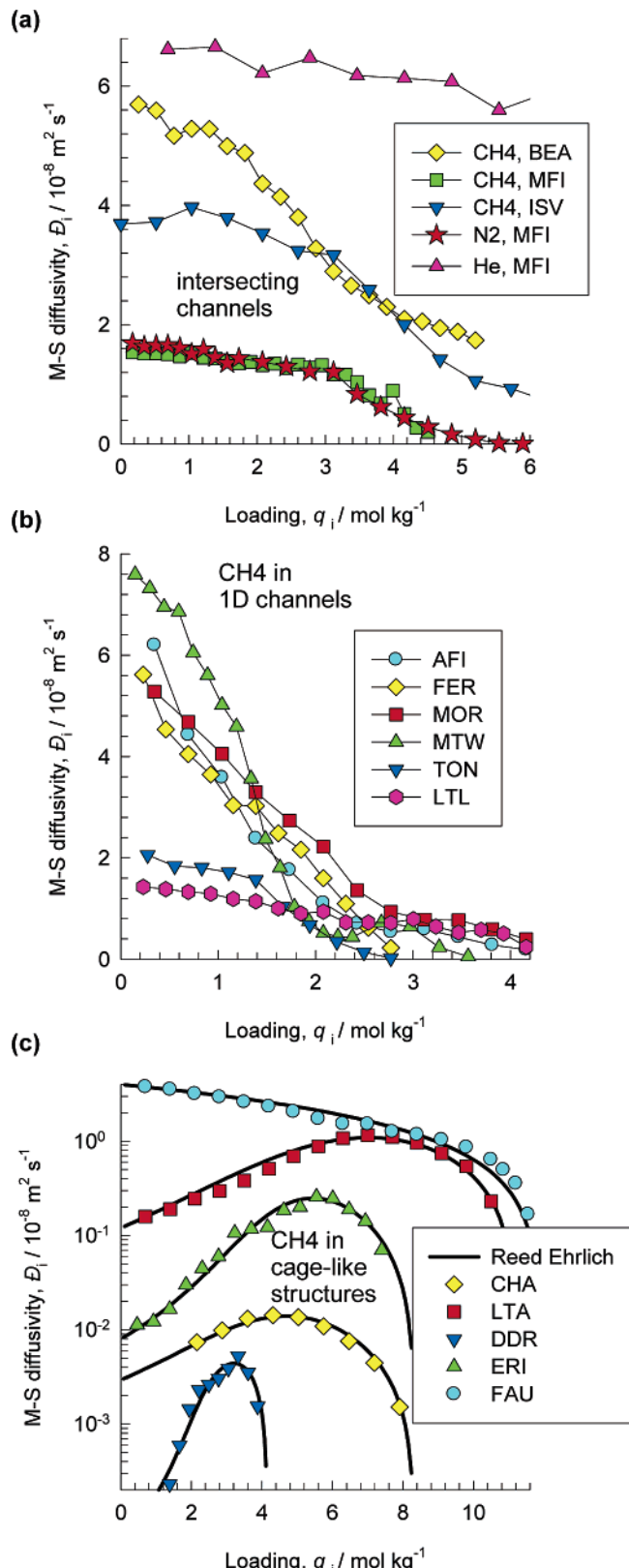
### 3. Analysis of CO<sub>2</sub> Permeation across Zeolite Membranes

Figure 6 shows the MD simulations for the loading dependence of the MS diffusivity of CO<sub>2</sub> in (a) MFI, (b) CHA, and (c) DDR. The variation of  $\Phi_i$  with *q*<sub>*i*</sub> is quite different for CO<sub>2</sub> than for CH<sub>4</sub> in the corresponding structures. For example in MFI,  $\Phi_i$  decreases almost linearly with *q*<sub>*i*</sub>, in agreement with the published MD simulation results of Papadopoulos et al.<sup>15</sup> Apparently the molecular length influences the loading dependence in the intersecting channel structure of MFI. CO<sub>2</sub> is a longer molecule than CH<sub>4</sub>, and its loading dependence is analogous to that of C<sub>2</sub>H<sub>6</sub>, which has a comparable length. As shown in Figure 6a for both CO<sub>2</sub> and C<sub>2</sub>H<sub>6</sub>, the  $\Phi_i$  decreases nearly linearly with *q*<sub>*i*</sub>, reducing to vanishingly small values at saturation loading. The Reed–Ehrlich model can also be applied to the describe the loading dependence of CO<sub>2</sub> in MFI, using our earlier work as a guideline.<sup>23</sup> The continuous solid lines in Figure 6a are drawn with the Reed–Ehrlich model with parameters listed in Table 2.

CO<sub>2</sub> is a more slender molecule than CH<sub>4</sub>, and therefore, the energy barrier for hopping between cages, separated by narrow windows, can be expected to be much lower than that for CH<sub>4</sub>. Consequently, the  $\Phi_i$  of CO<sub>2</sub> in CHA and DDR does not show the sharp initial increase as observed for CH<sub>4</sub>; see Figure 6 parts b and c. To stress this point further, we have plotted the MS diffusivities for He in CHA and DDR; see Figure 6 parts a and



**Figure 3.** (a) Sorption isotherm data for  $\text{CH}_4$  in DDR at 300 K. Also shown by the continuous line is the three-site Langmuir fit of the GCMC simulated isotherm. (b) The experimental data<sup>2</sup> on permeation flux of  $\text{CH}_4$  is plotted against the driving force  $DF_i$ , calculated from eq 3. (c) Transport coefficients,  $\rho D/\delta$  backed out using eq 2, are shown as a function of the loadings at the upstream face of the membrane,  $q_{up}$ . Also plotted in (c) are the MD simulated  $D_i$  (right y-axis). The continuous solid line in (c) is drawn with the Reed-Ehrlich parameters listed in Table 2.



**Figure 4.** MD simulation results on the loading dependences of the MS diffusivity  $D_i$  of  $\text{CH}_4$  in zeolites of three different topologies: (a) intersecting channels (MFI, ISV, and BEA), (b) one-dimensional channels (AFI, MOR, MTW, TON, FER, and LTL), and (c) cages separated by windows (LTA, FAU, CHA, DDR, and ERI). The simulation results are for 300 K with the exception of LTA (750 K), ERI (600 K), and DDR (373 K). Appendix B of the Supporting Information accompanying this publication also provides data on GCMC simulated adsorption isotherms. Also shown by continuous solid lines in (c) are the Reed-Ehrlich model calculations using the parameter values as listed in Table 2.

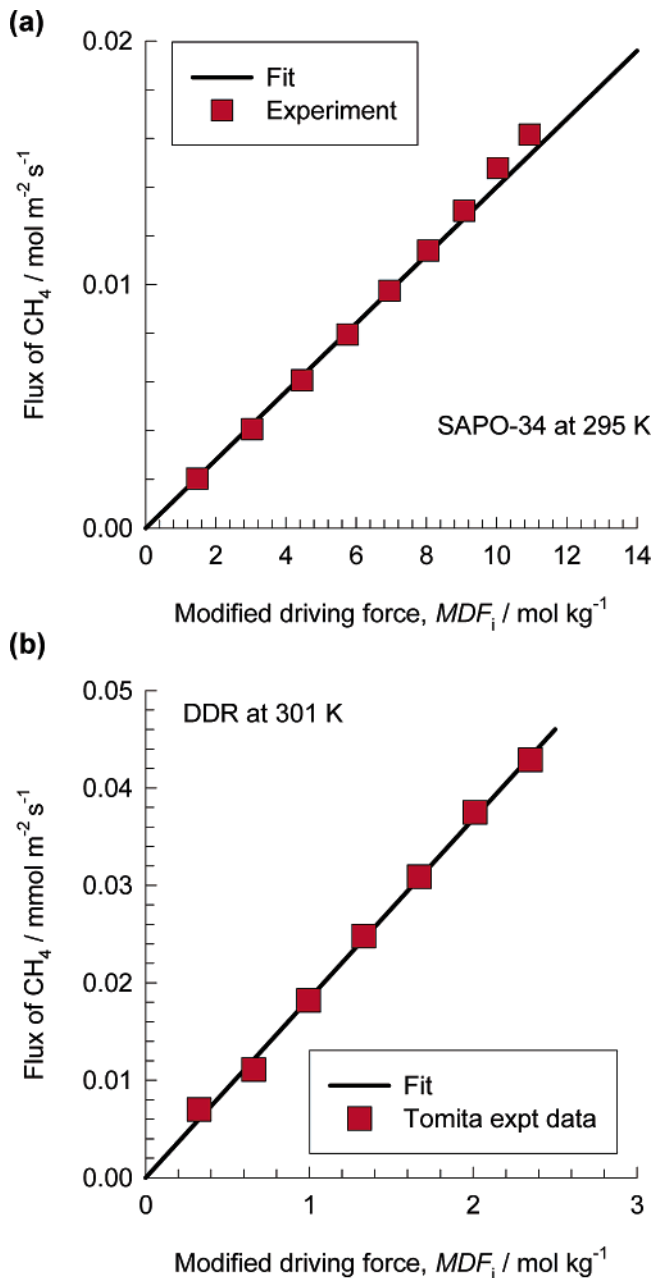


**Figure 5.** (a) Experimental data<sup>3</sup> on permeation flux of  $\text{CH}_4$  in CHA at 295 K is plotted against the modified driving force  $MDF_i$ , calculated from eq 8. (b) The experimental data<sup>2</sup> on permeation flux of  $\text{CH}_4$  in DDR at 300 K is plotted against the driving force  $MDF_i$ , calculated from eq 8. The continuous solid lines are drawn with fitted values as indicated in Table 3.

$$\theta_i \equiv q_i/q_{i,\text{sat}} \quad i = 1, 2, \dots, n \quad (5)$$

b. The  $\mathfrak{D}_i$  for He is practically loading independent, pointing to the fact that the energy barrier for intercage hopping is not influenced by the loading.  $\text{N}_2$  is a molecule that is intermediate in size, both with respect to slenderness and cross section, between  $\text{CO}_2$  and  $\text{CH}_4$ . The loading dependence of the  $\mathfrak{D}_i$  of  $\text{N}_2$  in CHA shows a slight increase with loading; cf. Figure 6b. This increase in  $\mathfrak{D}_i$  of  $\text{N}_2$  with  $q_i$  is smaller than that for  $\text{CH}_4$ , which has a slightly larger cross section than  $\text{N}_2$ .

It remains now to examine whether the permeation data for  $\text{CO}_2$  bears out the MD simulation results for the loading dependence shown in Figure 6. Consider the pure  $\text{CO}_2$  permeation experiments at 303 K in MFI zeolite as reported by Zhu et al.<sup>4</sup> Figure 7a compares the GCMC simulated isotherm with the experimental isotherm data of Zhu et al.<sup>4</sup> Up to the

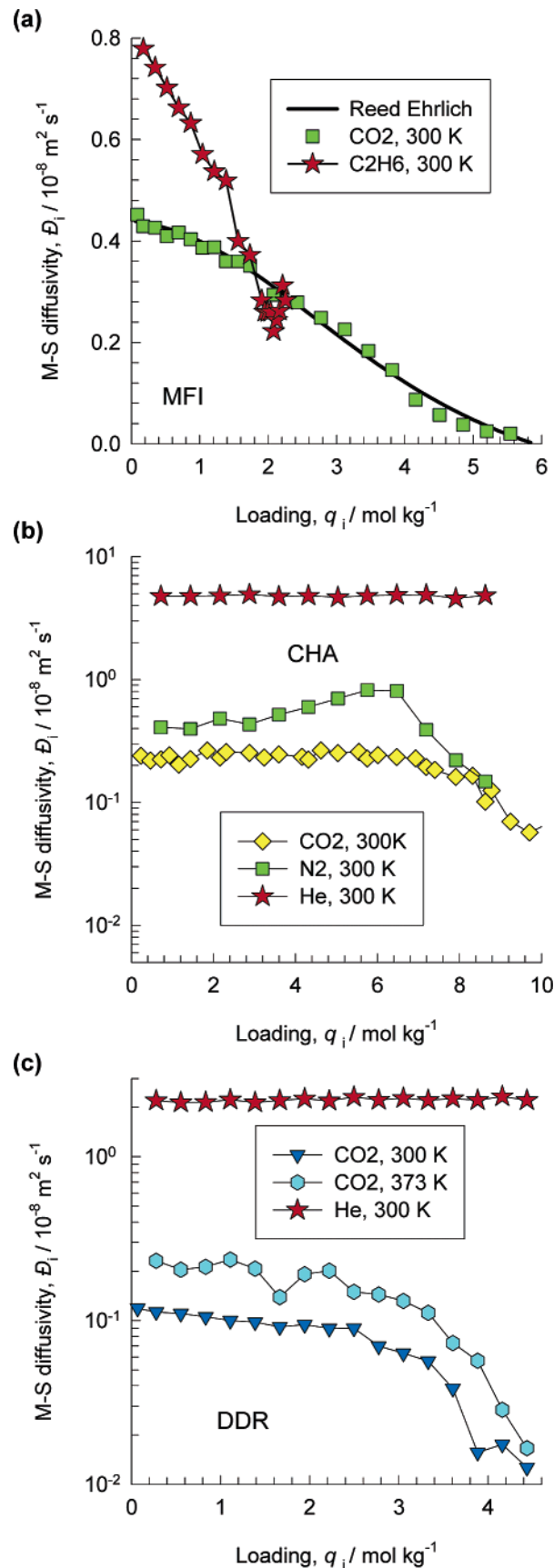


**Figure 6.** MD simulation results on the loading dependences of the MS diffusivity  $\mathfrak{D}_i$  of  $\text{CO}_2$  in MFI, CHA, and DDR zeolites. Also shown by continuous solid line in (a) is the Reed-Ehrlich model calculations using the parameter values as listed in Table 2.

**Table 2.** Reed-Ehrlich Parameters in Various Zeolite Structures

zeolite	molecule	temperature	saturation capacity, $q_{i,\text{sat}}$ , mol/kg	$\bar{\mathbf{D}}_i(0)$ , $10^{-8} \text{ m}^2 \text{ s}^{-1}$	$z$	Reed-Ehrlich model parameters in eqs 6 and 7
FAU	CH <sub>4</sub>	300 K	11.9	4	1	
LTA	CH <sub>4</sub>	750 K	11.19	0.12	9	$2.4 \exp(-0.45\theta_i)$
ERI	CH <sub>4</sub>	600 K	8.32	0.008	6	$6.5 \exp(-1.0\theta_i)$
CHA	CH <sub>4</sub>	300 K	8.32	0.0029	6	$3.2 \exp(-0.7\theta_i)$
DDR	CH <sub>4</sub>	300 K	4.16	0.000 062 3	5	$6 \exp(-0.2\theta_i)$
MFI	CO <sub>2</sub>	300 K	5.9	0.44	2.5	$1.44 \exp(-0.72\theta_i)$

range of pressures used in the experimental isotherms, 1 MPa, there is good agreement between the two sets of results. The GCMC data could be fitted with a three-site Langmuir model with the parameters as specified in Table 1, using a total saturation capacity  $q_{i,\text{sat}} = q_{i,\text{sat},A} + q_{i,\text{sat},B} + q_{i,\text{sat},C} = 5.9 \text{ mol kg}^{-1}$ , which is higher than the value of 2.97 used in the single-site Langmuir fit of Zhu et al.<sup>4</sup> but in reasonable agreement with the value of 5 mol kg<sup>-1</sup> chosen by Golden and Sircar.<sup>20</sup> Figure 7b presents a plot of the experimental permeation flux  $N_i$  against  $\bar{\mathbf{D}}_i$ . The plot appears to be almost linear. However, a closer examination shows that the flux varies less than proportionately with  $\bar{\mathbf{D}}_i$ ; this is observed more clearly in Figure 7c, where the values of the transport coefficients  $\rho\bar{\mathbf{D}}_i/\delta$  backed out from each experimental point are plotted against the upstream loading  $q_{i,\text{up}}$ . There appears to be a systematic decrease in the value of the transport coefficient with increasing  $q_{i,\text{up}}$ ; this trend is consistent with that for the loading dependence MS diffusivity  $\bar{\mathbf{D}}_i$  of CO<sub>2</sub>, the values of which are also plotted in Figure 7c with the right y-axis. The loading dependencies of the two sets of coefficients are nearly identical, at least within the range in which the experiments were performed. Insertion of the Reed-Ehrlich parameters determined from the MD simulation results, listed in Table 2, into eq 8 allows determination of the modified driving force MDF<sub>i</sub>. The plot of  $N_i$  vs MDF<sub>i</sub> is a straight line; see Figure 8. This confirms that  $\bar{\mathbf{D}}_i$  decreases with  $q_i$  in the same manner as anticipated by the MD simulations.

An important practical consequence of the decrease of the  $\bar{\mathbf{D}}_i$  with  $q_i$  for CO<sub>2</sub> is that the permeation selectivity,  $\alpha_{\text{perm}}$ , defined as the ratio of the fluxes of CO<sub>2</sub> to that of CH<sub>4</sub>,

$$\alpha_{\text{perm}} = N_1/N_2 \quad (10)$$

decreases more sharply with increasing upstream fugacities than that dictated by the sorption selectivity,

$$\alpha_{\text{sorp}} = q_{1,\text{up}}/q_{2,\text{up}} \quad (11)$$

This trend is indeed confirmed by the pure-component permeation experiments of Zhu et al.;<sup>4</sup> see Figure 9a. The dashed line represents the calculations of the pure-component permeation selectivity using eq 9 to calculate the fluxes of the individual components with the fitted values of  $\rho\bar{\mathbf{D}}_i(0)/\delta$  obtained of 0.0093 and  $0.0191 \text{ kg m}^{-2} \text{ s}^{-1}$ , obtained from the fits shown in Figures 1b and 8, for CH<sub>4</sub> and CO<sub>2</sub>, respectively (see Table 3).

We turn to analysis of CO<sub>2</sub> permeation in CHA. The GCMC simulation results for the sorption isotherm are compared in Figure 10a with the experimental isotherm reported by Li et al.<sup>21</sup> The experimental isotherm data is only available up to a pressure of 120 kPa, and there is good agreement with the GCMC simulations for this range. The GCMC simulated isotherms were fitted with the three-site Langmuir model with parameters specified in Table 1. The saturation capacity  $q_{i,\text{sat}} = q_{i,\text{sat},A} + q_{i,\text{sat},B} + q_{i,\text{sat},C} = 10.4 \text{ mol/kg}$  is significantly higher than the value obtained in the single-site Langmuir fit value of

5.0 mol/kg used by Li et al.<sup>21</sup> In Figure 10b, the permeation fluxes reported by Li et al.<sup>3</sup> are plotted against the DF<sub>i</sub> calculated using eq 3. The variation of  $N_i$  with DF<sub>i</sub> is practically linear, and a value of the transport coefficient  $\rho\bar{\mathbf{D}}_i/\delta = 0.0154$  provides a good representation of the permeation flux data, at least within the range  $0 < q_{i,\text{up}} < 7 \text{ mol/kg}$ . In Figure 10c, transport coefficients  $\rho\bar{\mathbf{D}}_i/\delta$ , backed out using eq 2, are shown as a function of the loadings at the upstream face of the membrane,  $q_{i,\text{up}}$ . Also plotted in Figure 10c are the MD simulated  $\bar{\mathbf{D}}_i$  (right y-axis). The two sets of coefficients appear to suggest that the assumption of loading independent  $\bar{\mathbf{D}}_i$  is not unreasonable.

Within the loading range  $0 < q_{i,\text{up}} < 7 \text{ mol/kg}$ , the  $\bar{\mathbf{D}}_i$  for CH<sub>4</sub> in CHA increases with  $q_i$ . Consequently, the permeation selectivity,  $\alpha_{\text{perm}}$ , should be expected to decrease more sharply with increasing upstream fugacities than dictated by the sorption selectivity  $\alpha_{\text{sorp}}$ . The pure-component permeation experiments of Li et al.<sup>3</sup> confirm this expectation; see Figure 9b. The dashed line in Figure 9b represents the calculations of the pure-component permeation selectivity using eq 9 to calculate the fluxes of the individual components with fitted values of  $\rho\bar{\mathbf{D}}_i(0)/\delta = 0.0154$  and  $1.4 \times 10^{-3} \text{ kg m}^{-2} \text{ s}^{-1}$ , respectively, for CO<sub>2</sub> and CH<sub>4</sub>.

We turn to CO<sub>2</sub> permeation in DDR. The GCMC simulated isotherm at 300 K is shown in Figure 11a. The variation of  $N_i$  with DF<sub>i</sub> is nearly linear, suggesting that the assumption of a constant  $\bar{\mathbf{D}}_i$  is justified for the loading range used in the experiments; see Figure 11b. A value of the transport coefficient  $\rho\bar{\mathbf{D}}_i/\delta = 0.0103$  appears to provide a fair representation of the permeation flux data. In Figure 11c, the values of transport coefficients  $\rho\bar{\mathbf{D}}_i/\delta$ , backed out using eq 2, are shown as a function of the loadings at the upstream face of the membrane,  $q_{i,\text{up}}$ . Also plotted in Figure 11c are the MD simulated  $\bar{\mathbf{D}}_i$  (right y-axis). We note that the permeation data suggest a slight increase in  $\rho\bar{\mathbf{D}}_i/\delta$  with loading, whereas the MD simulated  $\bar{\mathbf{D}}_i$  suggest a slight decrease. There is a need for permeation data for CO<sub>2</sub> in DDR membranes to much higher upstream pressures in order to ascertain the correct loading dependence. Here, we proceed further with the assumption of a loading-independent diffusivity for CO<sub>2</sub> in DDR. Within the loading range  $0 < q_{i,\text{up}} < 1 \text{ mol/kg}$ , the  $\bar{\mathbf{D}}_i$  for CH<sub>4</sub> increases with  $q_i$ . Consequently, the permeation selectivity,  $\alpha_{\text{perm}}$ , should be expected to decrease more sharply with increasing upstream fugacities than dictated by the sorption selectivity  $\alpha_{\text{sorp}}$ . The pure-component permeation experiments of Tomita et al.<sup>2</sup> are in conformity with this expectation; see Figure 9c. The dashed line in Figure 9c represents the calculations of the pure-component permeation selectivity using eq 9 to calculate the fluxes of the individual components with fitted values of  $\rho\bar{\mathbf{D}}_i(0)/\delta = 0.0103$  and  $1.84 \times 10^{-5} \text{ kg m}^{-2} \text{ s}^{-1}$ , respectively, for CO<sub>2</sub> and CH<sub>4</sub>.

Analysis of the CH<sub>4</sub> and CO<sub>2</sub> permeation experiments of Li et al.<sup>3</sup> and Tomita et al.<sup>2</sup> in CHA and DDR membranes at temperatures of 333, 373, 423, and 473 K leads to a similar conclusions; this information is included in Appendix D of the Supporting Information.

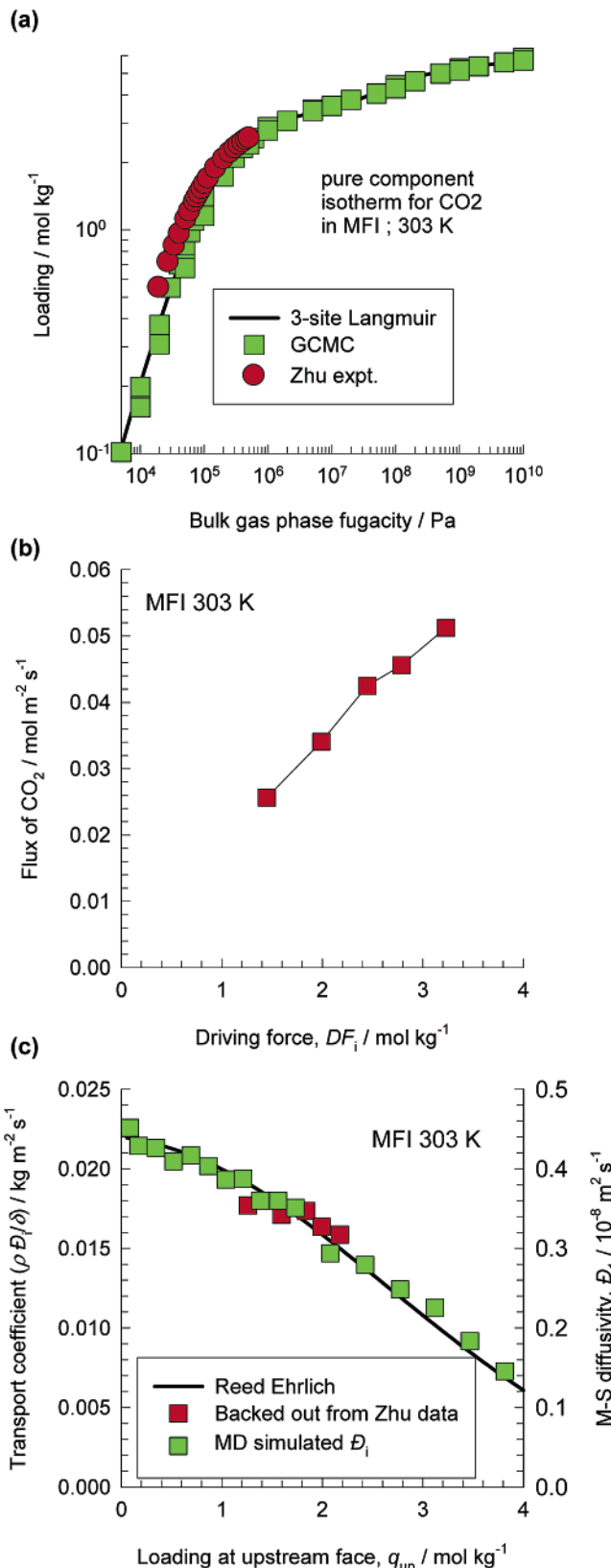


**Figure 7.** Sorption isotherm data for CO<sub>2</sub> in MFI at 303 K. The GCMC simulation results are compared with the experimental data of Zhu et al.<sup>4</sup> Also shown by the continuous line is the three-site Langmuir fit of the GCMC simulated isotherm. (b) The experimental data<sup>4</sup> on permeation flux of CO<sub>2</sub> is plotted against the driving force DF<sub>i</sub>, calculated from eq 3. (c) Transport coefficients, backed out using eq 2, are shown as a function of the loadings at the upstream face of the membrane,  $q_{\text{up}}$ . Also plotted in (c) are the MD simulated  $D_i$  (right y-axis). The continuous solid line in (c) is drawn with the Reed and Ehrlich parameters listed in Table 2.

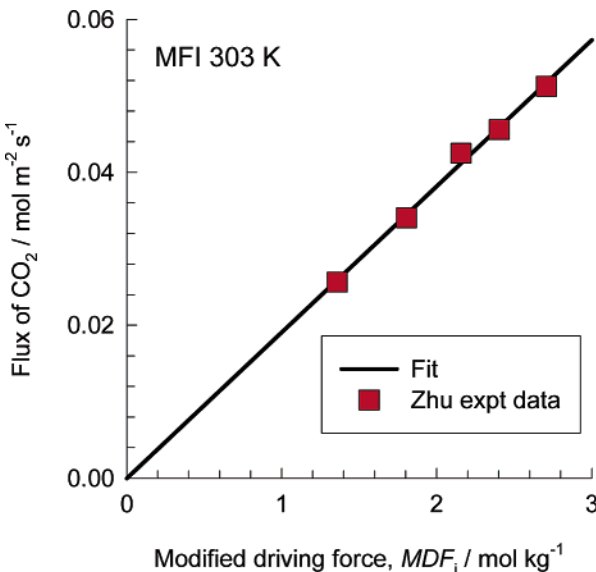


**Figure 8.** CO<sub>2</sub> permeation flux in MFI at 303 K is plotted against the modified driving force MDF<sub>i</sub>, calculated from eq 8. The straight line is obtained with  $\rho D_i(0)/\delta$  indicated in Table 3.

#### 4. Implication for Mixture Permeation across Zeolite Membranes

For mixture diffusion in zeolite, the MS equation in the form

$$-\frac{\theta_i}{RT} \nabla \mu_i = \sum_{\substack{j=1 \\ j \neq i}}^n \frac{q_j N_i - q_i N_j}{q_{i,\text{sat}} q_{j,\text{sat}} \bar{D}_{ij}} + \frac{N_i}{q_{i,\text{sat}} \bar{D}_i} \quad i = 1, \dots, n \quad (12)$$

was developed by Kapteijn et al.<sup>17</sup> to account for the influence of unequal saturation capacities on mixture diffusion. For proper modeling of mixture permeation, the loading dependence of each of the MS diffusivities  $\bar{D}_i$  in the mixture needs to be accounted for.

Consider permeation of a mixture of CO<sub>2</sub> and CH<sub>4</sub> across an MFI membrane, with equal partial fugacities in the upstream compartment. The sorption selectivity for a 50–50 mixture is shown in Figure 12a as a function of the upstream partial fugacity of each component; these calculations were performed with the ideal adsorbed solution theory (IAST) of Myers and Prausnitz,<sup>24</sup> using the pure-component isotherm data listed in Table 1. We note that  $\alpha_{\text{sorp}}$  increases with increasing  $f_{i,\text{up}}$ ; this increase is due to entropy effects.<sup>25</sup> From Figure 12a, we note that the experimentally determined  $\alpha_{\text{perm}}$ , however, decreases with increasing  $f_{i,\text{up}}$ . The reasons for the decrease in  $\alpha_{\text{perm}}$  are 2-fold: (1) the decrease in  $\bar{D}_i$  of CO<sub>2</sub> with  $q_i$  and (2) the slowing down of the “fast” CO<sub>2</sub> molecules by the more “tardy” CH<sub>4</sub> molecules. The slowing-down effect is captured by the binary exchange coefficient  $\bar{D}_{ij}$  in eq 12; this term is a reflection of correlation effects in zeolite diffusion.<sup>26</sup>

For permeation of a 50–50 mixture of CO<sub>2</sub> and CH<sub>4</sub> across the CHA membrane, the permeation and sorption selectivities are compared in Figure 12b. The experimental  $\alpha_{\text{perm}}$  increases less sharply with the upstream partial fugacity. The explanation for this observation is to be found in the increase in the  $\bar{D}_i$  of CH<sub>4</sub> with  $q_i$ .

For quantitative modeling of mixture permeation, it is necessary to have a good estimation of the binary exchange parameter  $\bar{D}_{ij}$ . Both Zhu<sup>4</sup> and Li<sup>3</sup> follow the suggestions in our earlier work<sup>18</sup> and estimate this exchange parameter from the

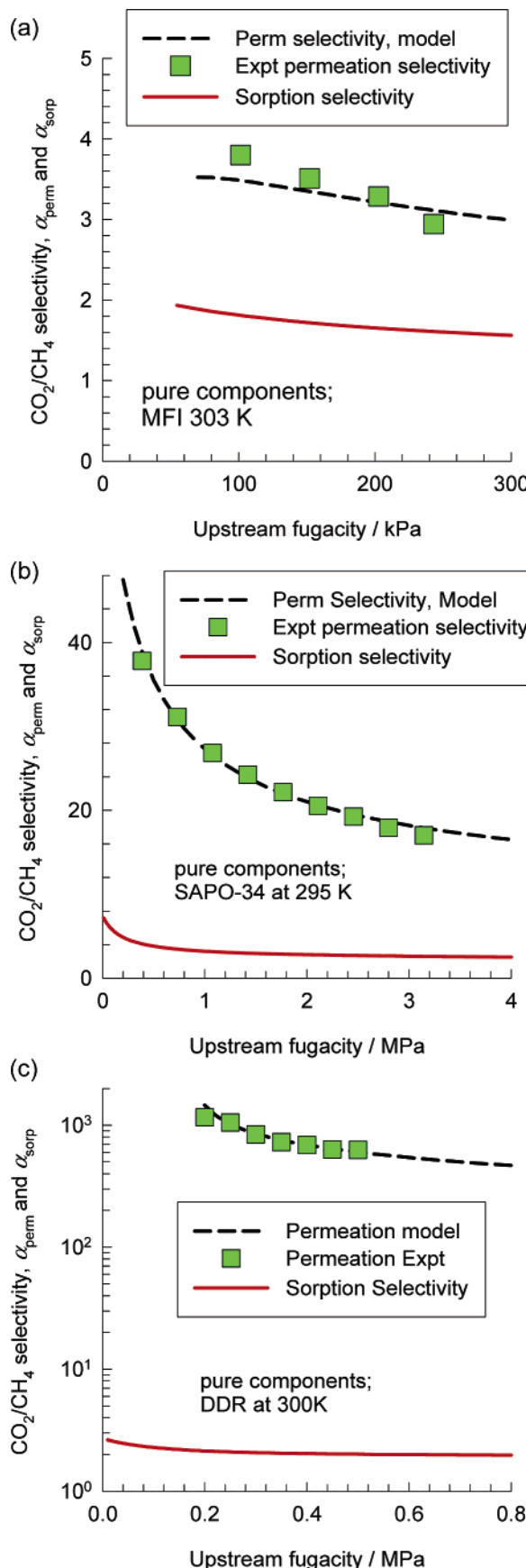


**Figure 9.** Experimental permeation selectivity,  $\alpha_{\text{permeation}}$ , along with calculated sorption selectivity,  $\alpha_{\text{sorption}}$ , as a function of the upstream feed fugacity for pure-component permeation of  $\text{CO}_2$  and  $\text{CH}_4$  across (a) MFI, (b) CHA, and (c) DDR membranes.

**Table 3. Fitted Values of Transport Coefficients  $\rho \mathfrak{D}_i(0)/\delta$  with Units of  $\text{kg m}^{-2} \text{s}^{-1}$**

zeolite	molecule	temperature	$\rho \mathfrak{D}_i(0)/\delta$
MFI	$\text{CH}_4$	303 K	$9.3 \times 10^{-3}$
CHA	$\text{CH}_4$	295 K	$1.4 \times 10^{-3}$
DDR	$\text{CH}_4$	300 K	$1.84 \times 10^{-5}$
MFI	$\text{CO}_2$	303 K	$1.91 \times 10^{-2}$
CHA	$\text{CO}_2$	295 K	$1.54 \times 10^{-2}$
DDR	$\text{CO}_2$	300 K	$1.03 \times 10^{-2}$

MS diffusivities of the pure components,  $\mathfrak{D}_i$ , using the interpolation formula.

$$\mathfrak{D}_{ij} = [\mathfrak{D}_i]^{q_i/(q_i+q_j)} [\mathfrak{D}_j]^{q_j/(q_i+q_j)} \quad (13)$$

More recent work using MD simulations<sup>7,10,26,27</sup> has shown that unequal saturation capacities violates the symmetry assumption of the  $\mathfrak{D}_{ij}$ ; conformity with the Onsager reciprocal relations demands that

$$q_{j,\text{sat}} \mathfrak{D}_{ij} = q_{i,\text{sat}} \mathfrak{D}_{ji} \quad (14)$$

Furthermore, the following, more general, interpolation formula has shown to be valid for mixture diffusion in zeolites and carbon nanotubes,<sup>7,10,26,27</sup>

$$q_{j,\text{sat}} \mathfrak{D}_{ij} = [q_{j,\text{sat}} \mathfrak{D}_{ii}]^{q_i/(q_i+q_j)} [q_{i,\text{sat}} \mathfrak{D}_{jj}]^{q_j/(q_i+q_j)} = q_{i,\text{sat}} \mathfrak{D}_{ji} \quad (15)$$

where  $\mathfrak{D}_{ii}$  is the self-exchange coefficient that can be calculated from pure-component MS and self-diffusivities:

$$\mathfrak{D}_{ii} = \frac{\theta_i}{\frac{1}{1 - \frac{1}{D_{i,\text{self}}} - \frac{1}{\mathfrak{D}_i}}} \quad (16)$$

The interpolation formula (eq 13) is recovered from the more general eq 15 when the saturation capacities are equal, and taking  $\mathfrak{D}_{ii}/\mathfrak{D}_i = 1$ . For diffusion of  $\text{CH}_4$  in various zeolite topologies, the value of the parameter  $\mathfrak{D}_{ii}/\mathfrak{D}_i$  obtained from MD simulations are plotted in Figure 13 against the loading  $q_i$ . For both intersecting channel structures and for one-dimensional channels,  $\mathfrak{D}_{ii}/\mathfrak{D}_i$  is significantly smaller than unity, suggesting that correlation effects are stronger than anticipated in the interpolation formula (eq 13).

For LTA, CHA, ERI, and DDR that contain cages separated by narrow windows,  $\mathfrak{D}_{ii}/\mathfrak{D}_i$  is larger than unity. This suggests that the intercage jumps are practically uncorrelated because only one molecule at a time can pass through the narrow windows. A good approximation in such cases is  $\mathfrak{D}_{ii}/\mathfrak{D}_i \rightarrow \infty$ ; this leads to the following simplification of eq 12,

$$\mathbf{N}_i = -\rho \mathfrak{D}_i \frac{q_i}{RT} \nabla \mu_i; \quad i = 1, \dots, n \quad (17)$$

relations which were used by Habgood<sup>28</sup> to describe mixture diffusion in LTA-4A. Our reanalysis of the Habgood experimental data<sup>18</sup> has indeed yielded a good match with a model employed using eq 17.

## 5. Conclusions

The following conclusions can be drawn from the results presented in this paper.

(1) The MS diffusivity  $\mathfrak{D}_i$  of  $\text{CH}_4$  in zeolite structures is generally a strong function of loading and decreases to zero at saturation loading,  $q_{i,\text{sat}}$ . In zeolite structures consisting of cages

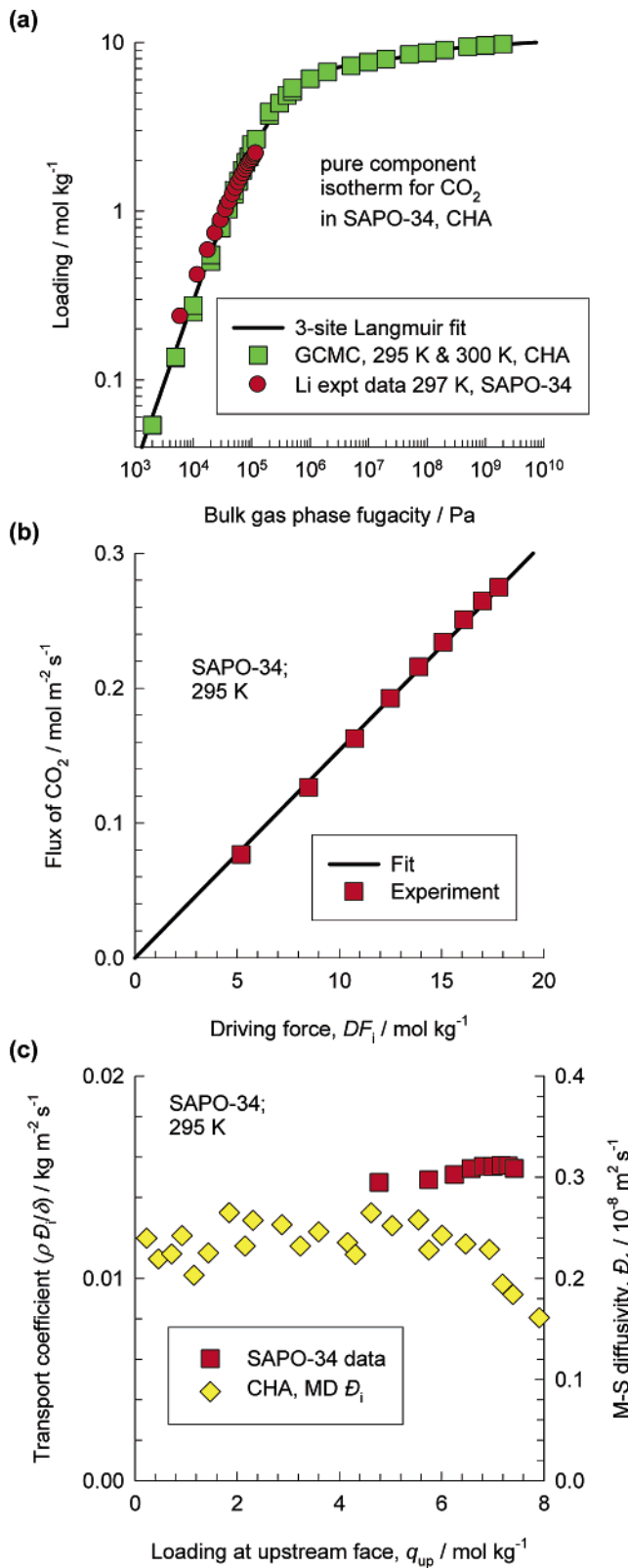


**Figure 10.** (a) Sorption isotherm data for CO<sub>2</sub> in CHA (SAPO-34) at 297 K. The GCMC simulation results are compared with the experimental data of Li et al.<sup>21</sup> Also shown by the continuous line is the three-site Langmuir fit of the GCMC simulated isotherm. (b) The experimental data<sup>3</sup> on permeation flux of CO<sub>2</sub> is plotted against the driving force DF<sub>i</sub>, calculated from eq 3. The straight line in (b) is obtained with  $\rho\Theta/\delta$  indicated in Table 3. (c) Transport coefficients  $\rho\Theta/\delta$ , backed out using eq 2, are shown as a function of the loadings at the upstream face of the membrane,  $q_{i,up}$ . Also plotted in (c) are the MD simulated  $D_i$  (right y-axis).

separated by narrow windows (CHA, DDR, ERI, and LTA),  $\Theta_i$  increases sharply with loading before decreasing to zero at

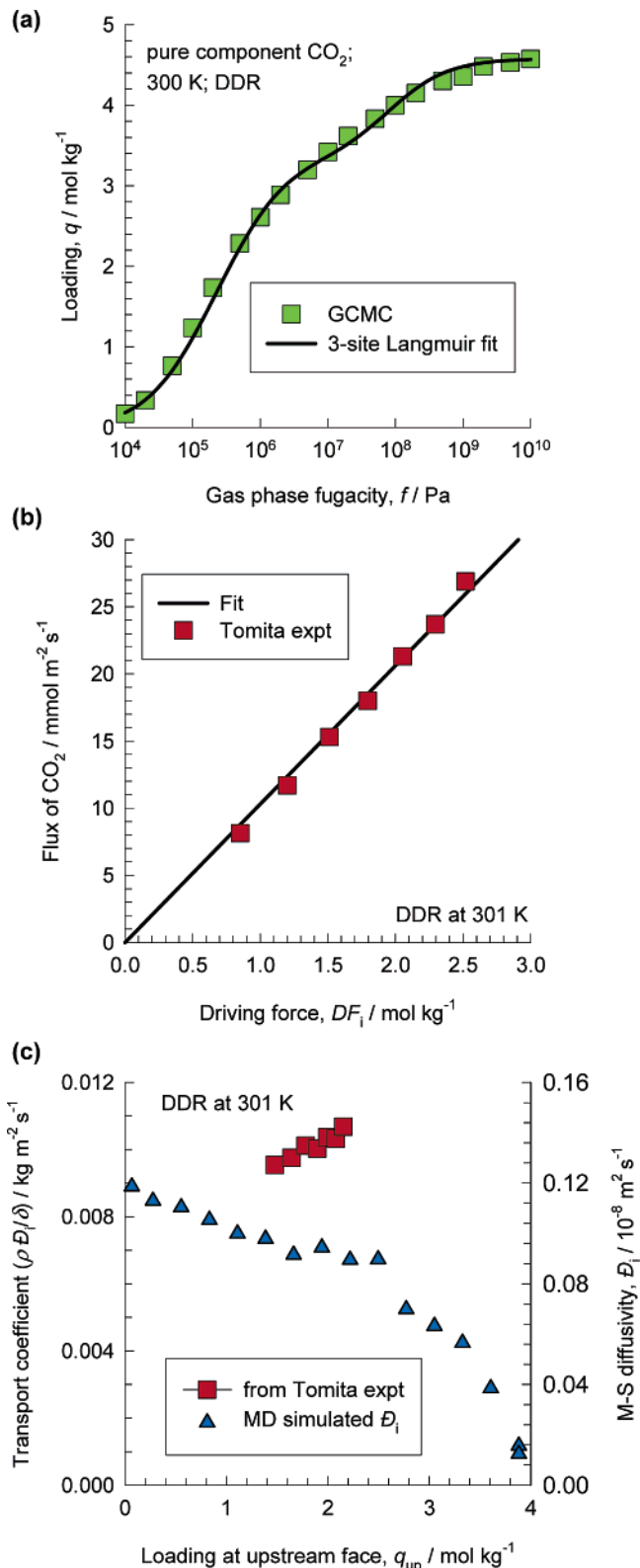


**Figure 11.** (a) Sorption isotherm data for CO<sub>2</sub> in DDR at 300 K. Also shown by the continuous line is the three-site Langmuir fit of the GCMC simulated isotherm. (b) The experimental data<sup>2</sup> on permeation flux of CO<sub>2</sub> is plotted against the driving force DF<sub>i</sub>, calculated from eq 3. The straight line in (b) is obtained with  $\rho\Theta/\delta$  indicated in Table 3. (c) Transport coefficients  $\rho\Theta/\delta$ , backed out using eq 2, are shown as a function of the loadings at the upstream face of the membrane,  $q_{i,up}$ . Also plotted in (c) are the MD simulated  $D_i$  (right y-axis).

$q_{i,sat}$ . This increase in the diffusivity is due to the reduction in the free energy barrier for intercage hopping of molecules. The

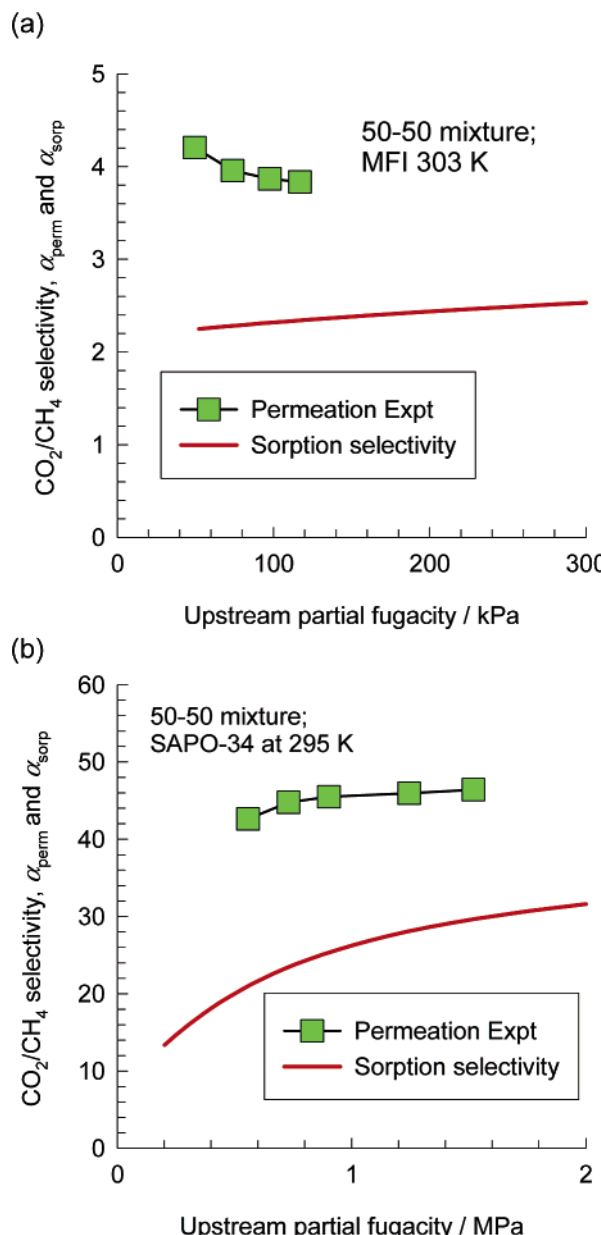


**Figure 12.** Experimental permeation selectivity,  $\alpha_{\text{perm}}$ , along with calculated sorption selectivity,  $\alpha_{\text{sorp}}$ , as a function of the upstream feed fugacity for 50–50 mixture permeation of  $\text{CO}_2$  and  $\text{CH}_4$  across (a) MFI and (b) CHA membranes. The sorption selectivities have been calculated using the IAST<sup>24</sup> with pure-component isotherm parameters listed in Table 1.

Reed–Ehrlich model<sup>19</sup> is a particularly simple and useful model to describe the  $\mathfrak{D}_i-q_i$  dependence.

(2) The  $\mathfrak{D}_i-q_i$  dependence of  $\text{CO}_2$  in zeolites is different from that for  $\text{CH}_4$ . For diffusion of  $\text{CO}_2$  in MFI, the  $\mathfrak{D}_i$  in MFI decreases with  $q_i$ . In CHA and DDR, the  $\mathfrak{D}_i$  remains constant for occupancies below about 0.5 and, subsequently, reduces to zero values at saturation. The differences between the loading dependences are to be attributed to the factor that  $\text{CO}_2$  is a more slender, and longer, molecule than  $\text{CH}_4$ .

(3) A unary permeation model incorporating the Reed–Ehrlich description of the  $\mathfrak{D}_i-q_i$  dependence provides a good description of the experimental data for  $\text{CH}_4$  and  $\text{CO}_2$  permeation across MFI, CHA, and DDR membranes.

(4) MD simulation results for the self-exchange coefficient  $\mathfrak{D}_{ii}$  are used to show that the commonly used interpolation formula (eq 13) must be replaced by the more general eq 15 for estimation of the binary exchange parameter  $\mathfrak{D}_{12}$ . For zeolites

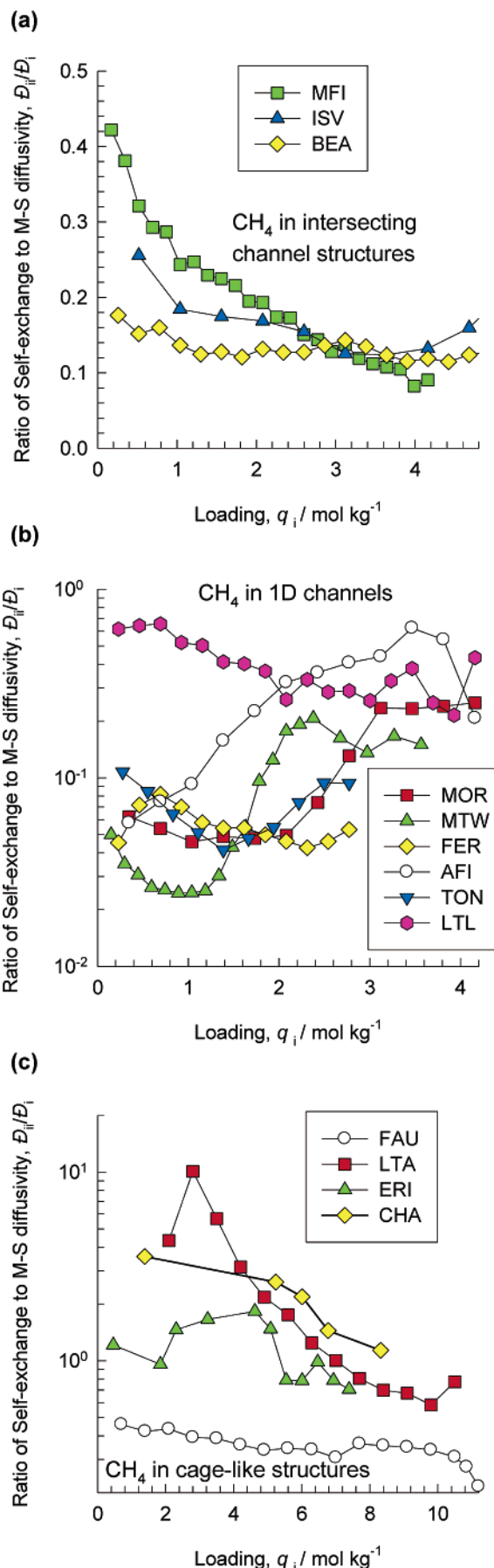


**Figure 13.** MD simulation results on the loading dependences of the ratio of the self-exchange coefficient to the MS diffusivity  $\mathfrak{D}_{ii}/\mathfrak{D}_i$  for  $\text{CH}_4$  in zeolites of varying topologies: (a) intersecting channel structures, (b) one-dimensional channels, and (c) cages connected by windows.

with cages separated by narrow windows, the assumption of  $\Theta_{ii}/\Theta_i \rightarrow \infty$  is perhaps a good approximation. The quantitative verification of this approximation is the subject of a subsequent publication.

## Acknowledgment

R.K. and J.M.v.B. acknowledge the grant of a TOP subsidy from The Netherlands Foundation for Fundamental Research (NWO-CW) for intensification of reactors and NWO/NCF for provision of high performance computing resources. E.G.-P. and S.C. would like to thank the European Commission (for a Marie Curie Reintegration Grant) and the Spanish Ministry of Science and Technology for financial support.

**Supporting Information Available:** Appendix A presents some details of the GCMC and MD simulation methodologies, including the force fields used. Appendix B contains complete data on the GCMC and MD simulation results for adsorption and diffusion of  $\text{CH}_4$  and  $\text{CO}_2$  in various zeolite topologies; this also includes snapshots of the location of the molecules in various frameworks. Appendix C gives detailed derivation of the unary permeation model, including the loading dependence of the MS diffusivity. Appendix D contains additional analysis of permeation of  $\text{CH}_4$  and  $\text{CO}_2$  in CHA and DDR at 333, 373, 423, and 473 K. This material is available free of charge via the Internet at <http://pubs.acs.org>.

## Notation

$b_i$  = Langmuir constant,  $\text{Pa}^{-1}$

$D_{i,\text{self}}$  = self-diffusivity,  $\text{m}^2 \text{s}^{-1}$

$\Theta_i$  = Maxwell–Stefan diffusivity of species  $i$ ,  $\text{m}^2 \text{s}^{-1}$

$\Theta_i(0)$  = zero-loading MS diffusivity of species  $i$ ,  $\text{m}^2 \text{s}^{-1}$

$\Theta_{ii}$  = self-exchange diffusivity,  $\text{m}^2 \text{s}^{-1}$

$\Delta F_i$  = driving force for transport across membrane,  $\text{mol kg}^{-1}$

$f_i$  = fugacity of species  $i$ ,  $\text{Pa}$

$MDF_i$  = modified driving force for transport across membrane,  $\text{mol kg}^{-1}$

$N_i$  = molar flux of species  $i$  across membrane,  $\text{mol m}^{-2} \text{s}^{-1}$

$q_i$  = molar loading,  $\text{mol kg}^{-1}$

$q_{i,\text{sat}}$  = saturation loading,  $\text{mol kg}^{-1}$

$R$  = gas constant,  $8.314 \text{ J mol}^{-1} \text{ K}^{-1}$

$T$  = absolute temperature,  $\text{K}$

$z$  = coordination number, dimensionless

## Greek Letters

$\alpha_{\text{perm}}$  = permeation selectivity, dimensionless

$\alpha_{\text{sorp}}$  = sorption selectivity, dimensionless

$\beta_i$  = Reed–Ehrlich parameter, dimensionless

$\phi_i$  = Reed–Ehrlich parameter, dimensionless

$\Gamma_i$  = thermodynamic factor for pure component  $i$ , dimensionless

$\delta$  = thickness of zeolite membrane,  $\text{m}$

$\delta E_i$  = reduction in energy barrier for diffusion,  $\text{J mol}^{-1}$

$\epsilon_i$  = Reed–Ehrlich parameter, dimensionless

$\theta_i$  = fractional occupancy of component  $i$ , dimensionless

$\mu_i$  = molar chemical potential,  $\text{J mol}^{-1}$

$\rho$  = density of zeolite,  $\text{kg m}^{-3}$

## Subscripts

A, B, C = referring to sites A, B, C in three-site Langmuir isotherm

down = referring to downstream conditions

sat = referring to saturation conditions

up = referring to upstream conditions

## Literature Cited

- (1) McLeary, E. E.; Jansen, J. C.; Kapteijn, F. Gas separation characteristics of DDR type zeolite membrane. *Microporous Mesoporous Mater.* **2006**, *90*, 198–220.
- (2) Tomita, T.; Nakayama, K.; Sakai, H. Gas separation characteristics of DDR type zeolite membrane. *Microporous Mesoporous Mater.* **2004**, *68*, 71–75.
- (3) Li, S.; Martinek, J. G.; Falconer, J. L.; Noble, R. D.; Gardner, T. Q. High-Pressure  $\text{CO}_2/\text{CH}_4$  separation using SAPO-34 membranes. *Ind. Eng. Chem. Res.* **2005**, *44*, 3220–3228.
- (4) Zhu, W.; Hrabanek, P.; Gora, L.; Kapteijn, F.; Moulijn, J. A. Role of Adsorption in the Permeation of  $\text{CH}_4$  and  $\text{CO}_2$  through a Silicalite-1 Membrane. *Ind. Eng. Chem. Res.* **2006**, *45*, 767–776.
- (5) Skouidas, A. I.; Sholl, D. S. Molecular Dynamics Simulations of Self, Corrected, and Transport Diffusivities of Light Gases in Four Silica Zeolites to Assess Influences of Pore Shape and Connectivity. *J. Phys. Chem. A* **2003**, *107*, 10132–10141.
- (6) Chempath, S.; Krishna, R.; Snurr, R. Q. Nonequilibrium MD simulations of diffusion of binary mixtures containing short  $n$ -alkanes in faujasite. *J. Phys. Chem. B* **2004**, *108*, 13481–13491.
- (7) Krishna, R.; van Baten, J. M. Diffusion of alkane mixtures in zeolites. Validating the Maxwell–Stefan formulation using MD simulations. *J. Phys. Chem. B* **2005**, *109*, 6386–6396.
- (8) Chong, S. S.; Jobic, H.; Plazanet, M.; Sholl, D. S. Concentration Dependence of Transport Diffusion of Ethane in Silicalite: A Comparison between Neutron Scattering Experiments and Atomically-Detailed Simulations. *Chem. Phys. Lett.* **2005**, *408*, 157–161.
- (9) Krishna, R.; van Baten, J. M. Influence of isotherm inflection on the diffusivities of C5–C8 linear alkanes in MFI zeolite. *Chem. Phys. Lett.* **2005**, *407*, 159–165.
- (10) van Baten, J. M.; Krishna, R. Entropy effects in adsorption and diffusion of alkane isomers in mordenite: An investigation using CBMC and MD simulations. *Microporous Mesoporous Mater.* **2005**, *84*, 179–191.
- (11) Beerdse, E.; Dubbeldam, D.; Smit, B. Molecular Understanding of Diffusion in Confinement. *Phys. Rev. Lett.* **2005**, *95*, 164505.
- (12) Beerdse, E.; Dubbeldam, D.; Smit, B. Understanding Diffusion in Nanoporous Materials. *Phys. Rev. Lett.* **2006**, *96*, 044501.
- (13) Krishna, R.; van Baten, J. M. Linking the loading dependence of the Maxwell–Stefan diffusivity of linear alkanes in zeolites with the thermodynamic correction factor. *Chem. Phys. Lett.* **2006**, *420*, 545–549.
- (14) Krishna, R.; van Baten, J. M. Influence of isotherm inflection on the loading dependence of the diffusivities of  $n$ -hexane and  $n$ -heptane in MFI zeolite. Quasi-Elastic Neutron Scattering experiments supplemented by molecular simulations. *J. Phys. Chem. B* **2006**, *110*, 2195–2201.
- (15) Papadopoulos, G. K.; Jobic, H.; Theodorou, D. N. Transport diffusivity of  $\text{N}_2$  and  $\text{CO}_2$  in silicalite: Coherent quasielastic neutron scattering measurements and molecular dynamics simulations. *J. Phys. Chem. B* **2004**, *108*, 12748–12756.
- (16) Krishna, R.; Wesselingh, J. A. The Maxwell–Stefan approach to mass transfer. *Chem. Eng. Sci.* **1997**, *52*, 861–911.
- (17) Kapteijn, F.; Moulijn, J. A.; Krishna, R. The generalized Maxwell–Stefan model for diffusion in zeolites: Sorbate molecules with different saturation loadings. *Chem. Eng. Sci.* **2000**, *55*, 2923–2930.
- (18) Krishna, R.; Baur, R. Modelling issues in zeolite based separation processes. *Sep. Purif. Technol.* **2003**, *33*, 213–254.
- (19) Reed, D. A.; Ehrlich, G. Surface diffusion, atomic jump rates and thermodynamics. *Surf. Sci.* **1981**, *102*, 588–609.
- (20) Golden, T. C.; Sircar, S. Gas-Adsorption on Silicalite. *J. Colloid Interface Sci.* **1994**, *162*, 182–188.
- (21) Li, S.; Falconer, J. L.; Noble, R. D. SAPO-34 membranes for  $\text{CO}_2/\text{CH}_4$  separation. *J. Membr. Sci.* **2004**, *241*, 121–135.
- (22) Krishna, R.; Paschek, D.; Baur, R. Modelling the occupancy dependence of diffusivities in zeolites. *Microporous Mesoporous Mater.* **2004**, *76*, 233–246.
- (23) Krishna, R.; van Baten, J. M. Kinetic Monte Carlo simulations of the loading dependence of diffusion in zeolites. *Chem. Eng. Technol.* **2005**, *28*, 160–167.
- (24) Myers, A. L.; Prausnitz, J. M. Thermodynamics of mixed gas adsorption. *AIChE J.* **1965**, *11*, 121–130.
- (25) Krishna, R.; Smit, B.; Calero, S. Entropy effects during sorption of alkanes in zeolites. *Chem. Soc. Rev.* **2002**, *31*, 185–194.

- (26) Skouidas, A. I.; Sholl, D. S.; Krishna, R. Correlation effects in diffusion of CH<sub>4</sub>/CF<sub>4</sub> mixtures in MFI zeolite. A study linking MD simulations with the Maxwell–Stefan formulation. *Langmuir* **2003**, *19*, 7977–7988.
- (27) Krishna, R.; van Baten, J. M. Describing binary mixture diffusion in carbon nanotubes with the Maxwell–Stefan equations. An investigation using molecular dynamics simulations. *Ind. Eng. Chem. Res.* **2006**, *45*, 2084–2093.
- (28) Habgood, H. W. The kinetics of molecular sieve action. Sorption of nitrogen–methane mixtures by Linde molecular sieve 4A. *Can. J. Chem.* **1958**, *36*, 1384–1397.

Received for review May 31, 2006  
Revised manuscript received July 25, 2006  
Accepted July 27, 2006

IE060693D

*Supporting information to accompany:*

# Incorporating the loading dependence of the Maxwell-Stefan diffusivity in the modeling of CH<sub>4</sub> and CO<sub>2</sub> permeation across zeolite membranes

**R. Krishna<sup>(1)\*</sup>, J.M. van Baten<sup>(1)</sup>, E. García-Pérez<sup>(2)</sup>, and S. Calero<sup>(2)</sup>**

<sup>(1)</sup>Van 't Hoff Institute for Molecular Sciences, University of Amsterdam, Nieuwe Achtergracht 166, 1018 WV Amsterdam, The Netherlands.

<sup>(2)</sup> Department of Environmental Sciences, University Pablo de Olavide, Ctra de Utrera, Km1, 41013 Seville, Spain

Contents:

Appendix A: Simulation methodologies

Appendix B: GCMC and MD simulation data for adsorption and diffusion of CH<sub>4</sub> and CO<sub>2</sub> in various zeolites

Appendix C: Unary permeation model

Appendix D: Additional CH<sub>4</sub> and CO<sub>2</sub> permeation data in SAPO-34 and DDR membranes.

# Appendix A: Simulation methodologies

## 1. GCMC simulation methodology

The adsorption isotherms for CH<sub>4</sub> and CO<sub>2</sub> in various zeolites were computed using Monte Carlo (MC) simulations in the grand canonical (GC) ensemble. The crystallographic data are available elsewhere.<sup>1</sup> The zeolite lattices are rigid during simulations, with static atomic charges that are assigned by choosing  $q_{\text{Si}} = +2.05$  and  $q_{\text{O}} = -1.025$ , following the work of Calero et al.<sup>2</sup> CH<sub>4</sub> molecules are described with a united atom model, in which each molecule is treated as a single interaction center.<sup>3</sup> CO<sub>2</sub> molecules are taken linear and rigid, with bond length C-O of 1.16 Å and partial charges distributed around each molecule to reproduce experimental quadrupole moment. The interaction between adsorbed molecules is described with Coulombic and Lennard-Jones terms. The parameters for methane are taken from Dubbeldam et al.<sup>4</sup> For CO<sub>2</sub> we use the 3LJ3CB.EPM2 potential.<sup>5</sup> The Lennard-Jones parameters for CH<sub>4</sub>-zeolite and CO<sub>2</sub>-zeolite interactions are taken from Dubbeldam et al.<sup>4</sup> and Makrodimitris et al.<sup>6</sup>, respectively.

The Lennard-Jones potentials are shifted and cut at 12 Å. The number of unit cells in the simulation box was chosen such that the minimum length in each of the coordinate directions was larger than 24 Å. Periodic boundary conditions were employed. Further GCMC simulation details are available in earlier publications.<sup>2,4</sup>

GCMC simulations of isotherms were carried out with all-silica zeolites in all but two cases; the FAU and LTA used had 96 Si and 96 Al atoms. The detailed validation of the force fields used for CH<sub>4</sub> and for CO<sub>2</sub> are available elsewhere.<sup>4,7</sup> We provide here only a brief comparison of experimental data with GCMC simulation results. Figure 1 compares the experimental data of Zhu et al.<sup>8</sup>, Sun et al.<sup>9</sup>, Choudhary and Mayadevi<sup>9</sup>, Hirotani et al.<sup>10</sup>, Yamazaki et al.<sup>11</sup>, Golden and Sircar<sup>12</sup> and Kishima et al.<sup>13</sup>

for adsorption of CO<sub>2</sub> and CH<sub>4</sub> in MFI (silicalite-1) at temperatures in the 298 K – 308 K range with GCMC simulations. We note that the agreement is very good for both species.

In Figure 2 and Figure 3 we compare the GCMC simulation results for all-silica CHA with isotherm data, measured at a variety of temperatures 253 K, 275 K, 297 K, 333 K, 373 K, 416 K and 473 K, of Li et al.<sup>14</sup> who used SAPO-34 with the composition Si<sub>x</sub>Al<sub>y</sub>P<sub>z</sub> with  $x/y = 0.15$ ;  $x+z = y$ . We consider this to be a reasonable *approximation* because the size of Si and P atoms are comparable and because the interactions of the adsorbed methane molecules with the zeolite structure is encapsulated in a Lennard-Jones interaction term with the much bulkier O atoms. The good agreement between the adsorption isotherms for both CH<sub>4</sub> and CO<sub>2</sub> between the experimental data *at all temperatures* with SAPO-34 and GCMC simulations with all-silica CHA support the use of the isotherm data for CHA for use in the analysis of membrane permeation results for SAPO-34.

## 2. MD simulation methodology

Diffusion is simulated using Newton's equations of motion until the system properties, on average, no longer change in time. The Verlet algorithm is used for time integration. The energy drift of the entire system is monitored to ensure that the time steps taken were not too large. A time step of 1 fs was used in all simulations. For each simulation, *initializing* CBMC moves are used to place the molecules in the domain, minimizing the energy. Next, follows an *equilibration* stage. Like the initialization stage this consists of CBMC moves, but now using velocity scaling; at each cycle all adsorbent pseudo-atom velocities are scaled to match the specified temperature. After a fixed number of initialization and equilibrium steps, the MD simulation *production* cycles start. For every cycle, the statistics for determining the mean square displacements (MSDs) are updated. The MSDs are determined for time intervals ranging from 2 fs to 1 ns. In order to do this, an order-*N* algorithm, as detailed in Chapter 4 of Frenkel and Smit<sup>15</sup> is implemented. The Nosé-Hoover thermostat is applied to all the diffusing particles.

The MD simulations were carried out for a variety of molecular loadings within the zeolites. All simulations were carried out on clusters of PCs equipped with Intel Xeon processors running at 3.4 GHz

on the Linux operating system. Each MD simulation, for a specified loading, was run for 120 h, determined to be long enough to obtain reliable statistics for determination of the diffusivities. In the case of CO<sub>2</sub> diffusion, several independent MD simulations were run and the results averaged.

The self-diffusivities,  $D_{i,\text{self}}$ , were computed by analyzing the mean square displacement of each component:

$$D_{i,\text{self}} = \frac{1}{2N_i} \lim_{\Delta t \rightarrow \infty} \frac{1}{\Delta t} \left\langle \left( \sum_{l=1}^{N_i} (\mathbf{r}_{l,i}(t + \Delta t) - \mathbf{r}_{l,i}(t))^2 \right) \right\rangle \quad (1)$$

In this expression  $N_i$  represents the number of molecules of species  $i$  respectively, and  $\mathbf{r}_{l,i}(t)$  is the position of molecule  $l$  of species  $i$  at any time  $t$ .

The Maxwell-Stefan diffusivity was determined for each of the coordinate directions

$$D = \frac{1}{2} \lim_{\Delta t \rightarrow \infty} \frac{1}{N} \frac{1}{\Delta t} \left\langle \left( \sum_{i=1}^N (\mathbf{r}_i(t + \Delta t) - \mathbf{r}_i(t))^2 \right)^2 \right\rangle \quad (2)$$

where  $\mathbf{r}_i(t)$  is the position of molecule  $i$  at any time  $t$  and  $N$  is the number of molecules. For 1D channel structures (AFI, MOR, TON, FER, LTL), the reported diffusivities are along the z-direction. For MTW the reported diffusivities are along the y-direction. For DDR the reported diffusivities are the averages in x- and y- directions  $D = (D_x + D_y)/2$ . For DDR there is no connectivity in the z-direction, as can be evidenced from the snapshots in Figure 4. For all other cases (MFI, ISV, BEA, FAU, LTA, ERI, CHA) the average values calculated according to  $D = (D_x + D_y + D_z)/3$  are presented. In all cases reported here, the MSD values were linear in  $t$  and we found no evidence of single file diffusion characteristics.

The self-exchange coefficient  $D_{ii}$  were calculated from

$$D_{ii} = \frac{\theta_i}{\frac{1}{D_{i,\text{self}}} - \frac{1}{D_i}} \quad (3)$$

where  $\theta_i$  is the fractional occupancy:

$$\theta_i = \frac{q_i}{q_{i,sat}} \quad (4)$$

The values of the saturation capacities  $q_{i,sat}$  were determined from GCMC simulations of the isotherms; this data are reported for each zeolite in the Appendix B of Supporting Information accompanying this publication.

Data for adsorption and diffusion of CH<sub>4</sub> were determined in fourteen different zeolites. The chosen zeolites fall into three categories consisting of (a) intersecting channels (MFI, ISV, BEA), (b) one-dimensional channel structures (AFI, MOR, TON, FER, LTL, MTW), and (c) cages separated by windows (FAU, LTA, CHA, ERI, DDR). Data for adsorption and diffusion of CO<sub>2</sub> were determined in MFI, CHA and DDR.

Some MD simulations were also carried out for He, Ar, N<sub>2</sub>, and C<sub>2</sub>H<sub>6</sub> in a variety of zeolites. For He and Ar the force fields used were taken from Skouidas et al.<sup>16, 17</sup>. The N<sub>2</sub> force field was taken from Makrodimitris et al.<sup>6</sup>. The force field for C<sub>2</sub>H<sub>6</sub> is from Dubbeldam et al.<sup>4</sup>

### 3. References

- (1) Baerlocher, C.; McCusker, L. B., Database of Zeolite Structures, <http://www.iza-structure.org/databases/>, International Zeolite Association, 10 January 2002.
- (2) Calero, S.; Dubbeldam, D.; Krishna, R.; Smit, B.; Vlugt, T. J. H.; Denayer, J. F. M.; Martens, J. A.; Maesen, T. L. M., Understanding the role of sodium during adsorption. A force field for alkanes in sodium exchanged faujasites, *J. Am. Chem. Soc.* **2004**, *126*, 11377-11386.
- (3) Ryckaert, J. P.; Bellemans, A., Molecular dynamics of liquid alkanes, *Faraday Discuss. Chem. Soc.* **1978**, *66*, 95-106.
- (4) Dubbeldam, D.; Calero, S.; Vlugt, T. J. H.; Krishna, R.; Maesen, T. L. M.; Smit, B., United Atom Forcefield for Alkanes in Nanoporous Materials, *J. Phys. Chem. B* **2004**, *108*, 12301-12313.
- (5) Harris, J. G.; Yung, K. H., Carbon Dioxide's Liquid-Vapor Coexistence Curve And Critical Properties as Predicted by a Simple Molecular Model, *J. Phys. Chem.* **1995**, *99*, 12021-12024.
- (6) Makrodimitris, K.; Papadopoulos, G. K.; Theodorou, D. N., Prediction of permeation properties of CO<sub>2</sub> and N<sub>2</sub> through silicalite via molecular simulations, *J. Phys. Chem. B* **2001**, *105*, 777-788.
- (7) García-Pérez, E.; Parra, J. B.; Ania, C. O.; Van Baten, J. M.; Krishna, R.; Calero, S., A computational study of CO<sub>2</sub>, N<sub>2</sub> and methane adsorption in zeolites, *Appl. Surf. Sci.* **2007**, *Manuscript in Preparation*,
- (8) Zhu, W.; Hrabanek, P.; Gora, L.; Kapteijn, F.; Moulijn, J. A., Role of Adsorption in the Permeation of CH<sub>4</sub> and CO<sub>2</sub> through a Silicalite-1Membrane, *Ind. Eng. Chem. Res.* **2006**, *45*, 767-776.

- (9) Sun, M. S.; Shah, D. B.; Xu, H. H.; Talu, O., Adsorption equilibria of C<sub>1</sub> to C<sub>4</sub> alkanes, CO<sub>2</sub>, and SF<sub>6</sub> on silicalite, *J. Phys. Chem. B* **1998**, *102*, 1466-1473.
- (10) Hirotani, A.; Mizukami, K.; Miura, R.; Takaba, H.; Miya, T.; Fahmi, A.; Stirling, A.; Kubo, M.; Miyamoto, A., Grand canonical Monte Carlo simulation of the adsorption of CO<sub>2</sub> on silicalite and NaZSM-5, *App. Surf. Sci.* **1997**, *120*, 81-84.
- (11) Yamazaki, T.; Katoh, M.; Ozawa, S.; Ogino, Y., Adsorption of CO<sub>2</sub> over univalent cation-exchanged ZSM-5 zeolites, *Mol. Phys.* **1993**, *80*, 313-324.
- (12) Golden, T. C.; Sircar, S., Gas-Adsorption on Silicalite, *J. Colloid Interface Sci.* **1994**, *162*, 182-188.
- (13) Kishima, M.; Mizuhata, H.; Okubo, T., Effects of Confinement on the Adsorption Behavior of Methane in High-Silica Zeolites, *J. Phys. Chem. B* **2006**, *110*, 13889-13896.
- (14) Li, S.; Falconer, J. L.; Noble, R. D., SAPO-34 membranes for CO<sub>2</sub>/CH<sub>4</sub> separation, *J. Membr. Sci.* **2004**, *241*, 121-135.
- (15) Frenkel, D.; Smit, B., Understanding molecular simulations: from algorithms to applications; 2nd Edition, Academic Press: San Diego, 2002.
- (16) Skouidas, A. I.; Sholl, D. S., Transport diffusivities of CH<sub>4</sub>, CF<sub>4</sub>, He, Ne, Ar, Xe, and SF<sub>6</sub> in silicalite from atomistic simulations, *J. Phys. Chem. B* **2002**, *106*, 5058-5067.
- (17) Skouidas, A. I.; Sholl, D. S., Molecular Dynamics Simulations of Self, Corrected, and Transport Diffusivities of Light Gases in Four Silica Zeolites to Assess Influences of Pore Shape and Connectivity, *J. Phys. Chem. A* **2003**, *107*, 10132-10141.

## 4. Captions for Figures

Figure 1. Comparison of GCMC simulations for pure component isotherms for CO<sub>2</sub> in (a) MFI and (b) CHA with experimental data of Zhu et al.<sup>8</sup>, Sun et al.<sup>9</sup>, Choudhary and Mayadevi<sup>9</sup>, Hirotani et al.<sup>10</sup>, Yamazaki et al.<sup>11</sup>, Golden and Sircar<sup>12</sup> and Kishima et al.<sup>13</sup>.

Figure 2. Experimental sorption isotherm data at 253 K, 275 K, 297 K for CH<sub>4</sub> and CO<sub>2</sub> in SAPO-34 of Li et al.<sup>14</sup> are compared with GCMC simulations in all-silica CHA at corresponding temperatures.

Figure 3. Experimental sorption isotherm data at 333 K, 373 K, 423 K, and 473 K for CH<sub>4</sub> and CO<sub>2</sub> in SAPO-34 of Li et al.<sup>14</sup> are compared with GCMC simulations in all-silica CHA at corresponding temperatures.

Figure 4. Snapshot of CO<sub>2</sub> molecules in DDR. There is no connectivity between the cages in z-direction and diffusion is possible only in x- and y- directions.

Figure 1

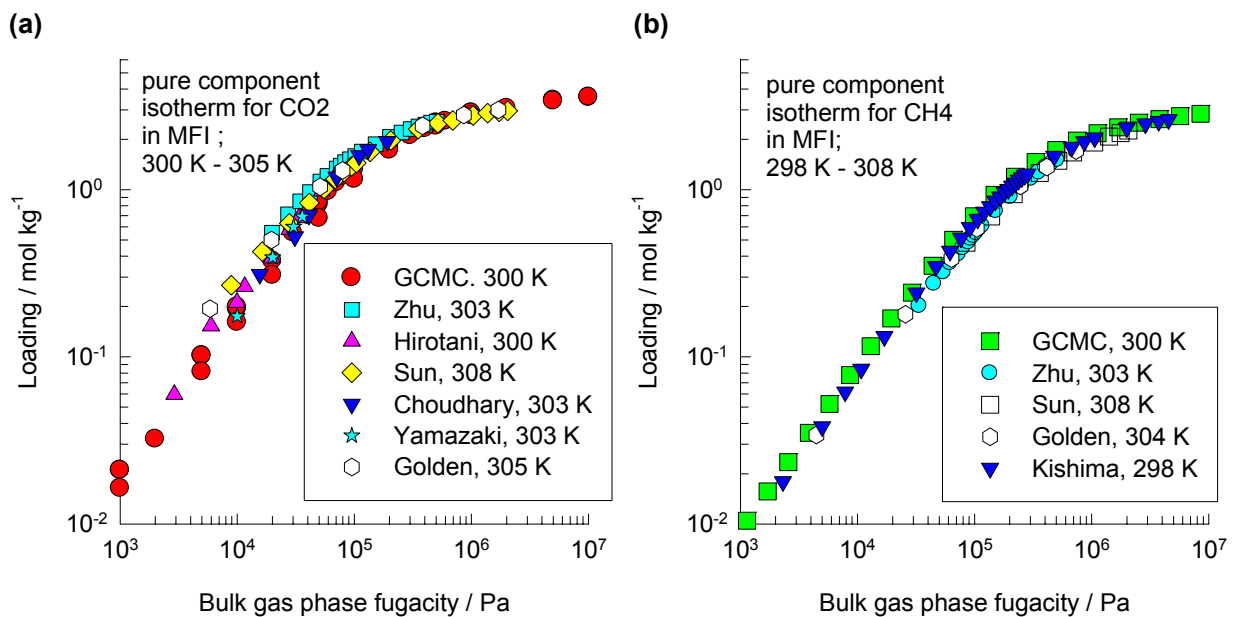


Figure 2

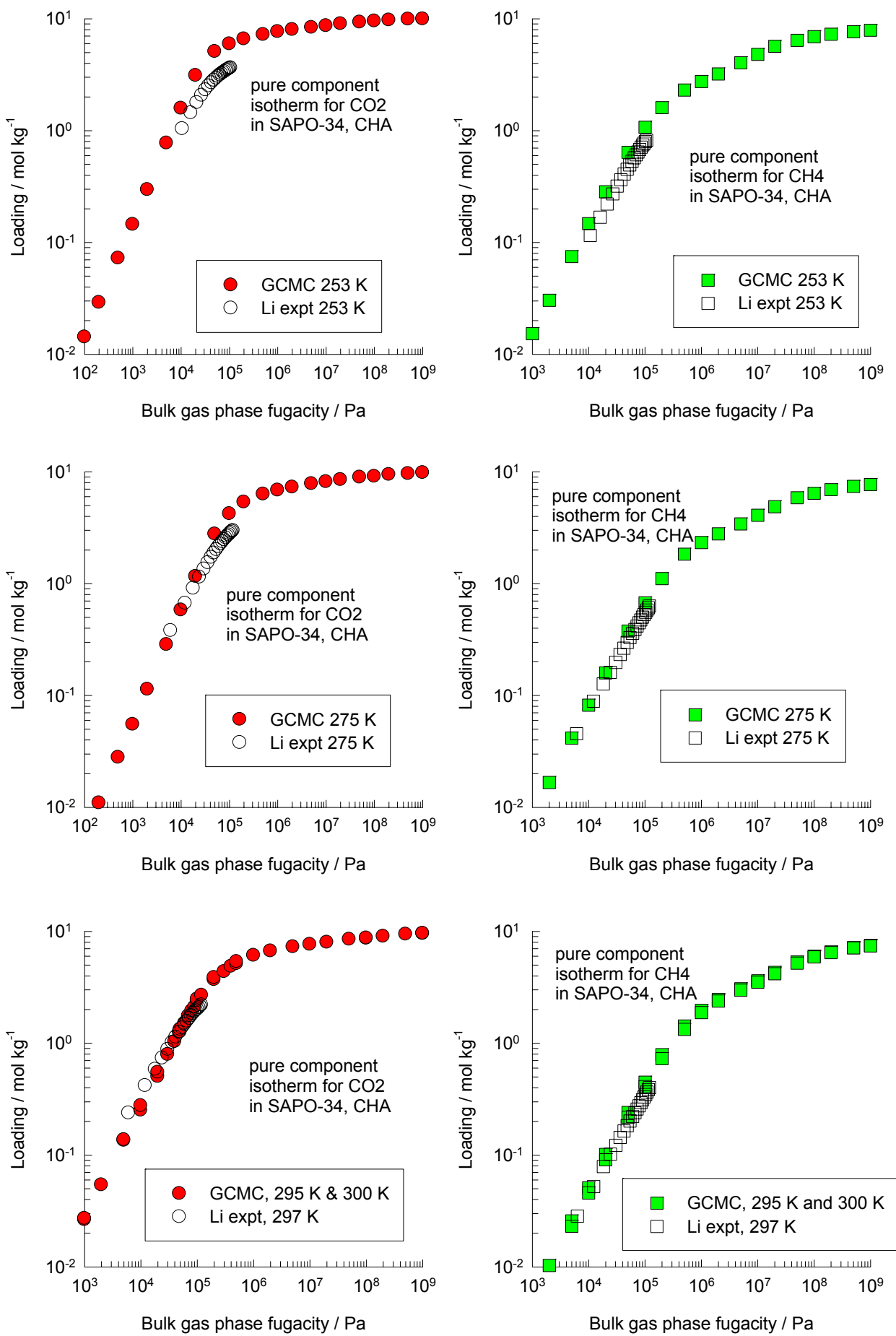


Figure 3

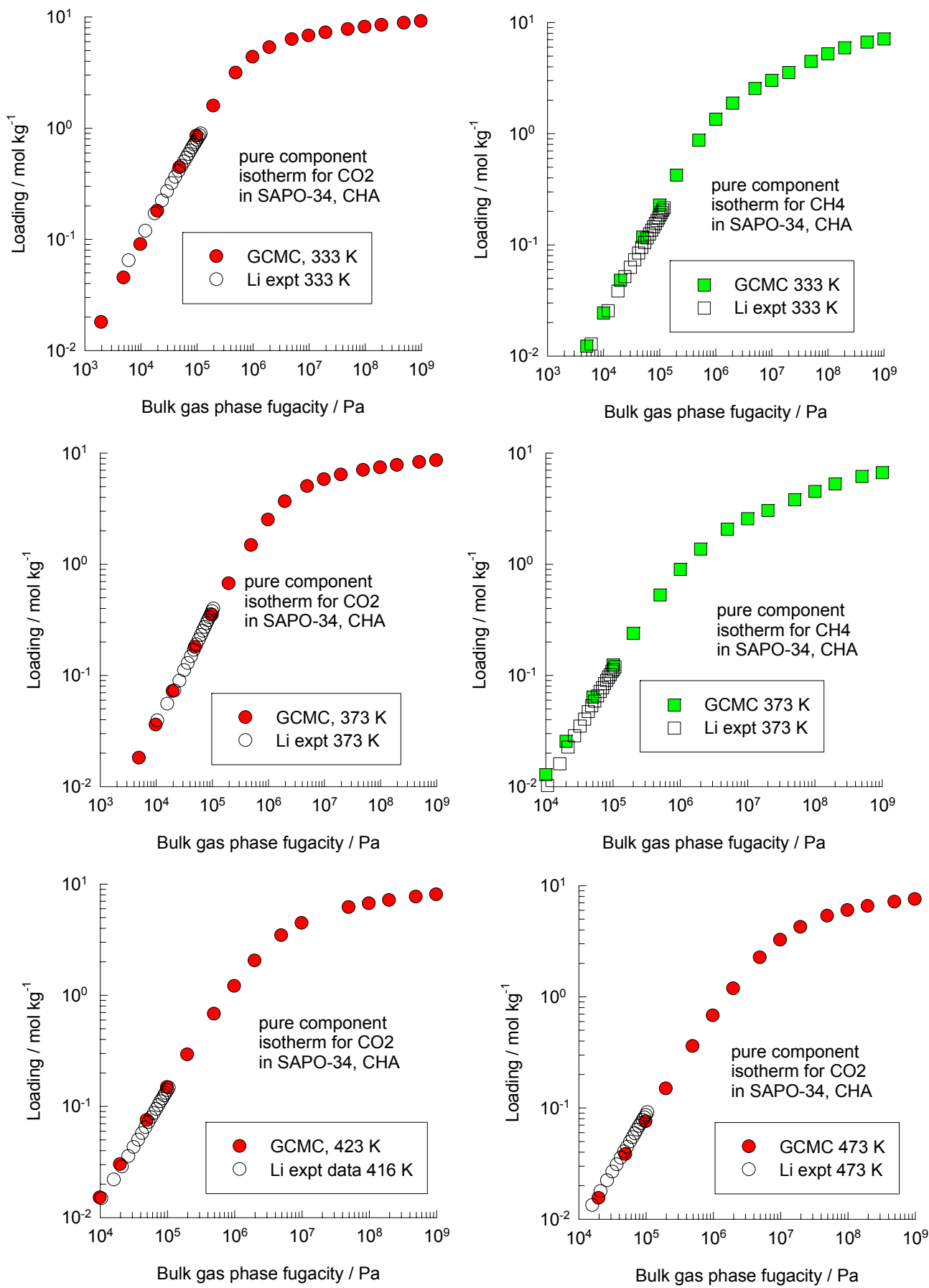
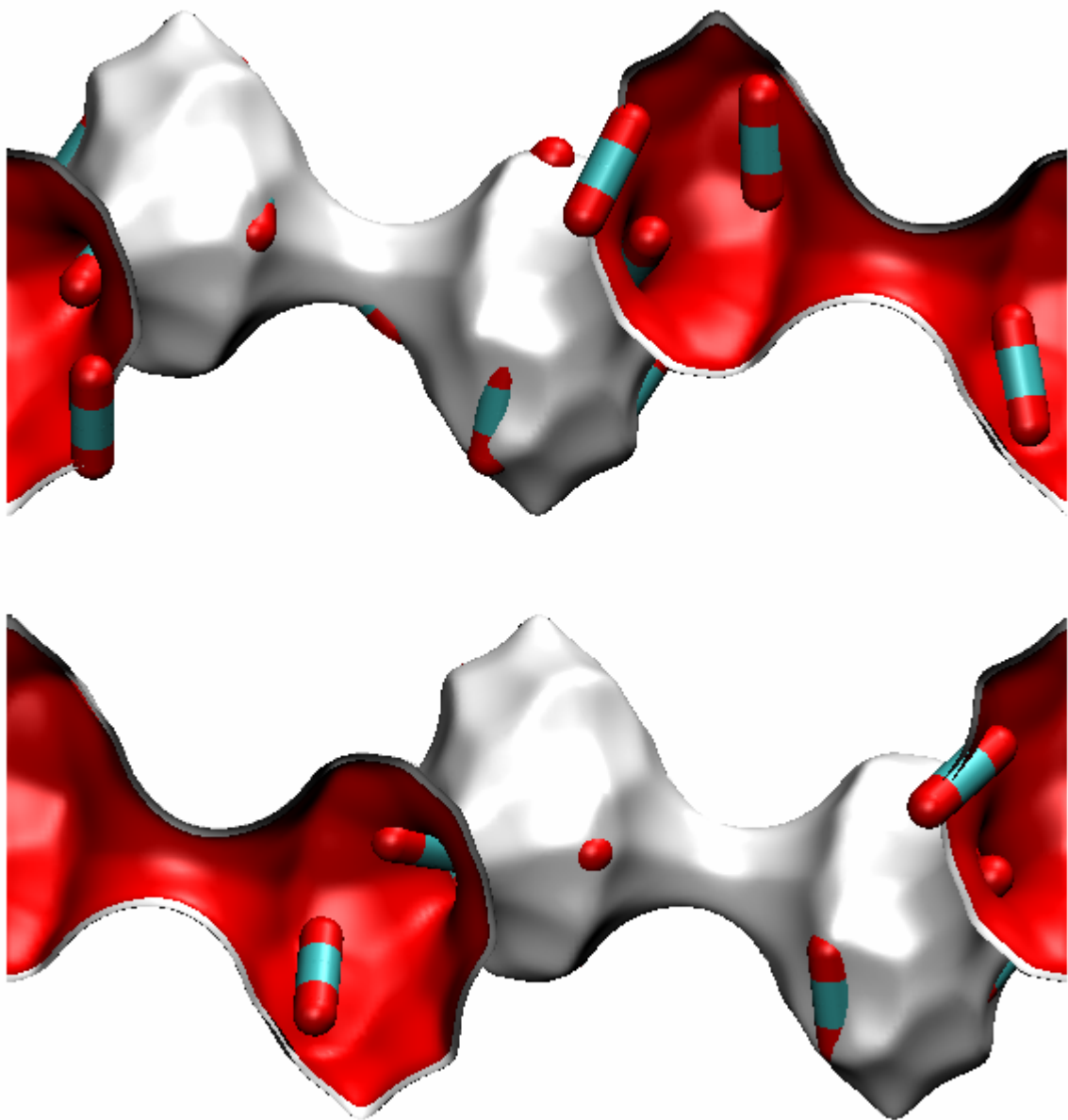


Figure 4

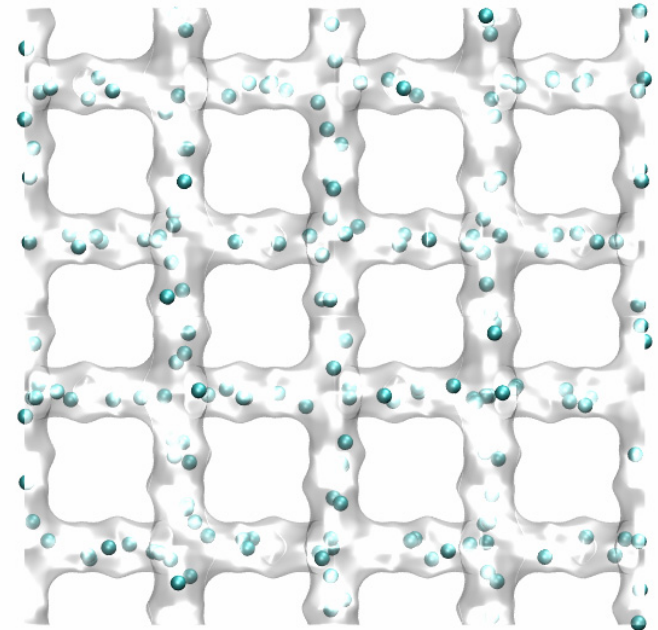
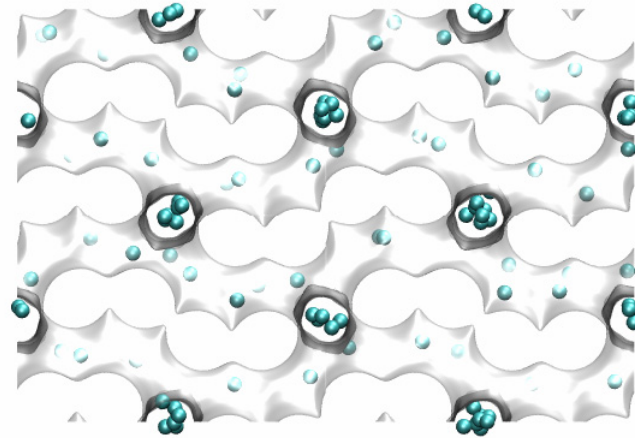


# Appendix B

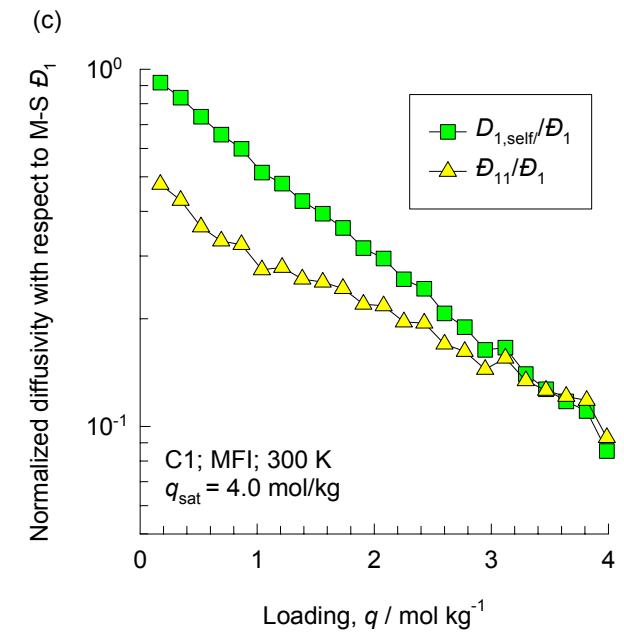
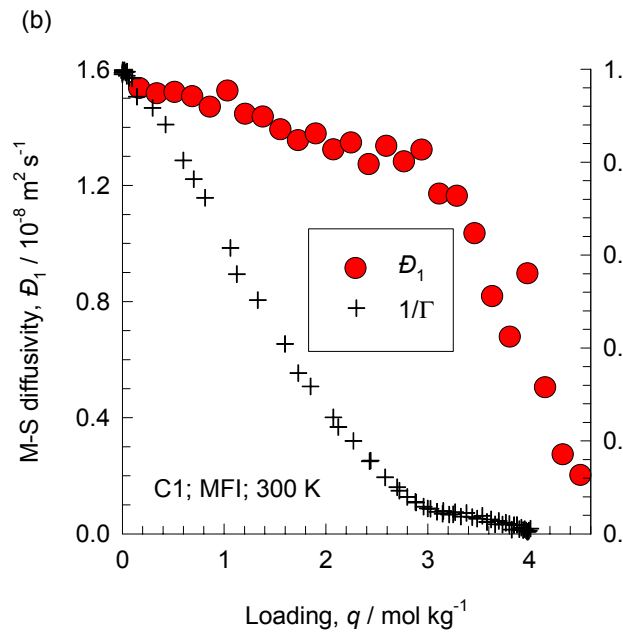
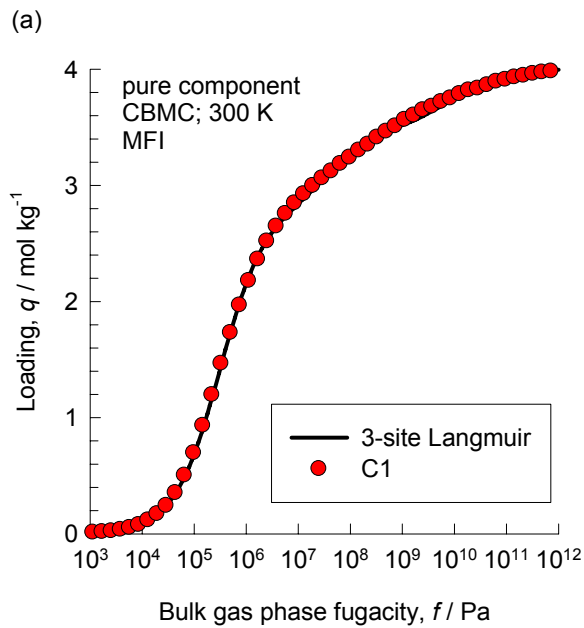
GCMC and MD simulation results for  
adsorption and diffusion of CH<sub>4</sub> and CO<sub>2</sub>  
in different zeolite structures

MFI

C1, 1000 kPa, 300 K

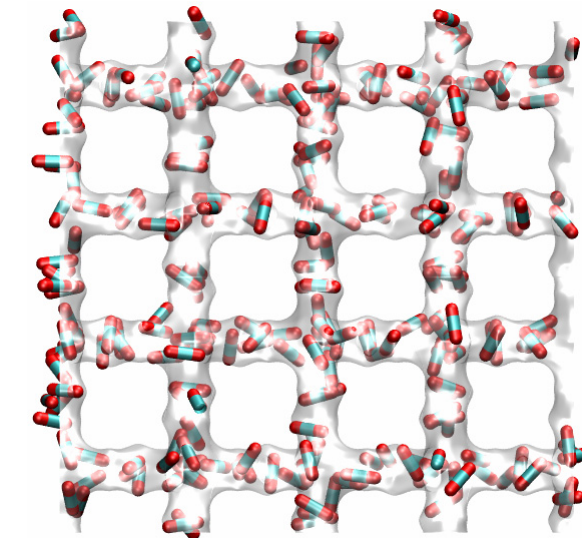
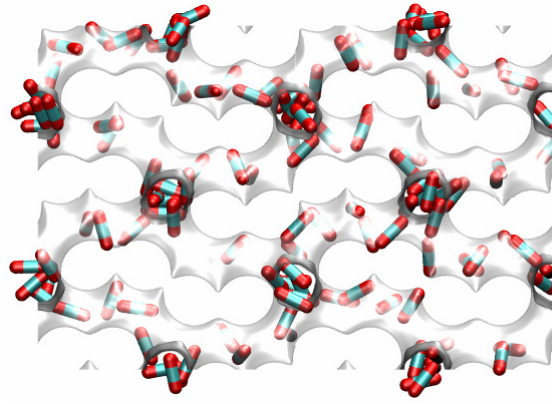


$$D_i(0) = 1.45 \times 10^{-8} \text{ m}^2 \text{ s}^{-1}$$

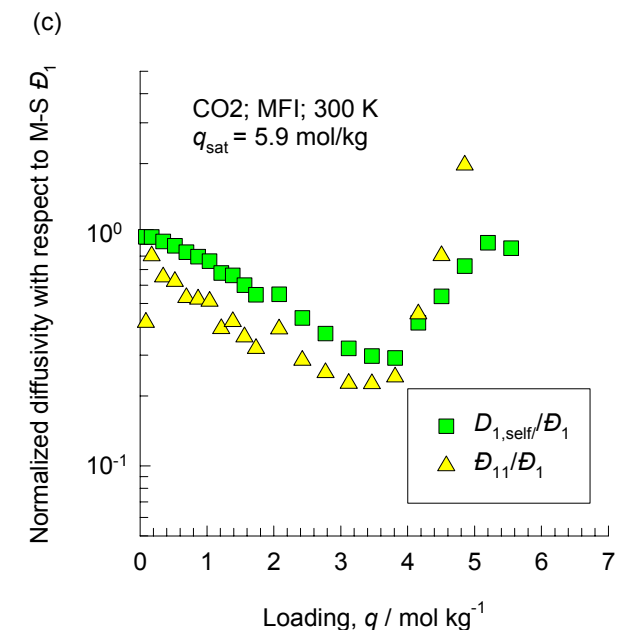
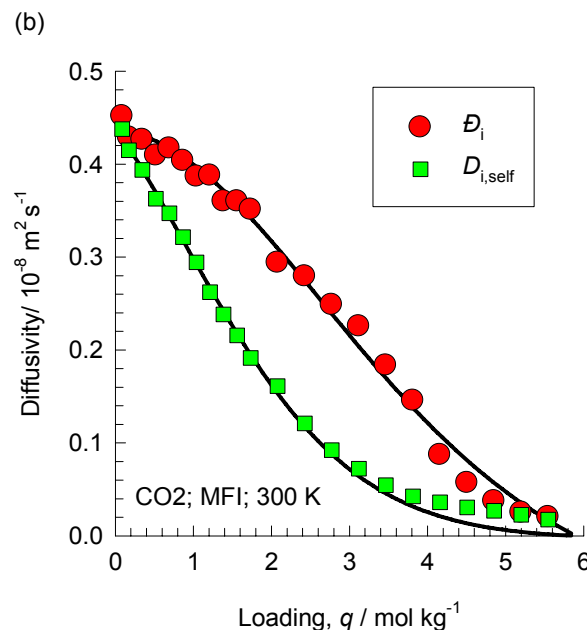
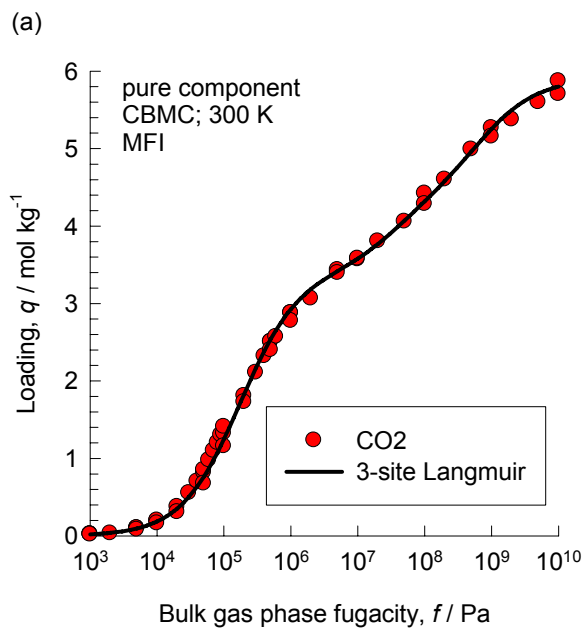


MFI

CO<sub>2</sub>, 1000 kPa, 300 K

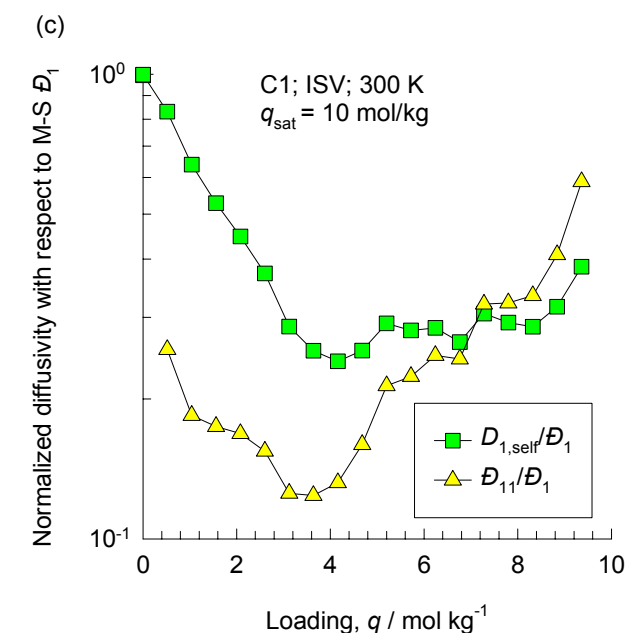
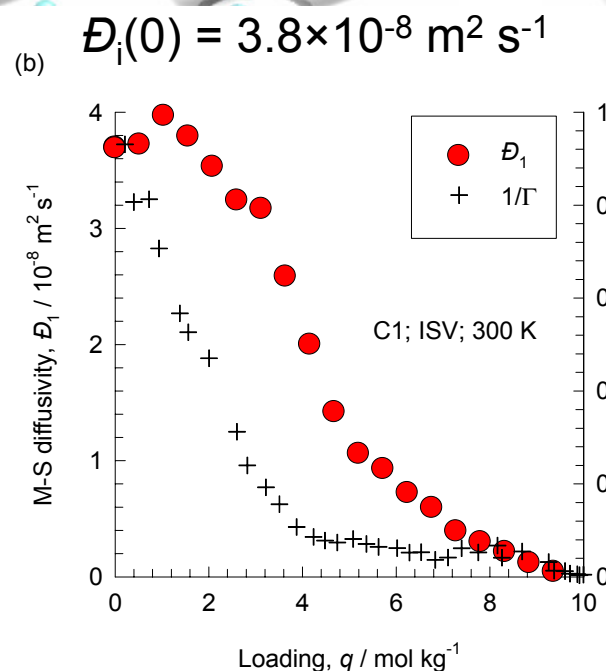
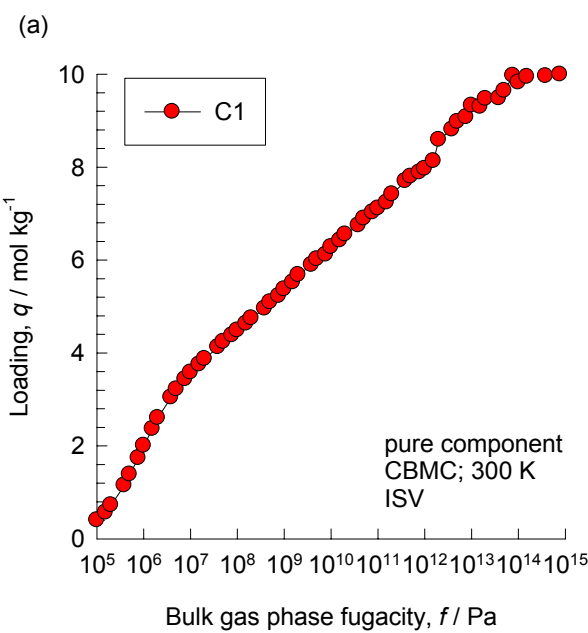
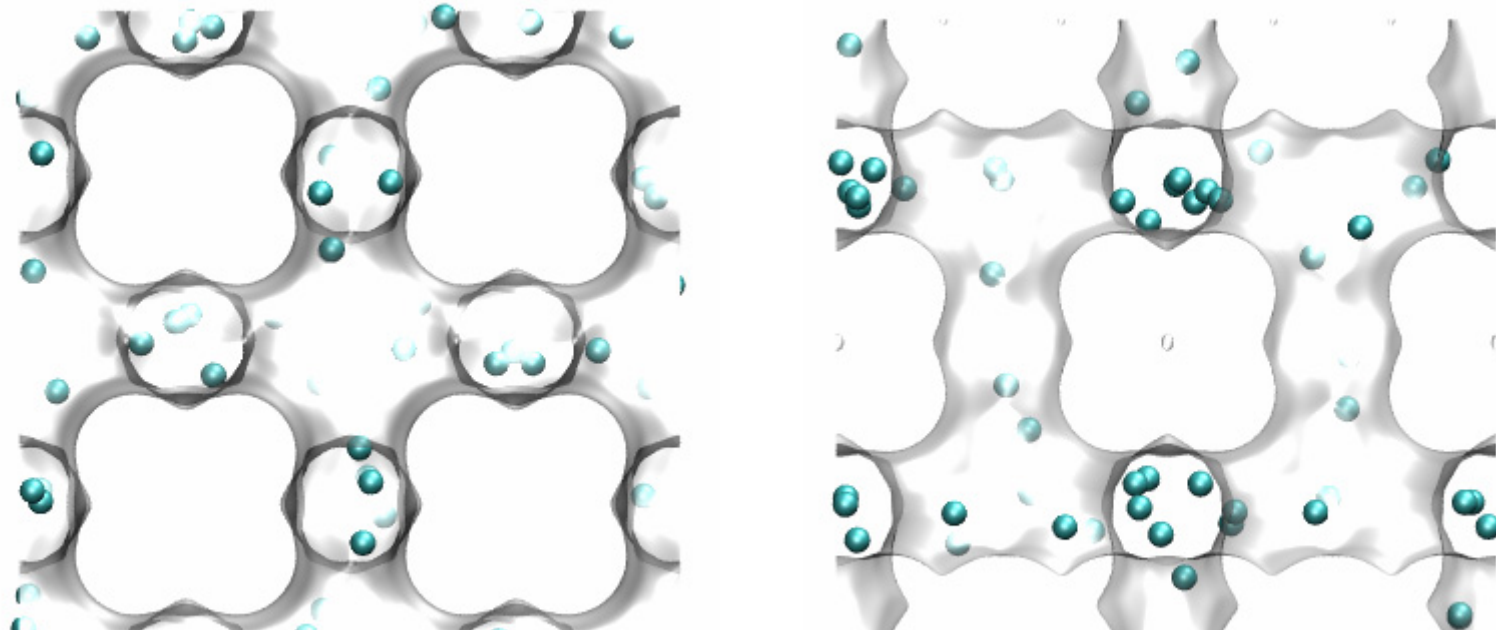


$$D_i(0) = 0.44 \times 10^{-8} \text{ m}^2 \text{ s}^{-1}$$



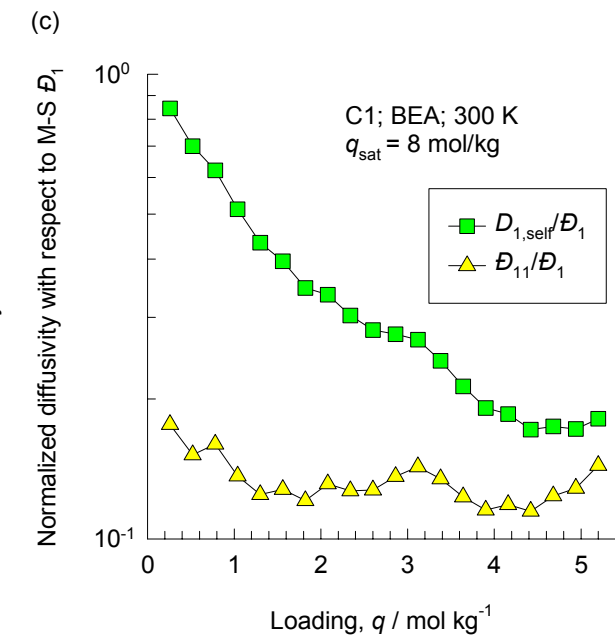
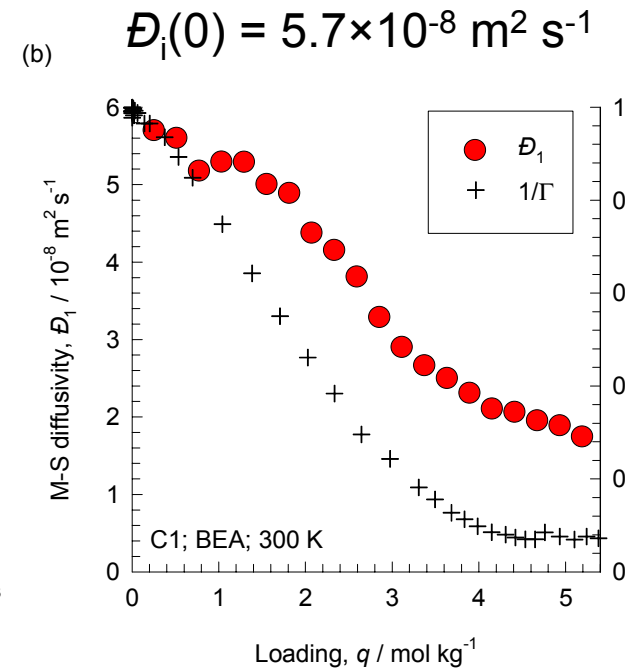
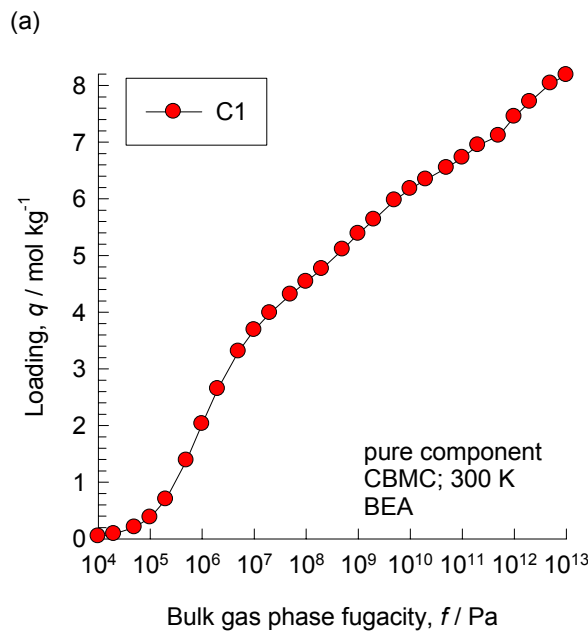
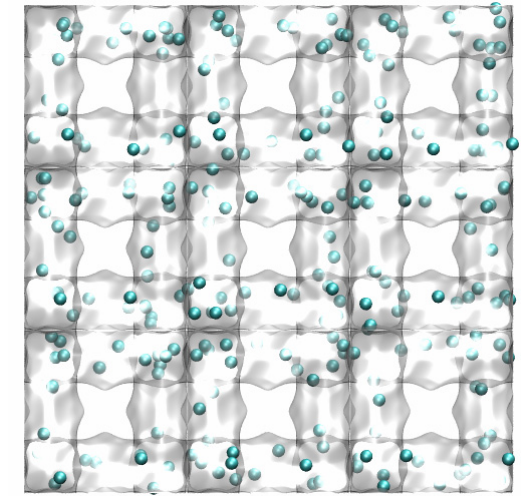
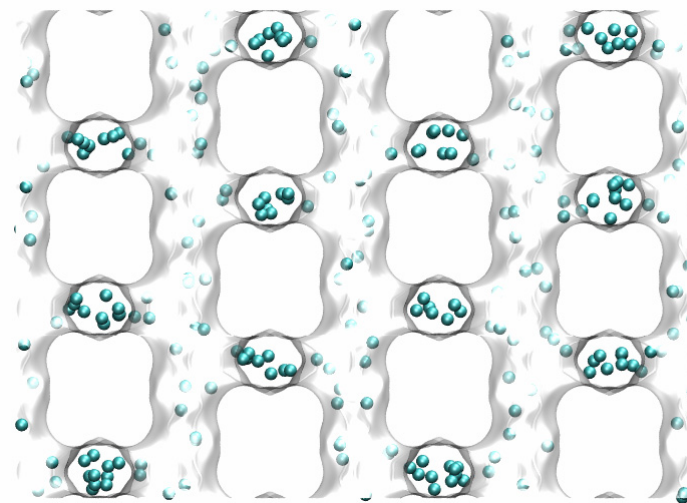
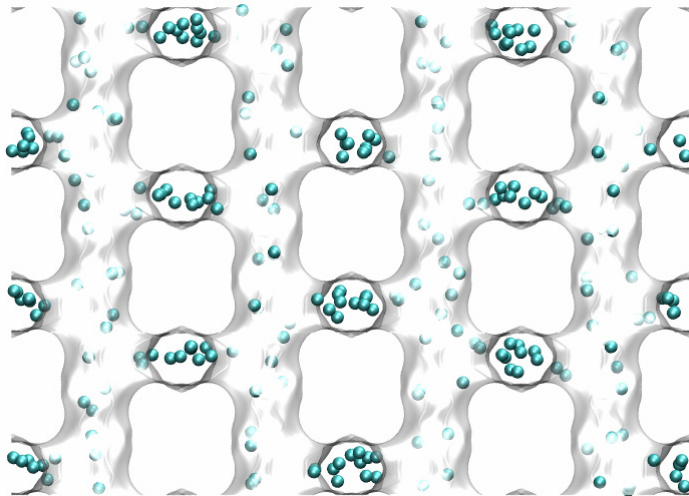
ISV

C1, 1000 kPa, 300 K

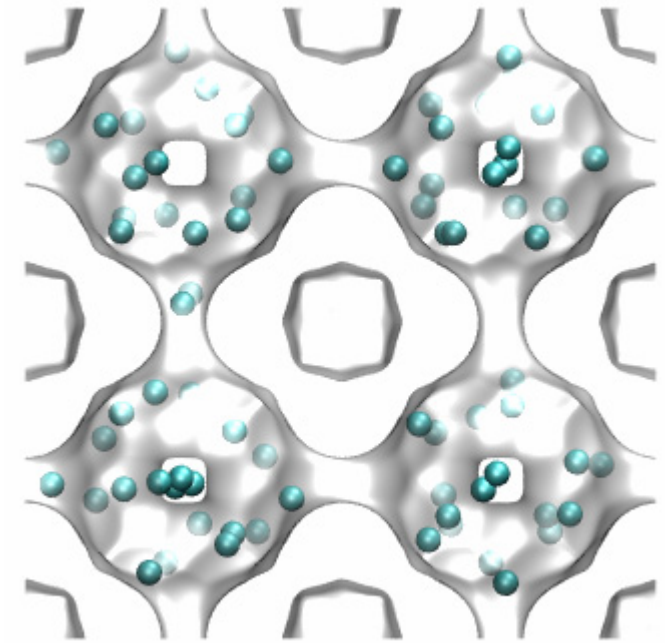
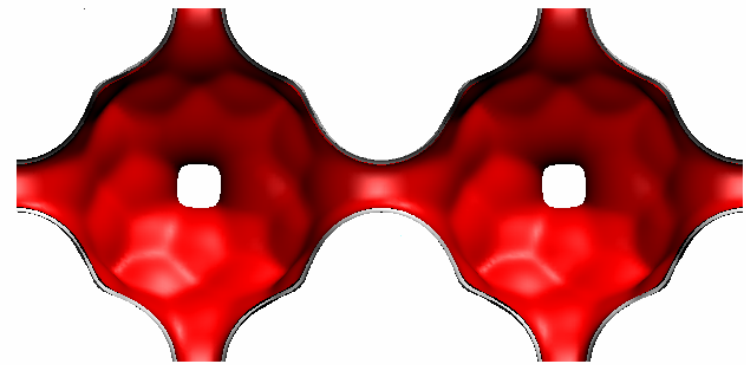


BEA

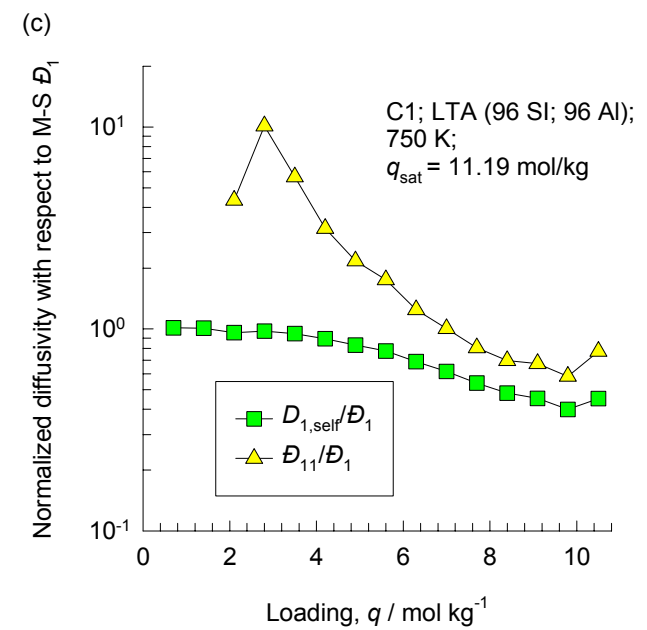
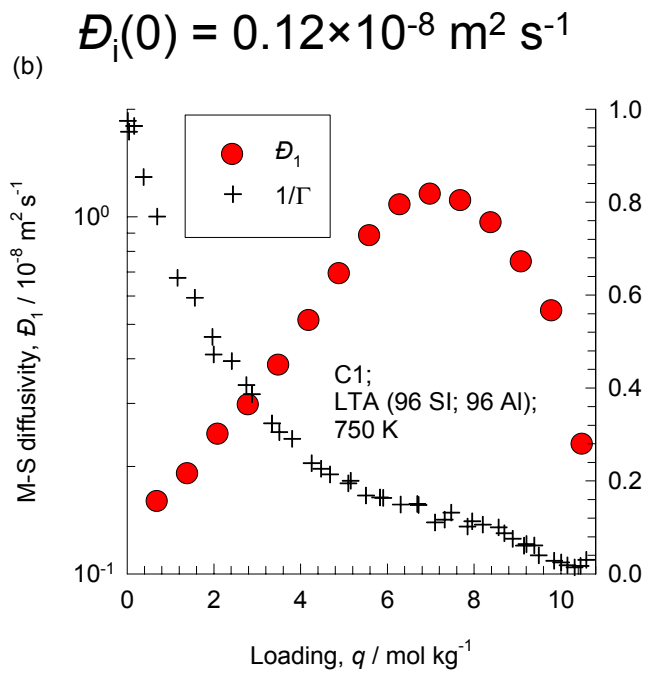
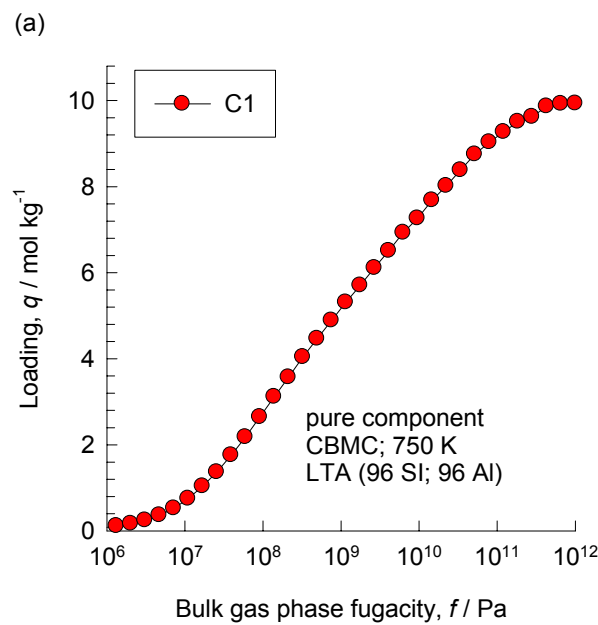
C1, 10 MPa, 300 K



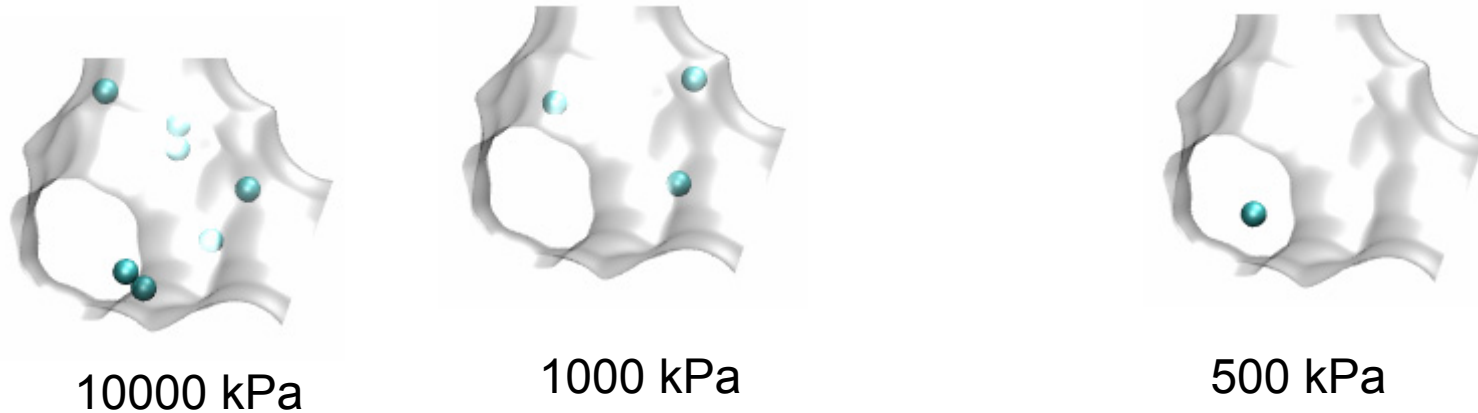
# LTA (96 Si, 96 Al)



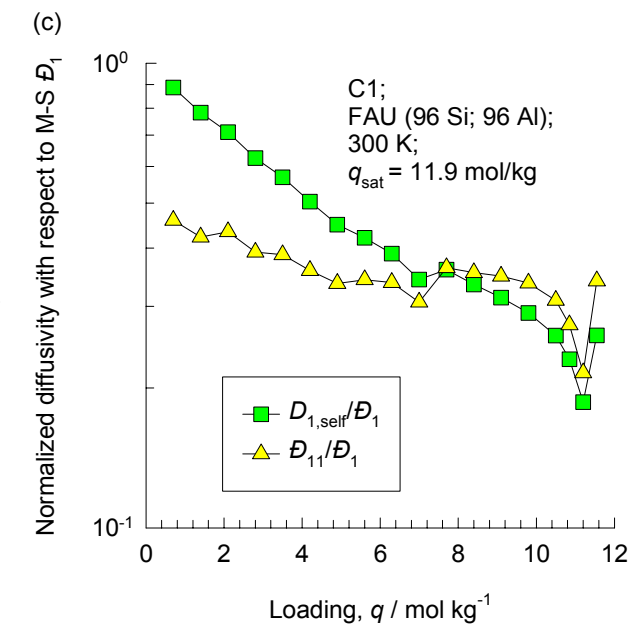
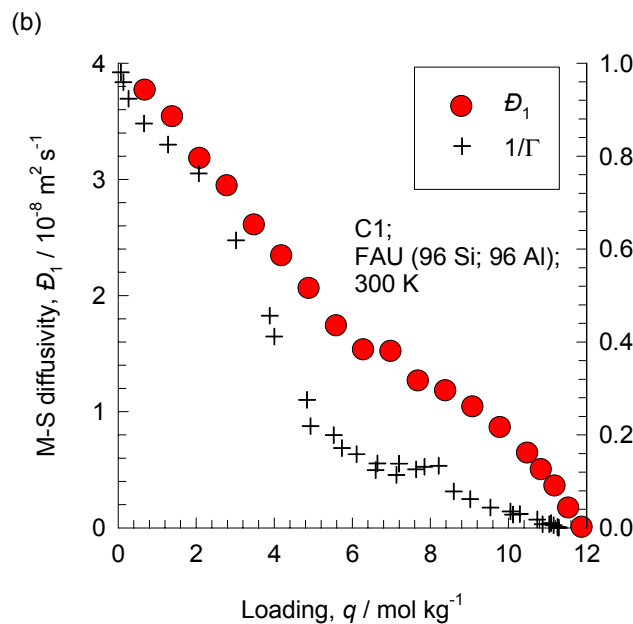
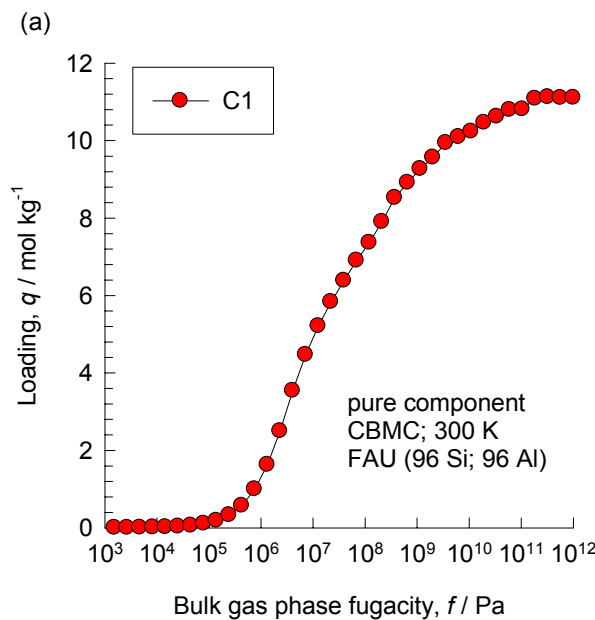
C1, 10000 MPa, 750 K



# FAU (96 Si; 96 Al), C1, 300 K

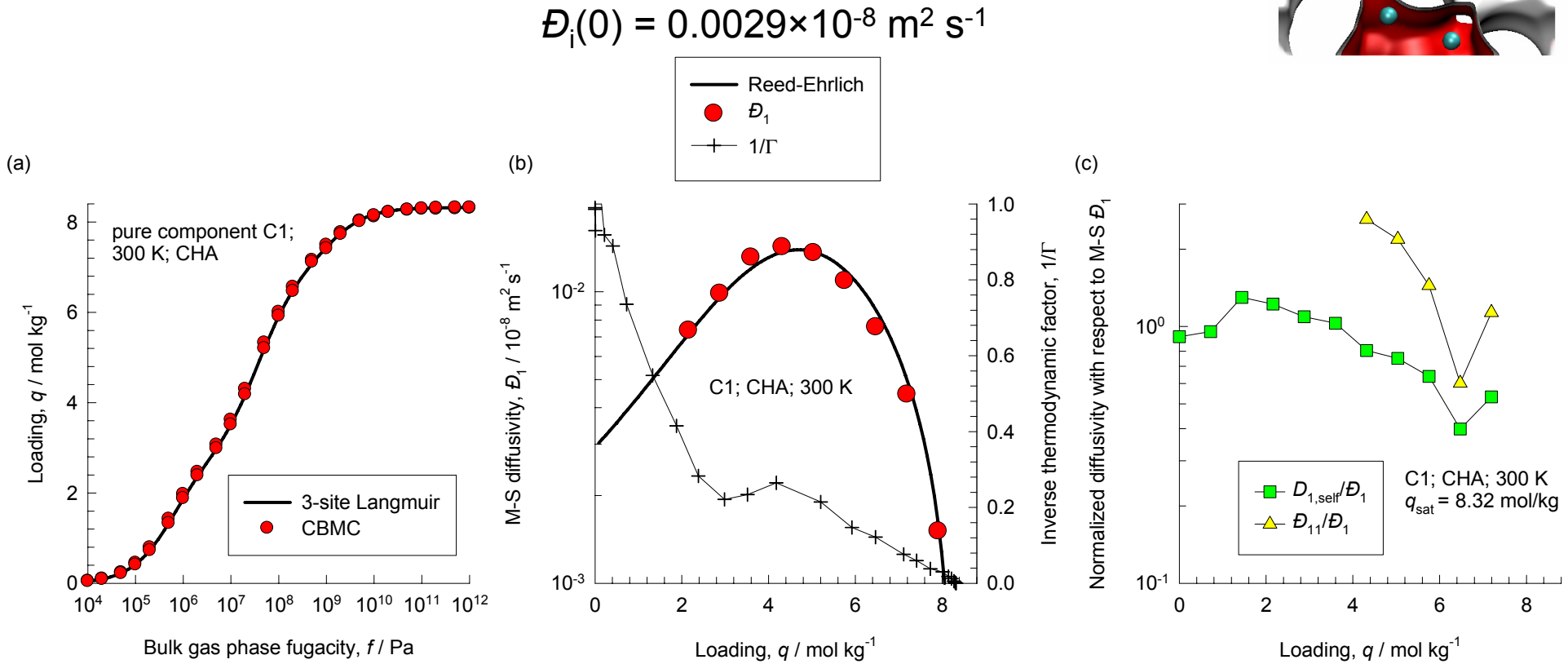


$$\mathcal{D}_i(0) = 4 \times 10^{-8} \text{ m}^2 \text{ s}^{-1}$$



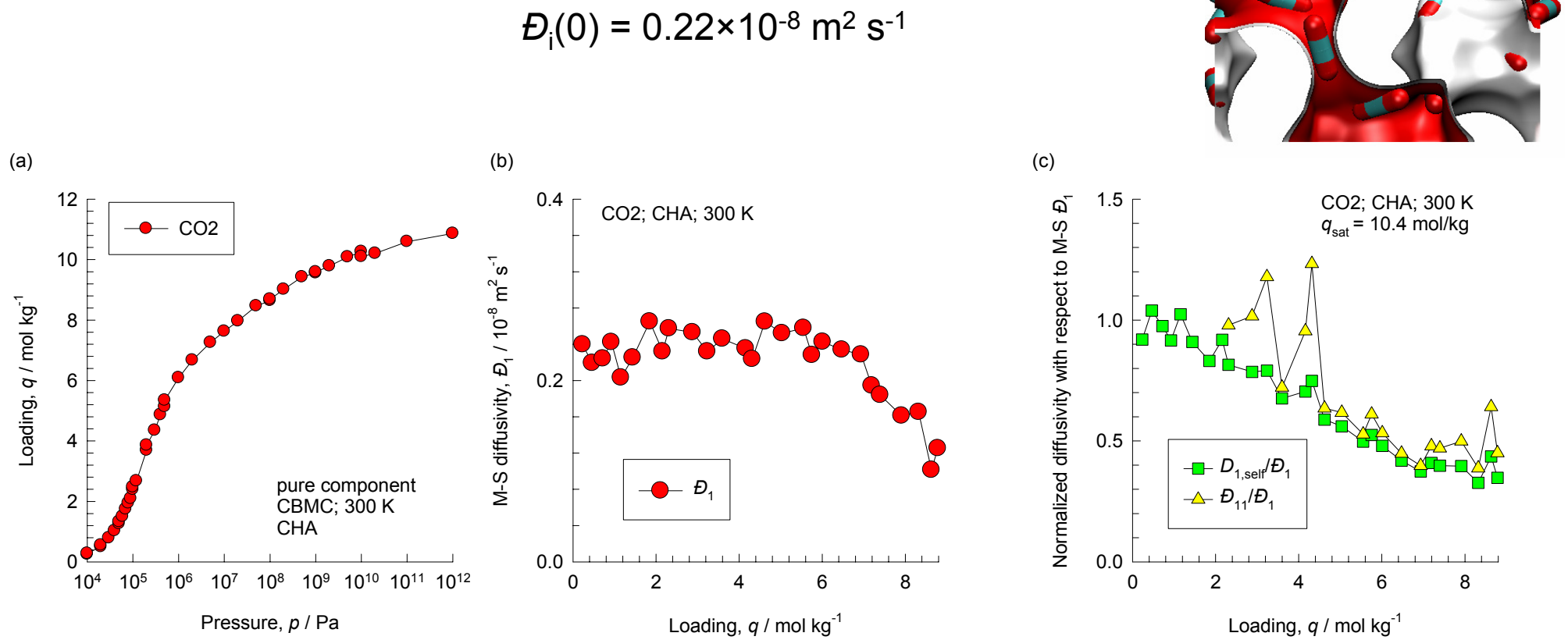
CHA

C1, 300 K, 1000 MPa

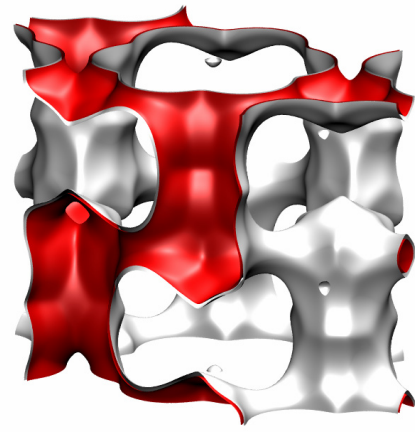


CHA

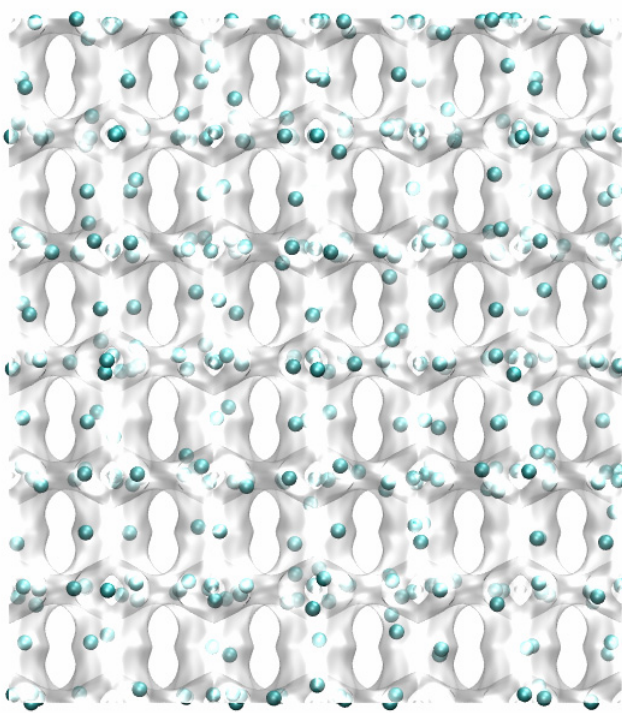
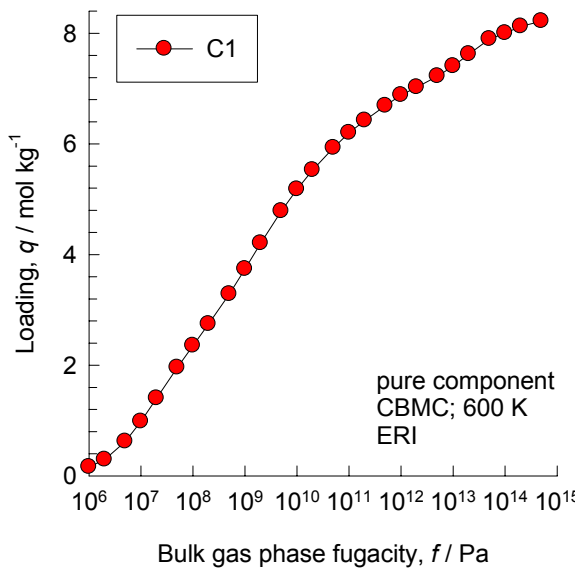
CO<sub>2</sub>, 300 K, 1000 MPa



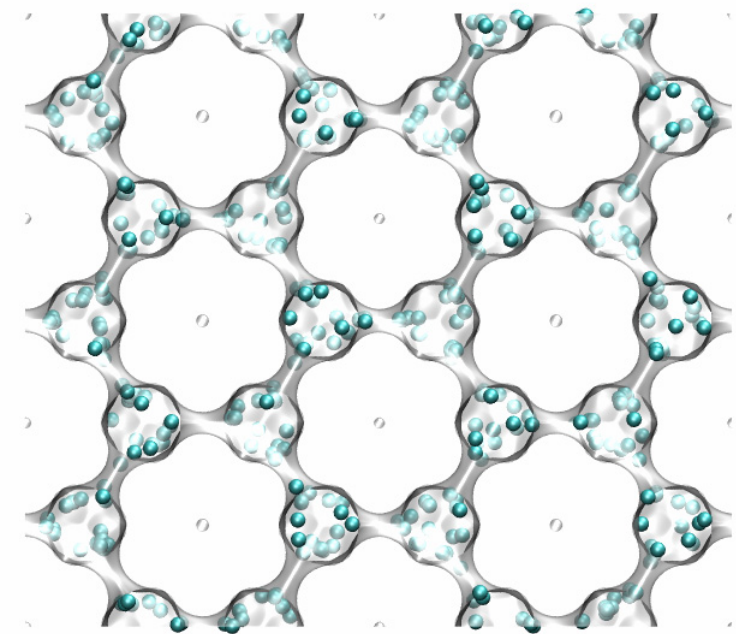
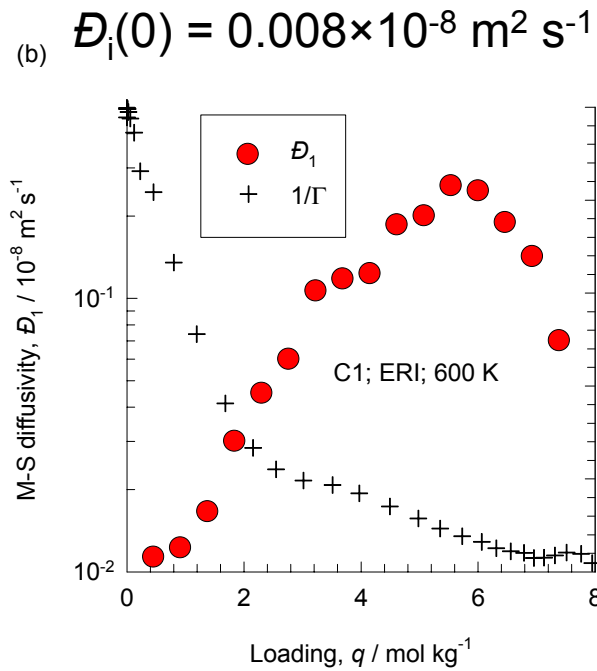
ERI



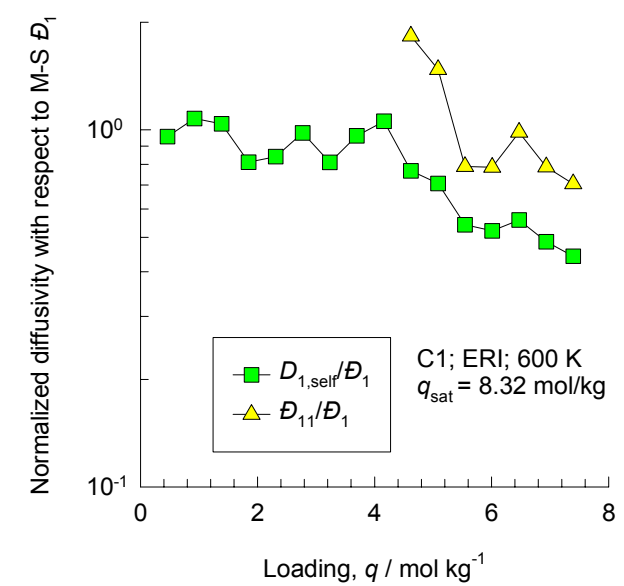
(a)

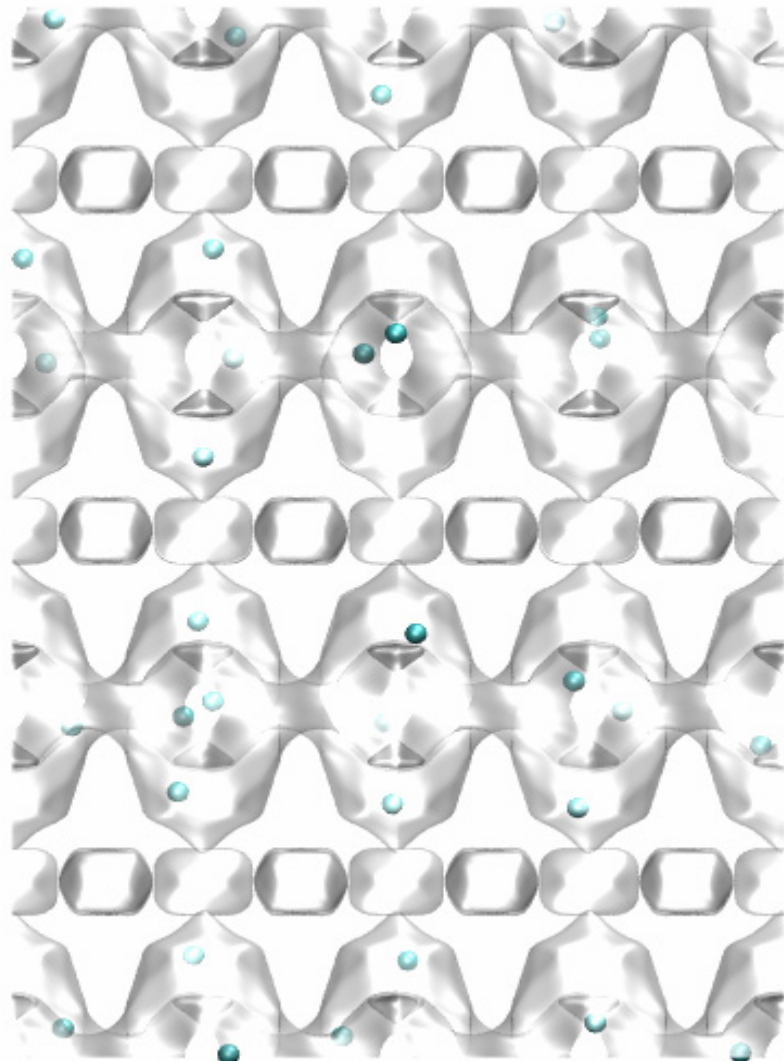


(b)



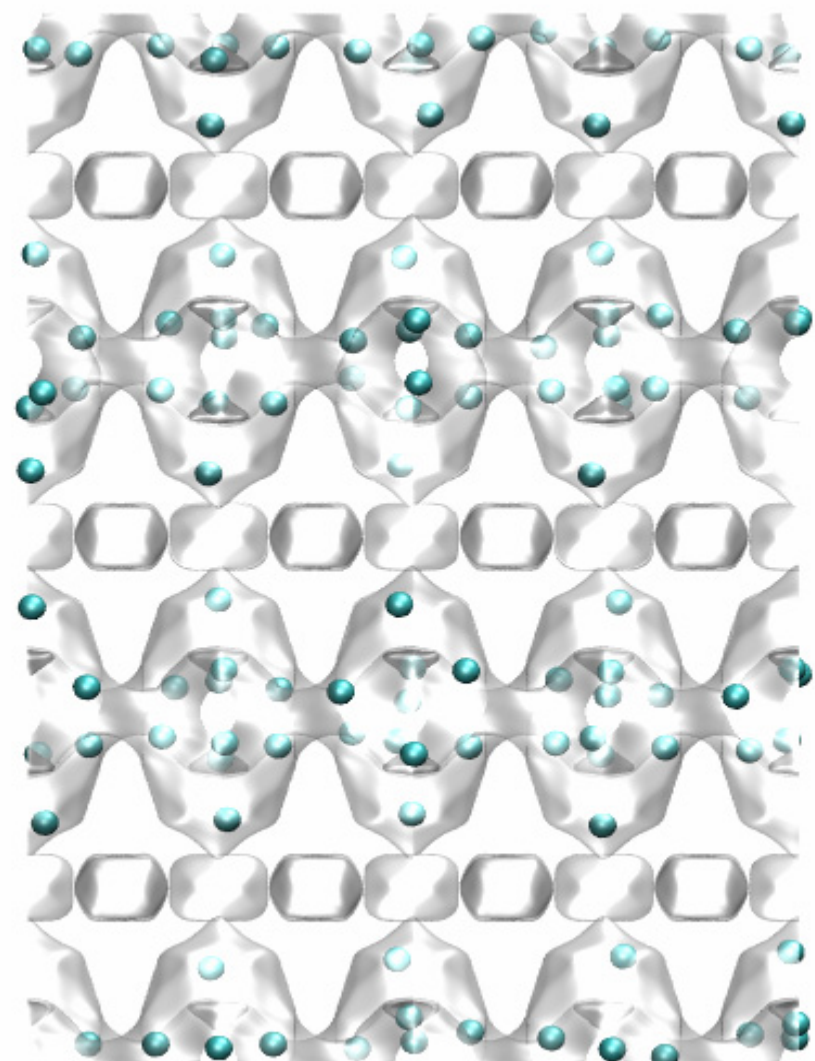
(c)



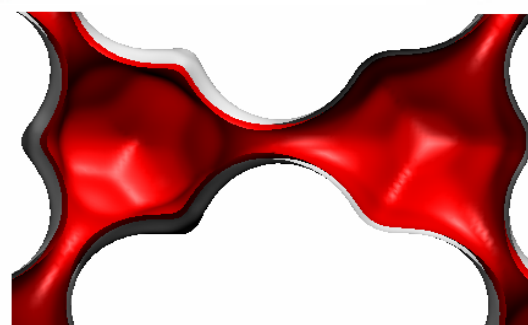


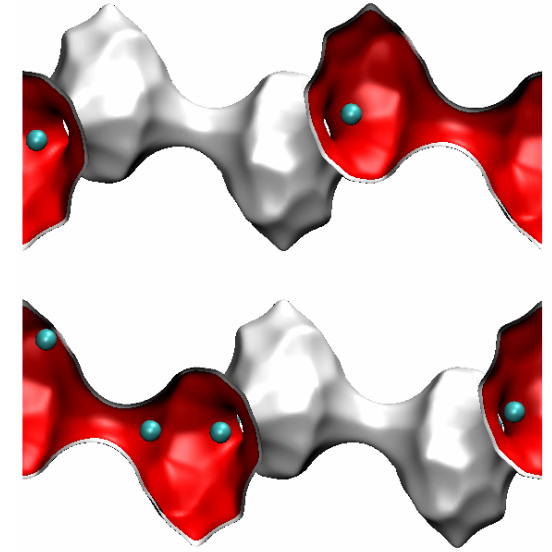
1 MPa

DDR, C1



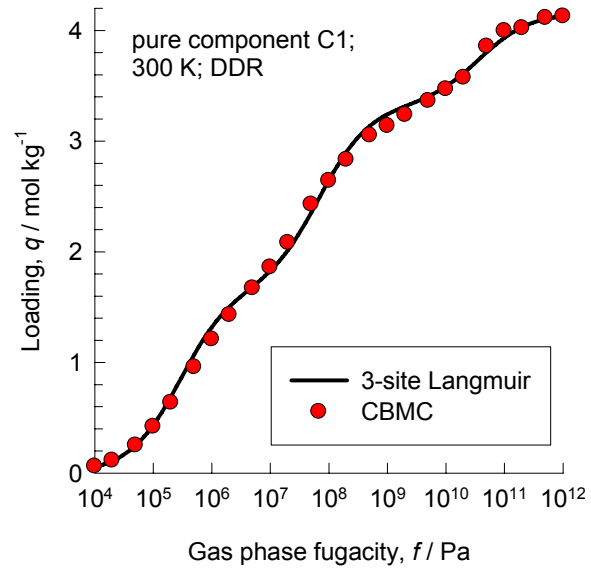
1000 MPa



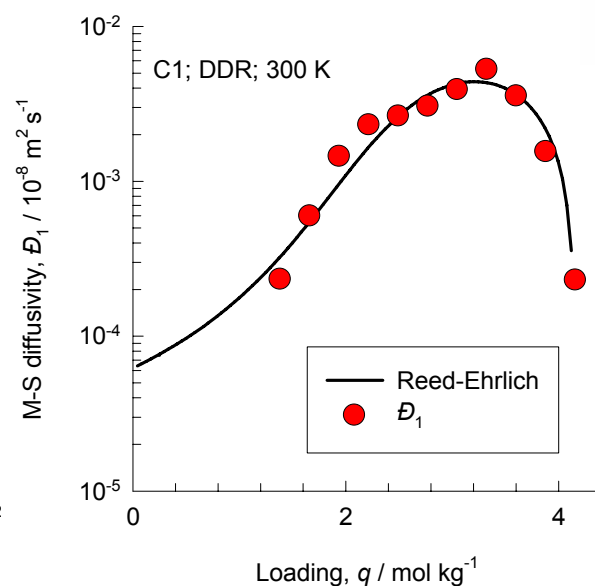


$$\mathcal{D}_i(0) = 0.0000623 \times 10^{-8} \text{ m}^2 \text{ s}^{-1}$$

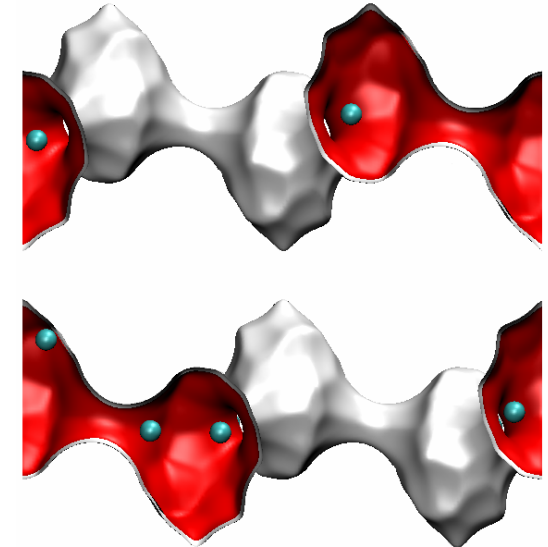
(a)



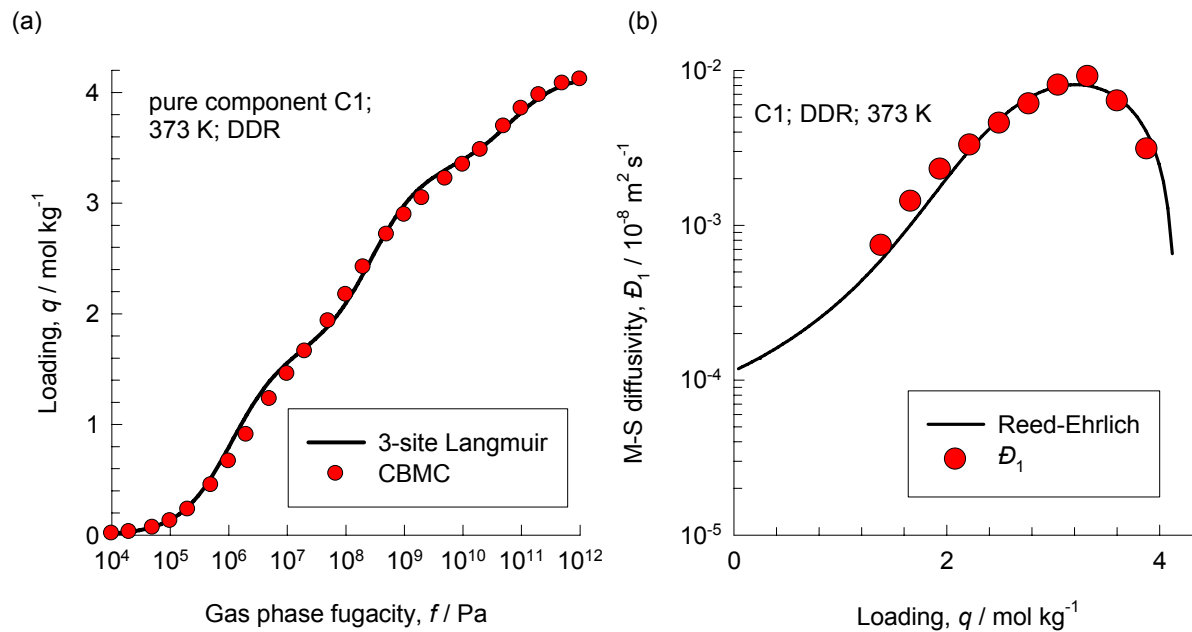
(b)



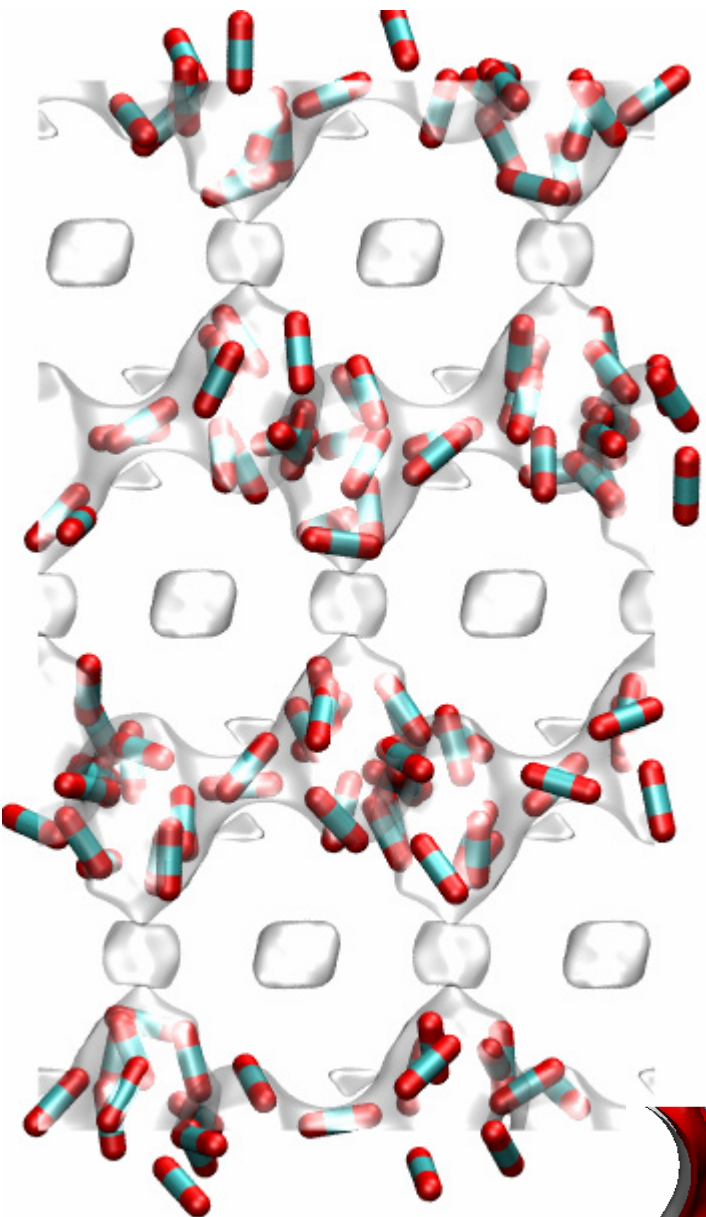
*For DDR the self- and M-S diffusivities are very close to each other*



$$\mathcal{D}_i(0) = 0.00011 \times 10^{-8} \text{ m}^2 \text{ s}^{-1}$$

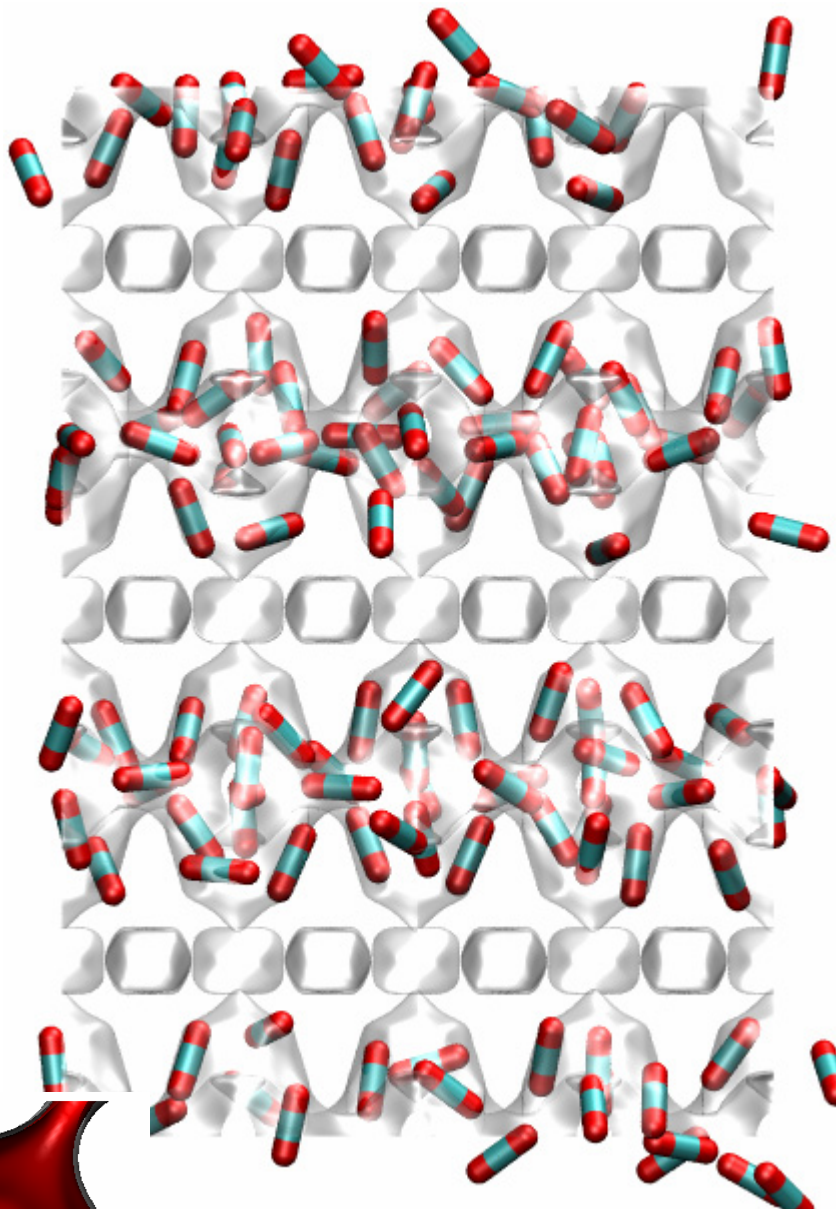


*For DDR the self- and M-S diffusivities are very close to each other*



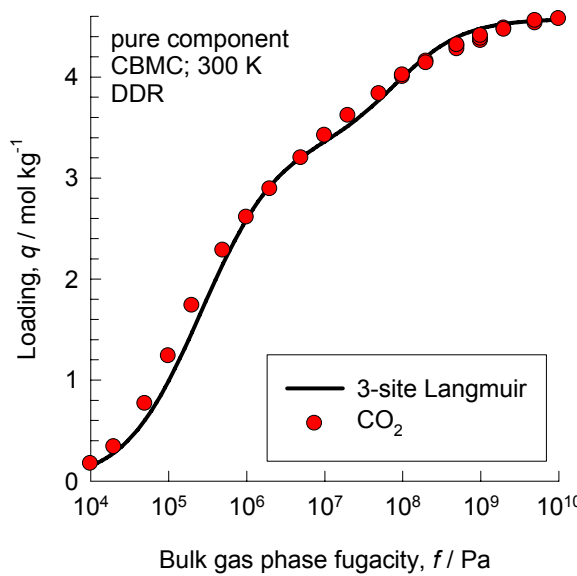
DDR, CO<sub>2</sub>

1000 MPa

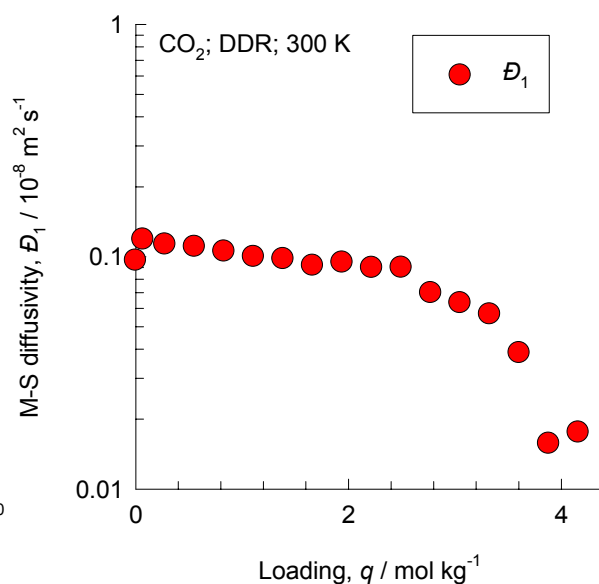


$$\mathcal{D}_i(0) = 0.11 \times 10^{-8} \text{ m}^2 \text{ s}^{-1}$$

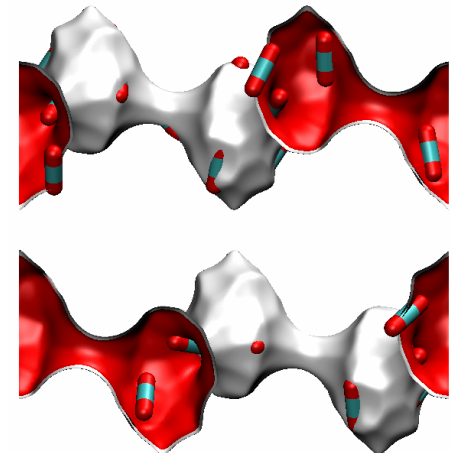
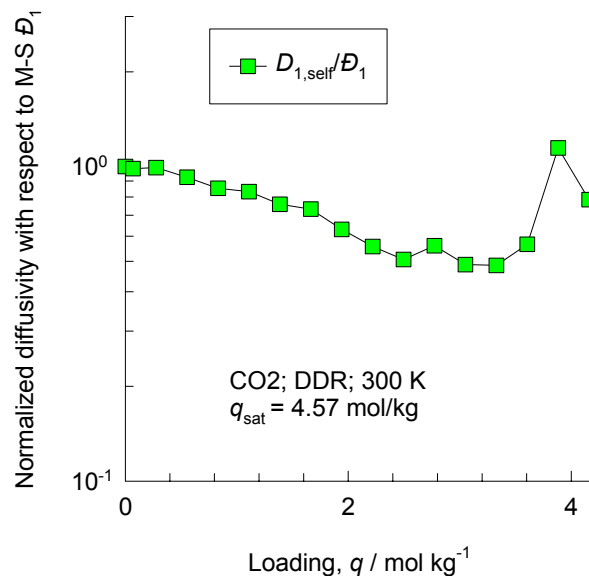
(a)



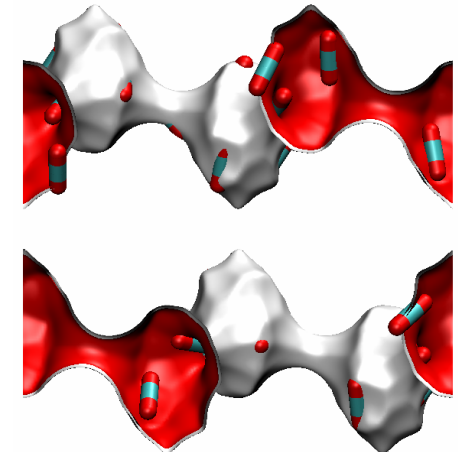
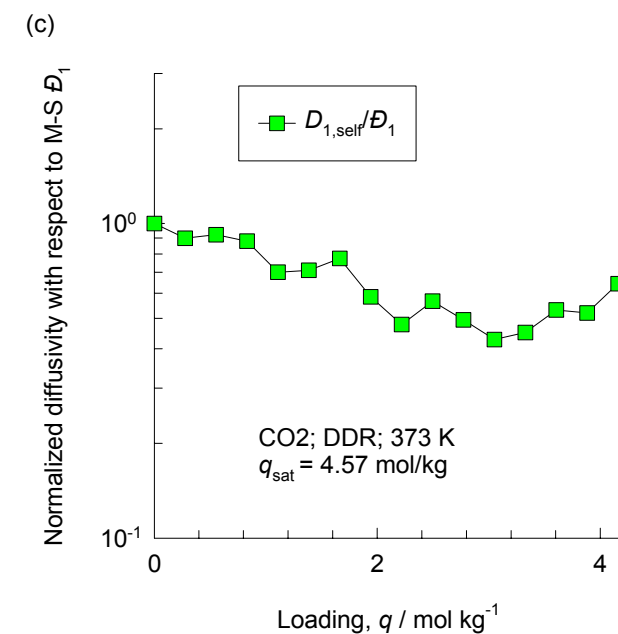
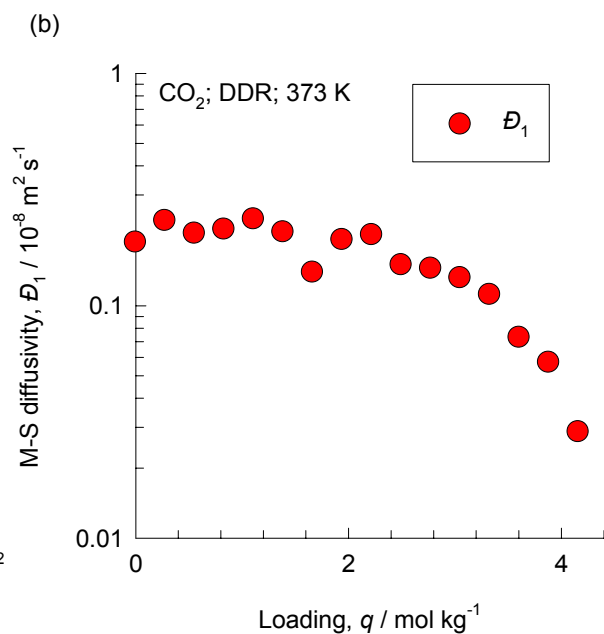
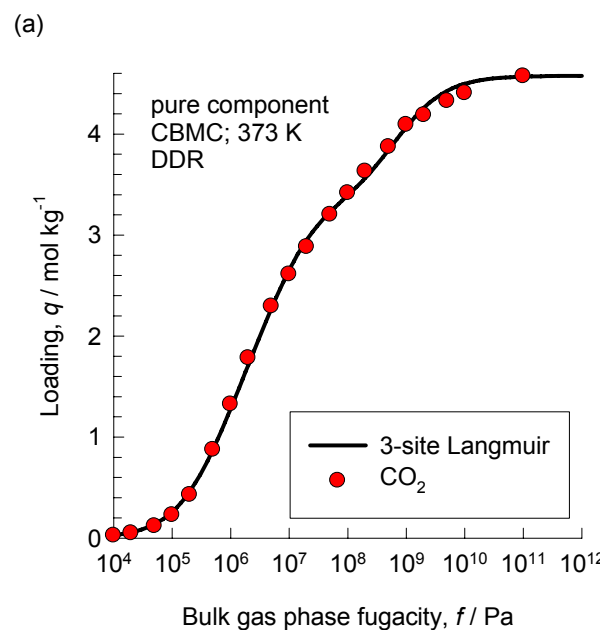
(b)



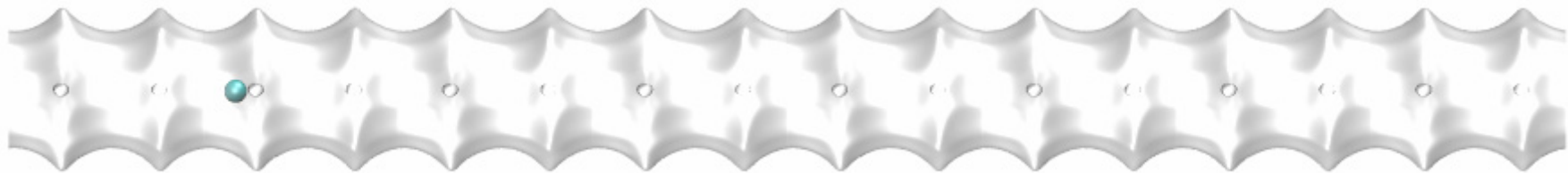
(c)



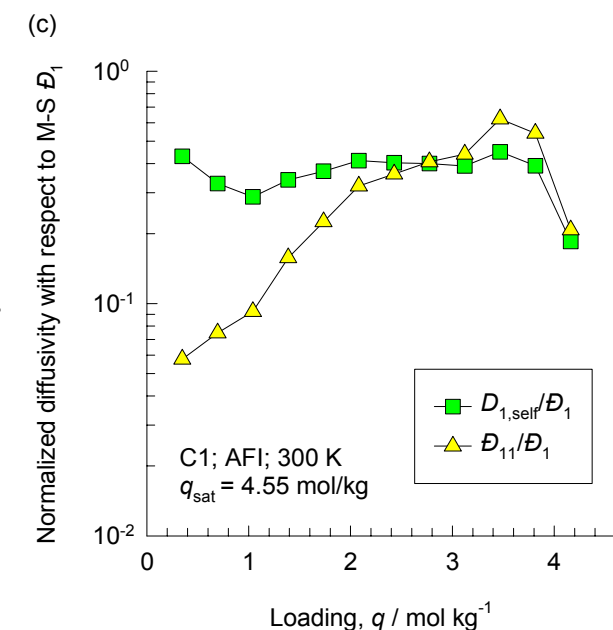
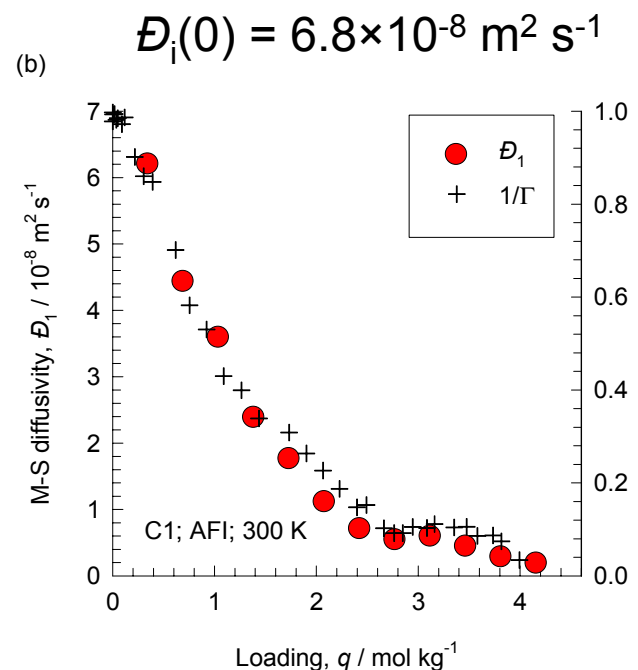
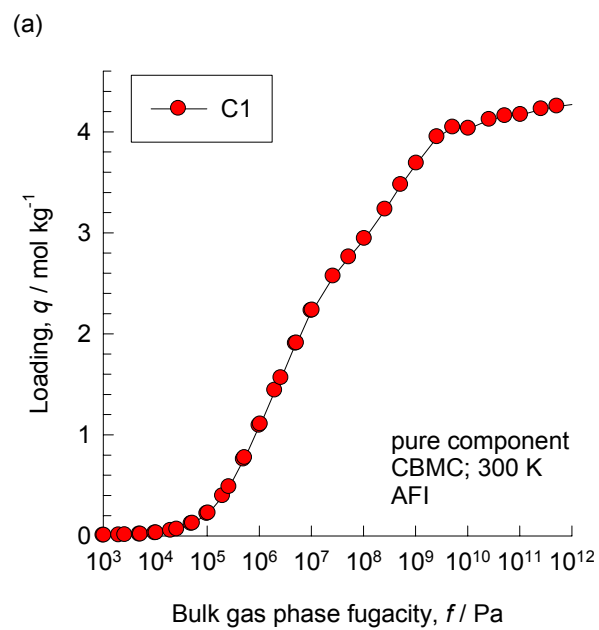
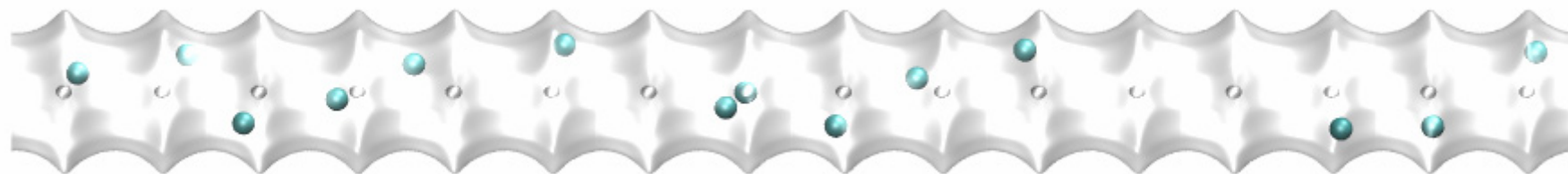
$$\mathcal{D}_i(0) = 0.22 \times 10^{-8} \text{ m}^2 \text{ s}^{-1}$$



AFI, C1, 100 kPa

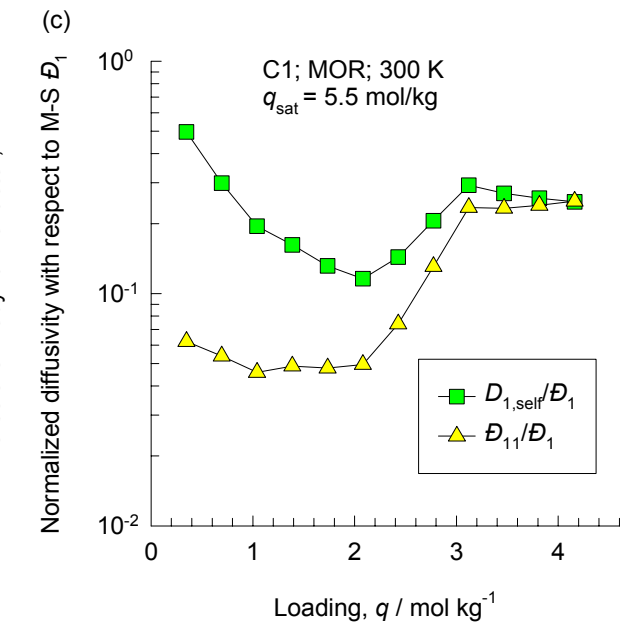
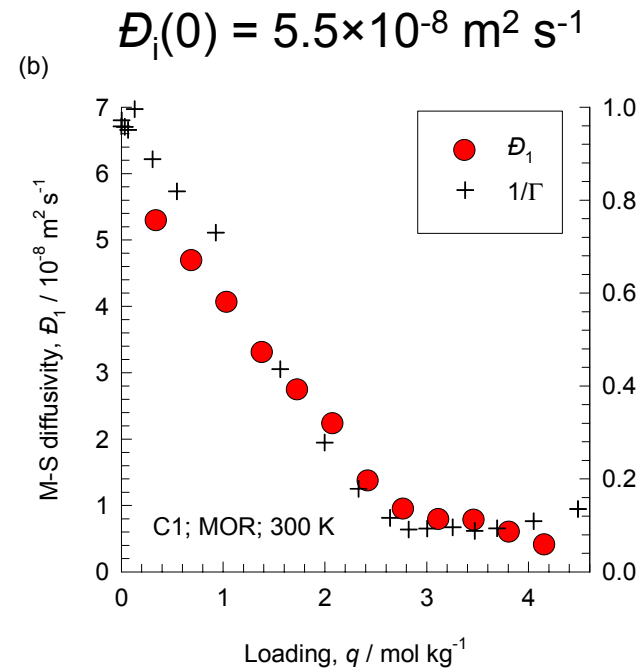
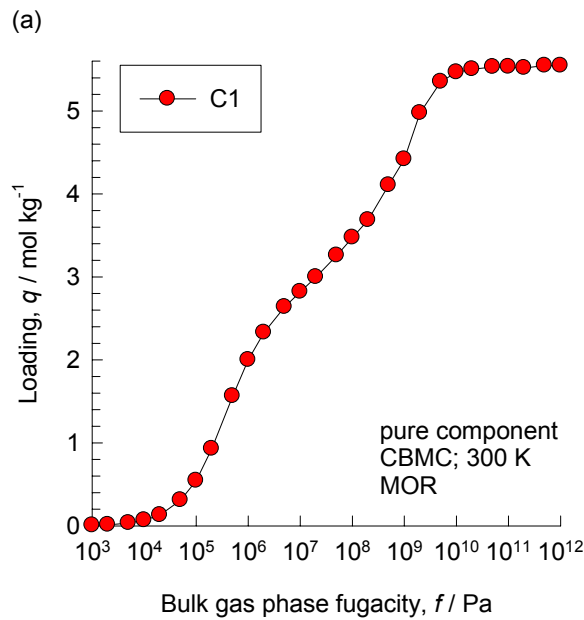
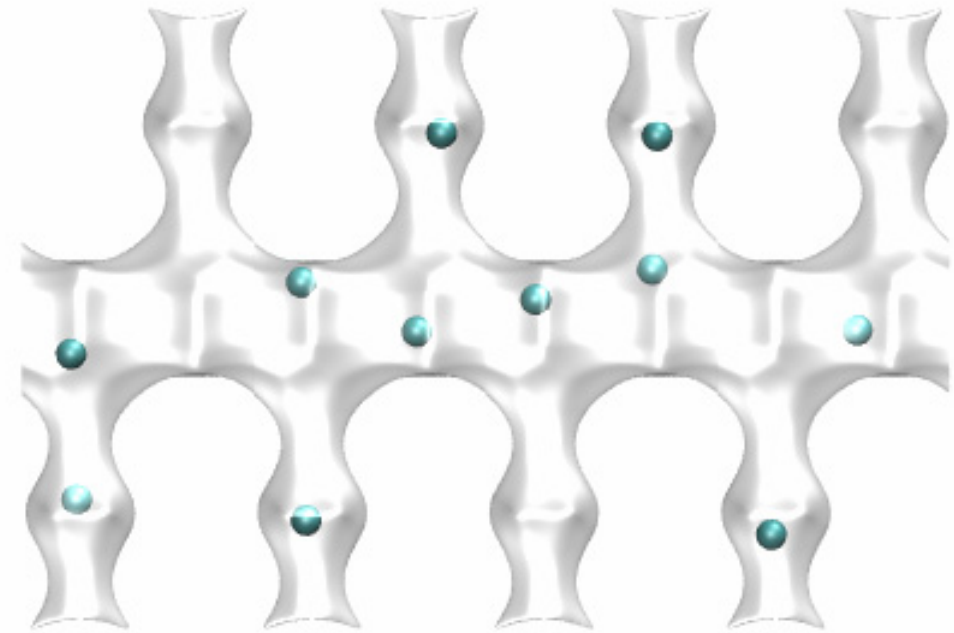


AFI, C1, 1000 kPa



MOR

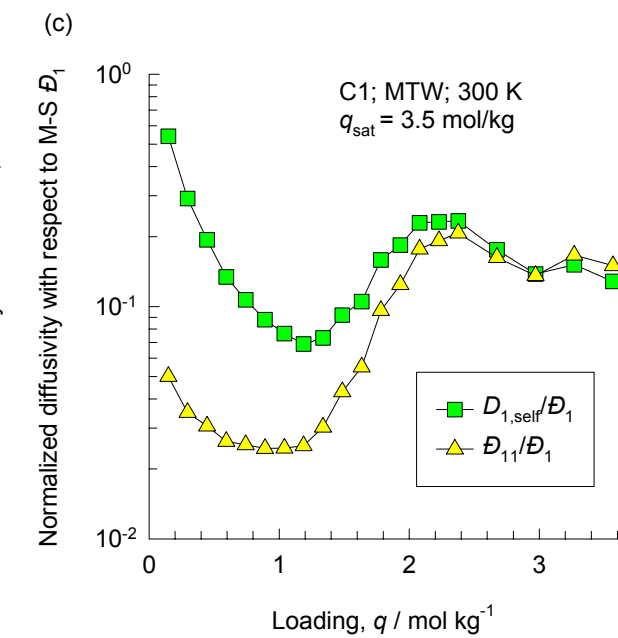
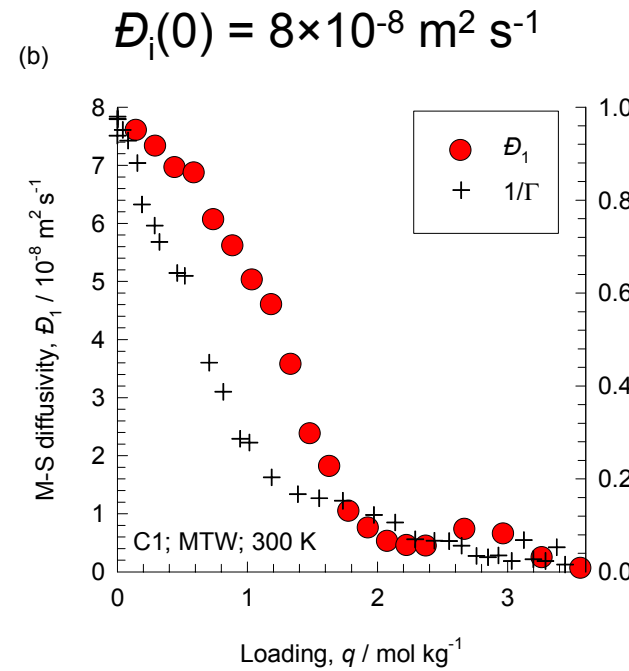
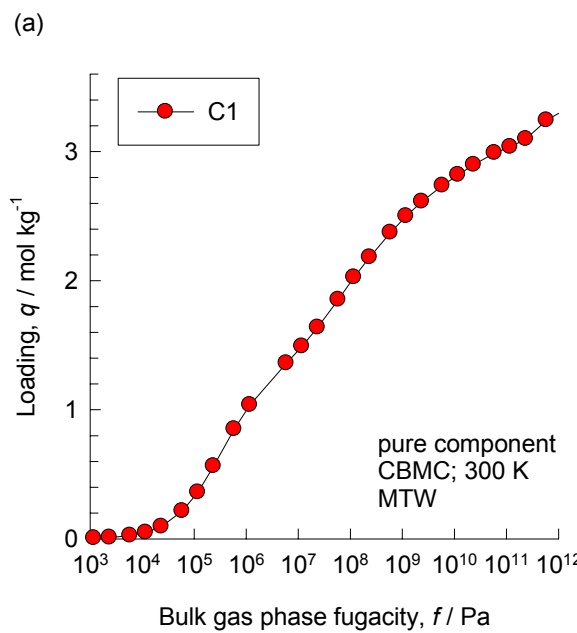
C1, 1000 kPa



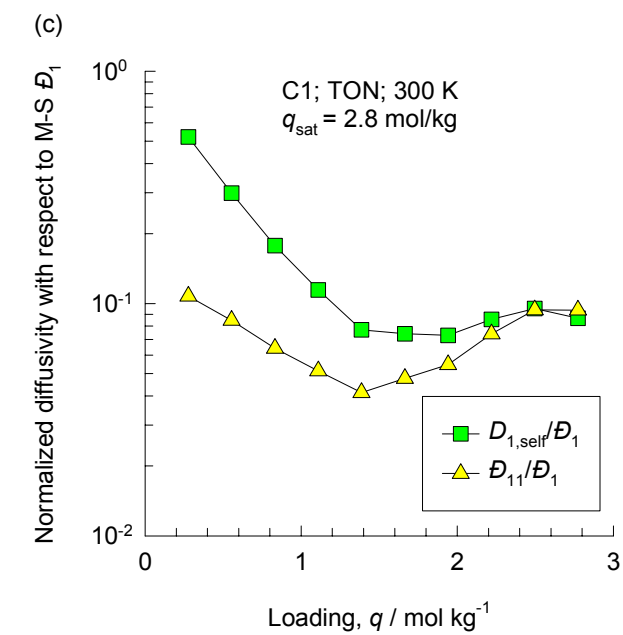
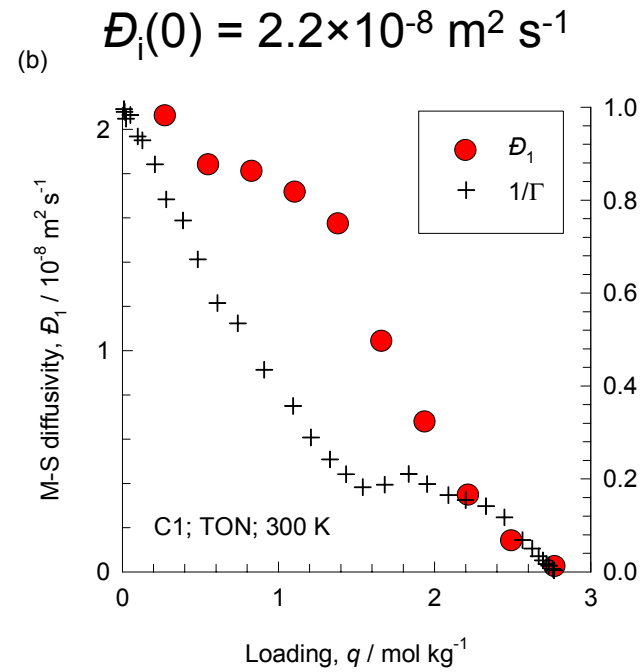
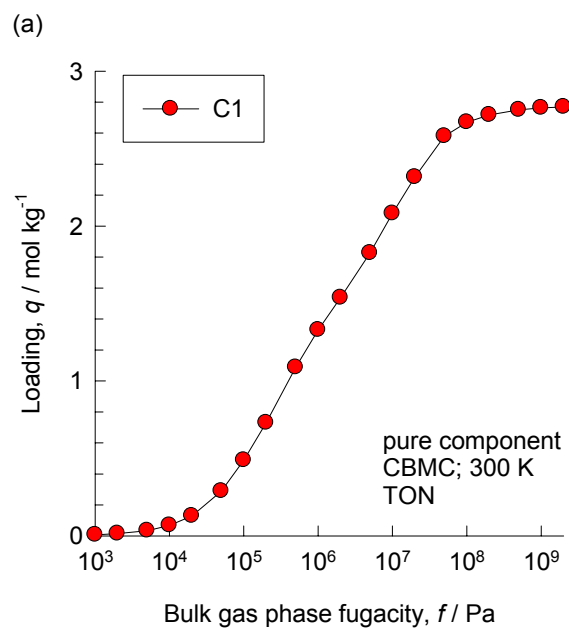
MTW



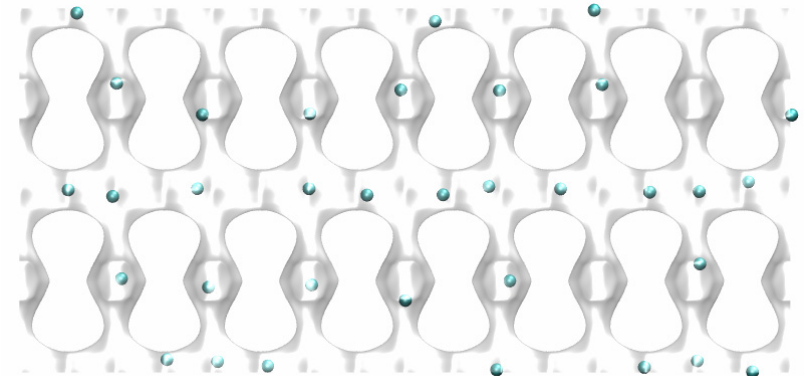
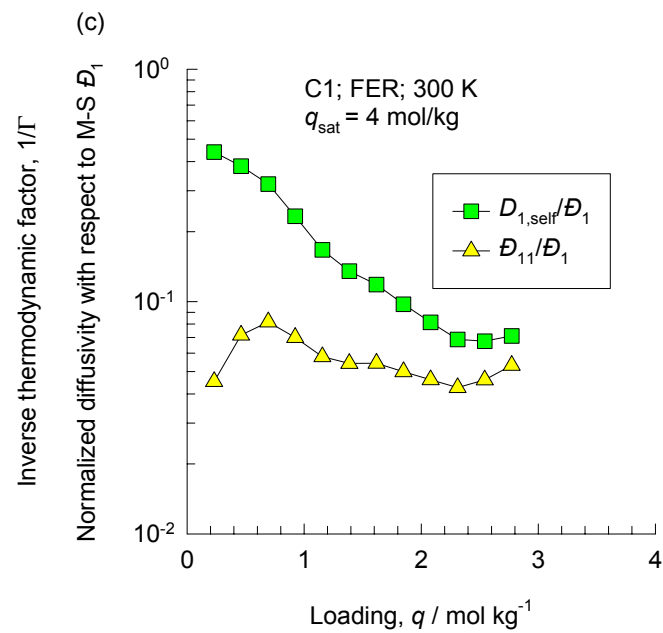
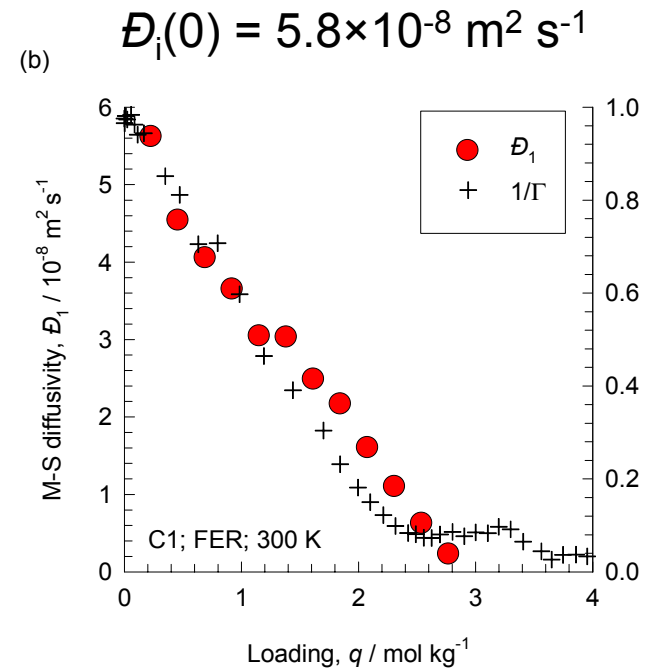
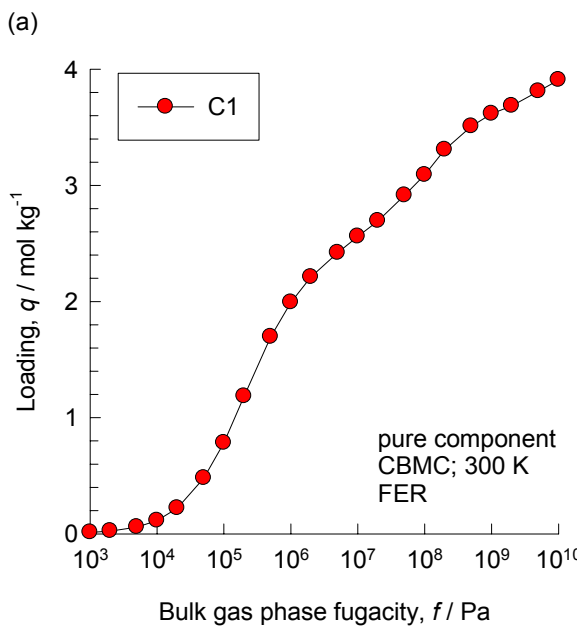
C1, 1000 kPa



TON

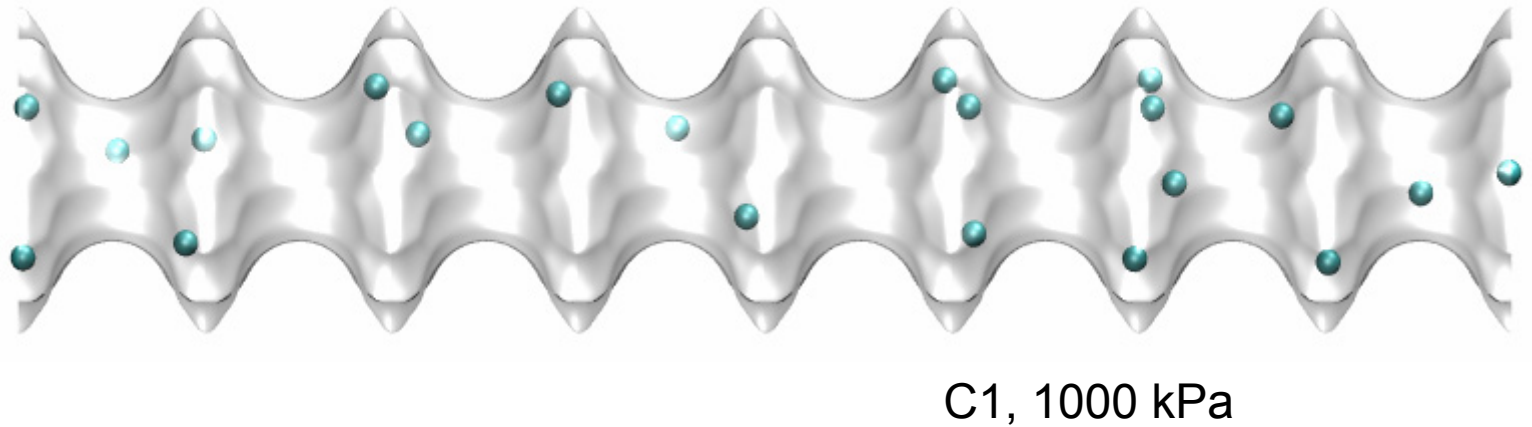


FER

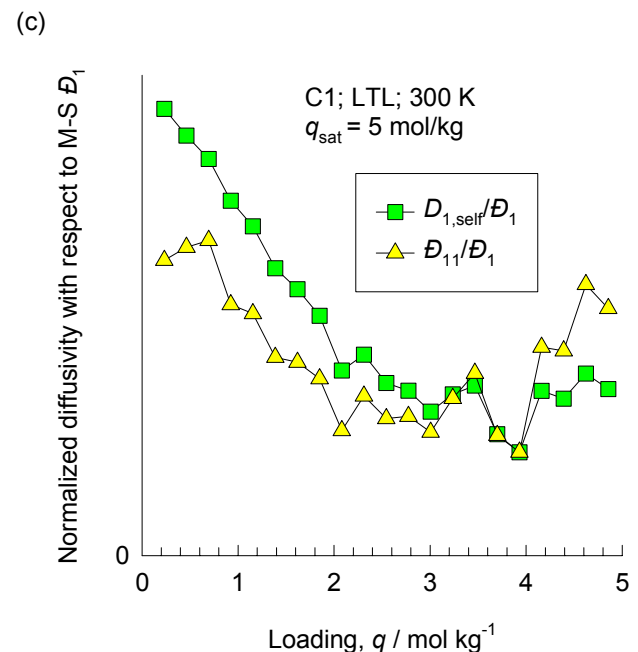
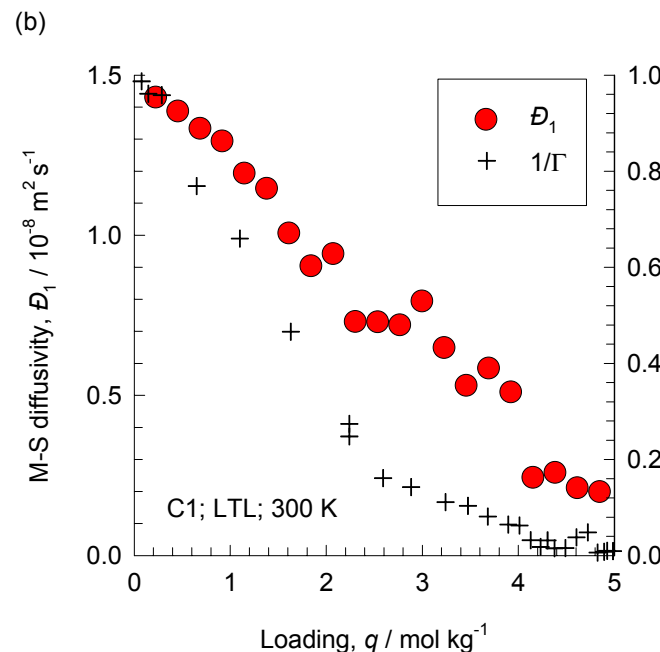
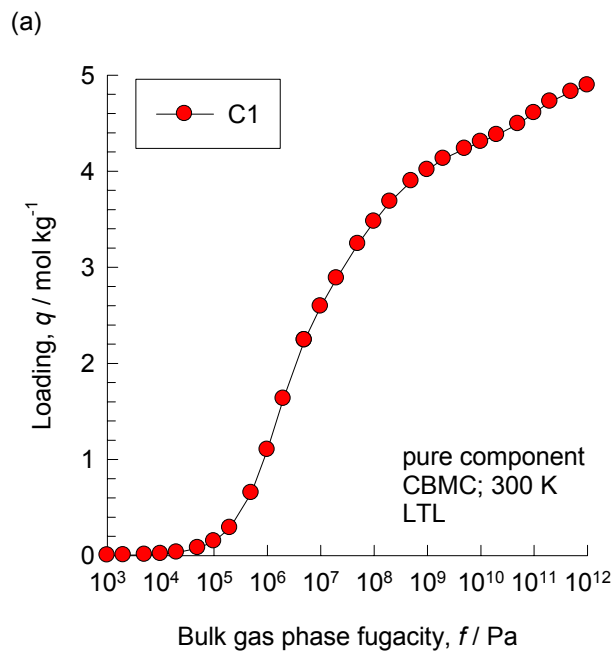


C1, 1000 kPa

LTL



$$\mathcal{D}_i(0) = 1.45 \times 10^{-8} \text{ m}^2 \text{ s}^{-1}$$



## Appendix C: Unary Permeation model

For steady-state diffusion  $x$ -directional across a zeolite membrane the flux  $N_i$  of a single component  $i$  is  $x$ -invariant

$$\frac{dN_i}{dx} = 0 \quad (1)$$

and can be obtained by integration of

$$N_i = -\rho D_i \frac{dq_i}{dx} \quad (2)$$

where  $D_i$  is the Fick diffusivity,  $\rho$  is the zeolite density, and  $q_i$  is the molar loading. The Fick diffusivity  $D_i$  is related to the Maxwell-Stefan (M-S) diffusivity  $D_i$  by

$$D_i = D_i \Gamma_i \quad (3)$$

where  $\Gamma_i$  is the thermodynamic factor defined by

$$\Gamma_i \equiv \frac{d \ln f_i}{d \ln q_i} = \frac{q_i}{f_i} \frac{df_i}{dq_i} \quad (4)$$

where  $f_i$  is the fugacity of species  $i$  in the gas phase.

Combining eqs (2), (3), and (4) we obtain

$$N_i = -\rho D_i \frac{q_i}{f_i} \frac{df_i}{dq_i} \frac{dq_i}{dx} = -\rho D_i \frac{q_i}{f_i} \frac{df_i}{dx} \quad (5)$$

The steady-state flux  $N_i$  can be obtained by integrating eq. (5) for the boundary conditions

$$x = 0; \quad f_i = f_{i,up} \quad (6)$$

$$x = \delta; \quad f_i = f_{i,down} \quad (7)$$

$$N_i = \frac{\rho}{\delta} \int_{f_{i,down}}^{f_{i,up}} D_i \frac{q_i}{f_i} df_i \quad (8)$$

where we retain the M-S diffusivity  $D_i$  within the integral sign to allow for the dependence of this diffusivity on the loadings  $q_i$ .

The simplest scenario for unary permeation is one in which the M-S diffusivity  $D_i$  is considered to be independent of the loading, and can be taken to be equal to the zero-loading limiting value

$$D_i = D_i(0) \quad \text{constant M - S diffusivity scenario} \quad (9)$$

In this case eq. (8) simplifies to

$$N_i = \frac{\rho D_i}{\delta} \int_{f_{i,down}}^{f_{i,up}} \frac{q_i}{f_i} df_i \equiv \frac{\rho D_i}{\delta} DF_i \quad (10)$$

where  $DF_i$  is the driving force for unary permeation across the membrane:

$$DF_i \equiv \int_{f_{i,down}}^{f_{i,up}} \frac{q_i}{f_i} df_i \quad (11)$$

Let us describe the sorption isotherm by a multi-site Langmuir isotherm with sites A, B, C.. with different strengths and capacities

$$q_i = \frac{q_{i,sat,A} b_{iA} f_i}{1 + b_{iA} f_i} + \frac{q_{i,sat,B} b_{iB} f_i}{1 + b_{iB} f_i} + \frac{q_{i,sat,C} b_{iC} f_i}{1 + b_{iC} f_i} + \dots \quad (12)$$

where  $q_{i,sat,A}$  and  $b_{iA}$  represent, respectively, the saturation capacity of site A, and its sorption strength.

Inserting eq. (12) into the integrand in eq. (11), and performing the analytic integration we obtain

$$DF_i = q_{i,sat,A} \ln \left( \frac{1 + b_{i,A} f_{i,up}}{1 + b_{i,A} f_{i,down}} \right) + q_{i,sat,B} \ln \left( \frac{1 + b_{i,B} f_{i,up}}{1 + b_{i,B} f_{i,down}} \right) + q_{i,sat,C} \ln \left( \frac{1 + b_{i,C} f_{i,up}}{1 + b_{i,C} f_{i,down}} \right) + \dots \quad (13)$$

Equation (13) implies that the dominant resistance is intracrystalline diffusion and that other resistances, such as that offered by the support, are negligible. In the more general case the M-S diffusivity  $D_i$  varies with the occupancy within the zeolite, defined by

$$\theta_i = \frac{q_i}{q_{i,sat}} \quad (14)$$

where  $q_{i,sat}$  is the total saturation capacity for species  $i$ , given by the sum of the saturation capacities of sites A, B, C,..

$$q_{i,sat} = q_{i,sat,A} + q_{i,sat,B} + q_{i,sat,C} + \dots \quad (15)$$

This occupancy dependence is caused by intermolecular forces (attraction or repulsion) that influence the energy barrier for diffusion. One model for the loading dependence of  $D_i$  is that due to Reed and Ehrlich<sup>1</sup>, that has applied to zeolites by Krishna et al<sup>2</sup>. In the Reed-Ehrlich model, the presence of neighboring molecules on a lattice is assumed to influence the jump frequencies of species  $i$  by a factor  $\phi_i = \exp\left(\frac{\delta E_i}{RT}\right)$ , where  $\delta E_i$  represents the reduction in the energy barrier for diffusion. This model leads to the following expression for the M-S diffusivity as a function of the fractional occupancy,

$$D_i = D_i(0) \frac{(1+\varepsilon_i)^{z-1}}{(1+\varepsilon_i/\phi_i)^z} \quad (16)$$

where  $z$  is the coordination number, representing the maximum number of nearest neighbours. The other parameters are defined as (see Krishna et al.<sup>2</sup> for more detailed discussions and derivations)

$$\varepsilon_i = \frac{(\beta_i - 1 + 2\theta_i)\phi_i}{2(1-\theta_i)}; \quad \beta_i = \sqrt{1 - 4\theta_i(1-\theta_i)(1-1/\phi_i)} \quad (17)$$

In the limiting case where there are no interactions between neighboring molecules

$$\delta E = 0; \quad \phi_i = 1; \quad \beta_i = 1; \quad \varepsilon_i = \frac{\theta_i}{1-\theta_i} \quad \text{no intermolecular interactions} \quad (18)$$

Eq. (16) reduces in this case

$$D_i = D_i(0)(1 - \theta_i) \quad \text{no intermolecular interactions} \quad (19)$$

To account for the loading dependence of the M-S diffusivity on the unary permeation flux we define the modified driving force

$$MDF_i \equiv \int_{f_{i,down}}^{f_{i,up}} \frac{(1 + \varepsilon_i)^{z-1}}{(1 + \varepsilon_i / \phi_i)^z} \frac{q_i}{f_i} df_i = \int_{f_{i,down}}^{f_{i,up}} \frac{(1 + \varepsilon_i)^{z-1}}{(1 + \varepsilon_i / \phi_i)^z} \left( \frac{q_{i,sat,A} b_{iA}}{1 + b_{iA} f_i} + \frac{q_{i,sat,B} b_{iB}}{1 + b_{iB} f_i} + \frac{q_{i,sat,C} b_{iC}}{1 + b_{iC} f_i} + \dots \right) df_i \quad (20)$$

The integration in eq. (20) has to be performed numerically. The unary permeation flux is then obtained as

$$N_i = \frac{\rho D_i(0)}{\delta} MDF_i \quad (21)$$

# Literature Cited

(1) Reed, D. A.; Ehrlich, G., Surface diffusion, atomic jump rates and thermodynamics, *Surf. Sci.* **1981**, *102*, 588-609.

(2) Krishna, R.; Paschek, D.; Baur, R., Modelling the occupancy dependence of diffusivities in zeolites, *Microporous Mesoporous Mater.* **2004**, *76*, 233-246.

# Nomenclature

$b_i$	Langmuir constant, $\text{Pa}^{-1}$
$D_i$	Fick diffusivity, $\text{m}^2 \text{s}^{-1}$
$D_i$	Maxwell-Stefan diffusivity of species $i$ , $\text{m}^2 \text{s}^{-1}$
$D_i(0)$	zero-loading M-S diffusivity of species $i$ , $\text{m}^2 \text{s}^{-1}$
$DF_i$	driving force for transport across membrane, $\text{mol kg}^{-1}$
$f_i$	fugacity of species $i$ , $\text{Pa}$
$MDF_i$	modified driving force for transport across membrane, $\text{mol kg}^{-1}$
$N_i$	molar flux of species $i$ across membrane, $\text{mol m}^{-2} \text{s}^{-1}$
$q_i$	molar loading, $\text{mol kg}^{-1}$
$q_{i,\text{sat}}$	saturation loading, $\text{mol kg}^{-1}$
$x$	distance coordinate for diffusion across membrane, $\text{m}$
$z$	coordination number, dimensionless

### ***Greek letters***

$\beta_i$	Reed-Ehrlich parameter, dimensionless
$\phi_i$	Reed-Ehrlich parameter, dimensionless
$\Gamma_i$	thermodynamic factor for pure component $i$ , dimensionless
$\delta$	thickness of zeolite membrane, m
$\delta E_i$	reduction in energy barrier for diffusion, J mol <sup>-1</sup>
$\varepsilon_i$	Reed-Ehrlich parameter, dimensionless
$\theta_i$	fractional occupancy of component $i$ , dimensionless
$\mu_i$	molar chemical potential, J mol <sup>-1</sup>
$\rho$	density of zeolite, kg m <sup>-3</sup>

### ***Subscripts***

A, B, C	referring to sites A, B, C,.. etc in multi-site Langmuir isotherm
down	referring to downstream conditions
sat	referring to saturation conditions
up	referring to upstream conditions

# Appendix D: Additional CH<sub>4</sub> and CO<sub>2</sub> permeation data analysis in SAPO-34 and DDR membranes

## 1. CH<sub>4</sub> permeation through SAPO-34 at 333K and 373 K

We first re-analyse the CH<sub>4</sub> permeation experiments of Li et al.<sup>1</sup> The GCMC simulation results for the sorption isotherm at 333 K are compared in Fig. 1a with the experimental isotherm reported by Li et al.<sup>2</sup> The experimental isotherm data is only available up to a pressure of 120 kPa, and there is good agreement with the GCMC simulations for this range. The GCMC simulated isotherms were fitted with the 3-site Langmuir model with parameters specified in Table 1. The saturation capacity  $q_{i,sat} = q_{i,sat,A} + q_{i,sat,B} + q_{i,sat,C} = 8.32$  mol/kg is significantly higher than the value obtained in the single-site Langmuir fit value of 2.7 mol/kg used by Li et al.<sup>2</sup> In Fig. 1b the permeation fluxes reported by Li et al.<sup>1</sup> are plotted against the  $DF_i$  calculated using

$$DF_i = q_{i,sat,A} \ln\left(\frac{1+b_{i,A}f_{i,up}}{1+b_{i,A}f_{i,down}}\right) + q_{sat,B} \ln\left(\frac{1+b_{i,B}f_{i,up}}{1+b_{i,B}f_{i,down}}\right) + q_{i,sat,C} \ln\left(\frac{1+b_{i,C}f_{i,up}}{1+b_{i,C}f_{i,down}}\right) \quad (1)$$

It is clear that a linear fit, with the line passing through the origin, is not possible, suggesting a break down of the constant  $D_i$  assumption. The values of the transport coefficients  $\rho D_i / \delta$  backed out from each experimental point using

$$N_i = \frac{\rho D_i}{\delta} DF_i \quad (2)$$

confirm that the  $D_i$  increases strongly with loading at the upstream face of the membrane; see Figure 1c. Also shown in Figure 1c are the MD simulation results of  $\bar{D}_i$  at 333 K. The continuous solid line in Figure 1c is obtained using the Reed and Ehrlich parameters listed in Table 2.

We can then calculate the *modified* driving force

$$MDF_i \equiv \int_{f_{i,down}}^{f_{i,up}} \frac{(1+\varepsilon_i)^{z-1}}{(1+\varepsilon_i/\phi_i)^z} \frac{q_i}{f_i} df_i = \int_{f_{i,down}}^{f_{i,up}} \frac{(1+\varepsilon_i)^{z-1}}{(1+\varepsilon_i/\phi_i)^z} \left( \frac{q_{i,sat,A} b_{iA}}{1+b_{iA} f_i} + \frac{q_{i,sat,B} b_{iB}}{1+b_{iB} f_i} + \frac{q_{i,sat,C} b_{iC}}{1+b_{iC} f_i} \right) df_i \quad (3)$$

The symbols in Figure 2 represent a plot of the permeation flux versus  $MDF_i$ . The straight line in Figure 2 is drawn using

$$N_i = \frac{\rho D_i(0)}{\delta} MDF_i \quad (4)$$

with the fitted value of the transport coefficients parameters listed in Table 3. The straight line obtained confirms the validity of the Reed and Ehrlich parameters obtained from MD simulations at 333 K.

The re-analyse the CH<sub>4</sub> permeation experiments of Li et al.<sup>1</sup> at 373 K follows an exactly parallel path; these results are presented in Figures 3 and Figure 4. CO<sub>2</sub> permeation through SAPO-34 at 373 K, 423 K, and 473 K

## 2. CO<sub>2</sub> permeation through CHA at 373 K, 423 K, and 473 K

The CO<sub>2</sub> permeation fluxes in CHA at 373 K are reported by Li et al.<sup>2</sup> We first determined the sorption isotherm at 373 K; these are presented in Fig. 5a. Also presented in Fig. 5a is the 3-site Langmuir fit with parameters listed in Table 1. The experimental isotherm data is only available up to a pressure of 120 kPa, and there is good agreement with the GCMC simulations for this range. The GCMC simulated isotherms were fitted with the 3-site Langmuir model with parameters specified in Table 1. The saturation capacity  $q_{i,sat} = q_{i,sat,A} + q_{i,sat,B} + q_{i,sat,C} = 10.4$  mol/kg is significantly higher than the value obtained in the single-site Langmuir fit value of 5 mol/kg used by Li et al.<sup>2</sup> A plot of the permeation fluxes reported by Li et al.<sup>2</sup> are plotted against the  $DF_i$  calculated using eq. (1); see Fig. 5b. The dependence of the flux  $N_i$  on  $DF_i$  is nearly linear. The values of the transport coefficients backed

out from each experimental point confirm that the  $D_i$  is practically constant with loading at the upstream face of the membrane; see Figure 5c. The MD simulated  $D_i$  is also plotted in Figure 5c (using the right y-axis); these data also show that they are nearly loading independent.

Figure 6 shows a plot of the pure component permeation selectivity calculated from the experimental fluxes of CO<sub>2</sub> and CH<sub>4</sub> in SAPO-34 at 373 K, calculated from

$$\alpha_{perm} = N_1/N_2 \quad (5)$$

Also plotted by the continuous solid line is the pure component sorption selectivity from the fitted pure component isotherms with parameter values listed in Table 1:

$$\alpha_{sorp} = q_{1,up}/q_{2,up} \quad (6)$$

Though the pure component sorption selectivity is practically constant, the experimental permeation selectivity decreases with increasing pressure. This decrease is entirely to be attributed to the increase in the transport coefficient of CH<sub>4</sub> as witnessed in Figure 3c.

The re-analyses of the CO<sub>2</sub> permeation experiments in SAPO-34 at 423 K and 473 K are presented in Figures 7 and 8. This shows, again, that the transport coefficients for CO<sub>2</sub> can be taken to be practically loading independent.

### 3. CH<sub>4</sub> and CO<sub>2</sub> permeation through DDR at 373 K

The re-analysis of the CH<sub>4</sub> permeation experiments of Tomita et al.<sup>3</sup> in DDR at 373 K are presented in Figures 9a, b and c. The sharp increase in the transport coefficients  $\rho D_i/\delta$ , backed out from the Tomita et al.<sup>3</sup> data with  $q_{i,up}$  is particularly noteworthy; see Figure 9c. Also shown in Figure 9c are the MD simulated  $D_i$ ; these MD simulation results could be fitted with the Reed and Ehrlich parameters listed in Table 2.

Figure 10 shows a plot of the permeation flux vs the modified driving force  $MDF_i$ . This plot is linear validating the assumed Reed and Ehrlich parameters obtained from MD simulation results. The straight

line in Figure 10 was drawn using eq (4) with the fitted values of the transport coefficients listed in Table 3.

The re-analysis of the CO<sub>2</sub> permeation experiments at 373 K are presented in Figures 11a,b and c. These results confirm the assumption that the transport coefficient for CO<sub>2</sub> may be assumed to be practically loading independent.

Figure 12 shows a plot of the pure component permeation selectivity calculated from the experimental fluxes of CO<sub>2</sub> and CH<sub>4</sub> in DDR at 373 K, calculated from eq (5). Also plotted by the continuous solid line is the pure component sorption selectivity from the fitted pure component isotherms with parameter values listed in Table 1. Though the pure component sorption selectivity is practically constant, the experimental permeation selectivity decreases with increasing pressure. This decrease is entirely to be attributed to the increase in the transport coefficient of CH<sub>4</sub> as witnessed in Figure 9c.

#### 4. Literature cited

- (1) Li, S.; Martinek, J. G.; Falconer, J. L.; Noble, R. D.; Gardner, T. Q., High-Pressure CO<sub>2</sub>/CH<sub>4</sub> separation using SAPO-34 membranes, *Ind. Eng. Chem. Res.* **2005**, *44*, 3220-3228.
- (2) Li, S.; Falconer, J. L.; Noble, R. D., SAPO-34 membranes for CO<sub>2</sub>/CH<sub>4</sub> separation, *J. Membr. Sci.* **2004**, *241*, 121-135.
- (3) Tomita, T.; Nakayama, K.; Sakai, H., Gas separation characteristics of DDR type zeolite membrane, *Microporous Mesoporous Mater.* **2004**, *68*, 71-75.

Table 1. Three-site Langmuir parameters for CH<sub>4</sub> and CO<sub>2</sub> in CHA and DDR. The saturation capacity  $q_{\text{sat}}$  has the units of mol kg<sup>-1</sup>. The Langmuir parameters  $b_i$ , have the units of Pa<sup>-1</sup>.

Zeolite	Molecule, Temperature	Three-Site Langmuir parameters					
		$b_{i,A}$	$q_{i,\text{sat},A}$	$b_{i,B}$	$q_{i,\text{sat},B}$	$b_{i,C}$	$q_{i,\text{sat},C}$
CHA	CH <sub>4</sub> , 300 K	1.72×10 <sup>-6</sup>	2.77	2.7×10 <sup>-8</sup>	4.16	9.0×10 <sup>-10</sup>	1.39
CHA	CH <sub>4</sub> , 333 K	9.0×10 <sup>-7</sup>	2.77	1.4×10 <sup>-8</sup>	4.16	4.0×10 <sup>-10</sup>	1.39
CHA	CH <sub>4</sub> , 373 K	4.53×10 <sup>-7</sup>	2.77	7.4×10 <sup>-9</sup>	4.16	2.1×10 <sup>-10</sup>	1.39
DDR	CH <sub>4</sub> , 373 K	3.5×10 <sup>-6</sup>	1.66	1.45×10 <sup>-8</sup>	1.66	2.7×10 <sup>-11</sup>	0.83
CHA	CO <sub>2</sub> , 300 K	5.21×10 <sup>-6</sup>	6.93	1.02×10 <sup>-7</sup>	1.73	1.17×10 <sup>-9</sup>	1.73
CHA	CO <sub>2</sub> , 373 K	5.24×10 <sup>-7</sup>	6.93	4.36×10 <sup>-9</sup>	1.73	1.09×10 <sup>-10</sup>	1.73
CHA	CO <sub>2</sub> , 423 K	1.88×10 <sup>-7</sup>	6.93	1.28×10 <sup>-9</sup>	1.73	3.84×10 <sup>-11</sup>	1.73
CHA	CO <sub>2</sub> , 473 K	1×10 <sup>-7</sup>	6.93	4.84×10 <sup>-10</sup>	1.73	1.6×10 <sup>-11</sup>	1.73
DDR	CO <sub>2</sub> , 373 K	7.5×10 <sup>-6</sup>	1.66	2.0×10 <sup>-6</sup>	1.66	1.2×10 <sup>-8</sup>	1.25

Table 2. Reed-Ehrlich parameters.

Zeolite	Molecule	Temperature	Saturation capacity, $q_{i,\text{sat}}$ / mol/kg	$D_i(0) / 10^{-8} \text{ m}^2 \text{ s}^{-1}$	Reed-Ehrlich model parameters	
					$z$	$\phi_i$
CHA	CH <sub>4</sub>	300 K	8.32	0.0029	6	$3.2 \exp(-0.7\theta)$
CHA	CH <sub>4</sub>	333 K	8.32	0.0038	6	$3.2 \exp(-0.7\theta)$
CHA	CH <sub>4</sub>	373 K	8.32	0.0053	6	$3.2 \exp(-0.7\theta)$
DDR	CH <sub>4</sub>	300 K	4.16	0.0000623	5	$6 \exp(-0.2\theta)$
DDR	CH <sub>4</sub>	373 K	4.16	0.00011	5	$6 \exp(-0.2\theta)$

Table 3. Fitted values of Transport Coefficients  $\rho D_i(0)/\delta$  with units of  $\text{kg m}^{-2} \text{s}^{-1}$ .

Zeolite	Molecule	Temperature	$\rho D_i(0)/\delta$
CHA	CH <sub>4</sub>	295 K	$1.4 \times 10^{-3}$
CHA	CH <sub>4</sub>	333 K	$2.3 \times 10^{-3}$
CHA	CH <sub>4</sub>	373 K	$4.5 \times 10^{-3}$
DDR	CH <sub>4</sub>	300 K	$1.84 \times 10^{-5}$
DDR	CH <sub>4</sub>	373 K	$8.36 \times 10^{-5}$
CHA	CO <sub>2</sub>	295 K	$1.54 \times 10^{-2}$
CHA	CO <sub>2</sub>	373 K	$4.45 \times 10^{-2}$
CHA	CO <sub>2</sub>	423 K	$7.85 \times 10^{-2}$
CHA	CO <sub>2</sub>	473 K	$10.03 \times 10^{-2}$
DDR	CO <sub>2</sub>	300 K	$1.03 \times 10^{-2}$
DDR	CO <sub>2</sub>	373 K	$1.683 \times 10^{-2}$

## 5. Captions for Figures

Figure 1. (a) Sorption isotherm data for CH<sub>4</sub> in CHA or SAPO-34 at 333 K. The GCMC simulation results are compared with the experimental data of Li et al.<sup>2</sup> Also shown by the continuous line is the 3-site Langmuir fit of the GCMC simulated isotherm. (b) The experimental data<sup>1</sup> on permeation flux of CH<sub>4</sub> is plotted against the driving force  $DF_i$ , calculated from eq. (1). (c) Transport coefficients  $\rho D_i / \delta$ , backed out using eq. (2), are shown as a function of the loadings at the upstream face of the membrane,  $q_{i,up}$ . Also plotted in (c) are the MD simulated  $D_i$  (right y-axis). The continuous solid line in (c) is drawn with the Reed and Ehrlich parameters listed in Table 2.

Figure 2. The experimental data<sup>1</sup> on permeation flux of CH<sub>4</sub> in CHA at 333 K is plotted against the modified driving force  $MDF_i$ , calculated from eq. (3). The straight line is obtained with the value of  $\rho D_i(0) / \delta$  as given in Table 3.

Figure 3. (a) Sorption isotherm data for CH<sub>4</sub> in CHA or SAPO-34 at 373 K. The GCMC simulation results are compared with the experimental data of Li et al.<sup>2</sup> Also shown by the continuous line is the 3-site Langmuir fit of the GCMC simulated isotherm. (b) The experimental data<sup>1</sup> on permeation flux of CH<sub>4</sub> is plotted against the driving force  $DF_i$ , calculated from eq. (1). (c) Transport coefficients  $\rho D_i / \delta$ , backed out using eq. (2), are shown as a function of the loadings at the upstream face of the membrane,  $q_{i,up}$ . Also plotted in (c) are the MD simulated  $D_i$  (right y-axis). The continuous solid line in (c) is drawn with the Reed and Ehrlich parameters listed in Table 2.

Figure 4. The experimental data<sup>1</sup> on permeation flux of CH<sub>4</sub> in CHA at 373 K is plotted against the modified driving force  $MDF_i$ , calculated from eq. (3). The straight line is obtained with the value of  $\rho D_i(0)/\delta$  as given in Table 3.

Figure 5. (a) Sorption isotherm data for CO<sub>2</sub> in CHA or SAPO-34 at 373 K. The GCMC simulation results are compared with the experimental data of Li et al.<sup>2</sup> Also shown by the continuous line is the 3-site Langmuir fit of the GCMC simulated isotherm. (b) The experimental data<sup>1</sup> on permeation flux of CO<sub>2</sub> is plotted against the driving force  $DF_i$ , calculated from eq. (1). The straight line is obtained with the value of  $\rho D_i(0)/\delta$  as given in Table 3. (c) Transport coefficients, backed out using eq. (2), are shown as a function of the loadings at the upstream face of the membrane,  $q_{i,up}$ . Also plotted in (c) are the MD simulated  $D_i$  (right y-axis).

Figure 6. Experimental permeation selectivity,  $\alpha_{perm}$ , along with calculated sorption selectivity,  $\alpha_{sorpt}$ , as a function of the upstream feed fugacity for pure component permeation of CO<sub>2</sub> and CH<sub>4</sub> across SAPO-34 membrane at 373 K. The dashed line are the calculations of using  $\alpha_{perm}$  eqs (4) and (5) with values of fitted transport coefficients from Table 3.

Figure 7. (a) Sorption isotherm data for CO<sub>2</sub> in CHA at 423 K compaed with data for SAPO-34 at 416 K. The GCMC simulation results are compared with the experimental data of Li et al.<sup>2</sup> Also shown by the continuous line is the 3-site Langmuir fit of the GCMC simulated isotherm. (b) The experimental data<sup>1</sup> on permeation flux of CO<sub>2</sub> is plotted against the driving force  $DF_i$ , calculated from eq. (1). The straight line is obtained with the value of  $\rho D_i(0)/\delta$  as given in Table 3. (c) Transport coefficients,

backed out using eq. (2), are shown as a function of the loadings at the upstream face of the membrane,  $q_{i,up}$ . Also plotted in (c) are the MD simulated  $D_i$  (right y-axis).

Figure 8. (a) Sorption isotherm data for CO<sub>2</sub> in CHA or SAPO-34 at 473 K. The GCMC simulation results are compared with the experimental data of Li et al.<sup>2</sup> Also shown by the continuous line is the 3-site Langmuir fit of the GCMC simulated isotherm. (b) The experimental data<sup>1</sup> on permeation flux of CO<sub>2</sub> is plotted against the driving force  $DF_i$ , calculated from eq. (1). The straight line is obtained with the value of  $\rho D_i(0)/\delta$  as given in Table 3. (c) Transport coefficients, backed out using eq. (2), are shown as a function of the loadings at the upstream face of the membrane,  $q_{i,up}$ . Also plotted in (c) are the MD simulated  $D_i$  (right y-axis).

Figure 9. (a) Sorption isotherm data for CH<sub>4</sub> in DDR at 373 K. Also shown by the continuous line is the 3-site Langmuir fit of the GCMC simulated isotherm. (b) The experimental data<sup>3</sup> on permeation flux of CH<sub>4</sub> is plotted against the driving force  $DF_i$ , calculated from eq. (1). (c) Transport coefficients,  $\rho D_i / \delta$  backed out using eq. (2), are shown as a function of the loadings at the upstream face of the membrane,  $q_{i,up}$ . Also plotted in (c) are the MD simulated  $D_i$  (right y-axis). The continuous solid line in (c) is drawn with the Reed and Ehrlich parameters listed in Table 2.

Figure 10. The experimental data<sup>1</sup> on permeation flux of CH<sub>4</sub> in DDR at 373 K is plotted against the modified driving force  $MDF_i$ , calculated from eq. (3). The straight line is obtained with the value of  $\rho D_i(0)/\delta$  as given in Table 3.

Figure 11. (a) Sorption isotherm data for CO<sub>2</sub> in DDR at 373 K. Also shown by the continuous line is the 3-site Langmuir fit of the GCMC simulated isotherm. (b) The experimental data<sup>3</sup> on permeation flux of CO<sub>2</sub> is plotted against the driving force  $DF_i$ , calculated from eq. (1). The straight line in (b) is obtained with  $\rho D_i / \delta$  indicated in Table 3. (c) Transport coefficients, backed out using eq. (2), are shown as a function of the loadings at the upstream face of the membrane,  $q_{i,up}$ . Also plotted in (c) are the MD simulated  $D_i$  (right y-axis).

Figure 12. Experimental permeation selectivity,  $\alpha_{perm}$ , along with calculated sorption selectivity,  $\alpha_{sorpt}$ , as a function of the upstream feed fugacity for pure component permeation of CO<sub>2</sub> and CH<sub>4</sub> across DDR membrane at 373 K. The dashed line are the calculations of using  $\alpha_{perm}$  eqs (4) and (5) with values of fitted transport coefficients from Table 3.

Figure 1

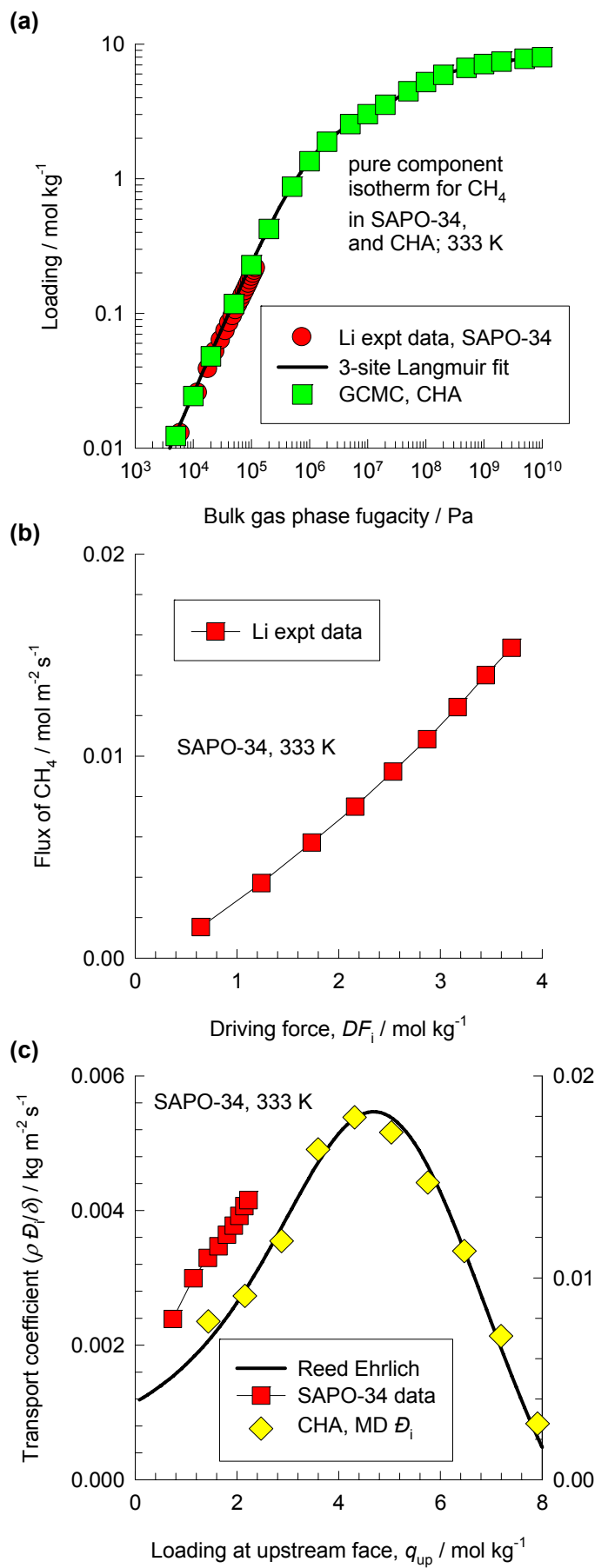


Figure 2

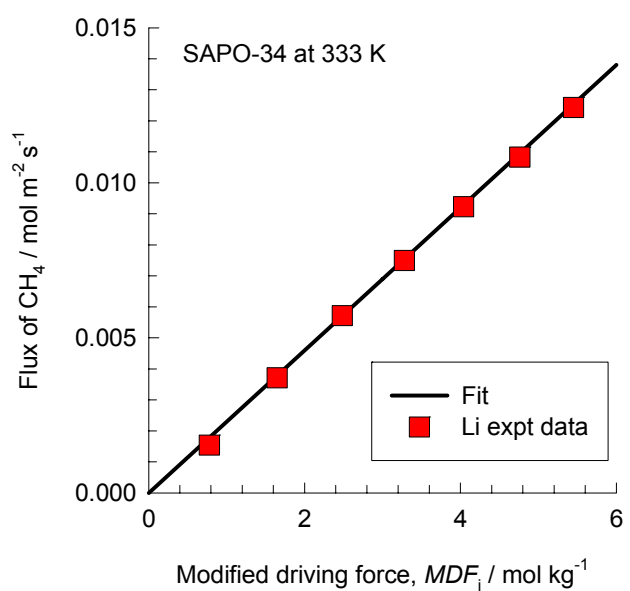


Figure 3

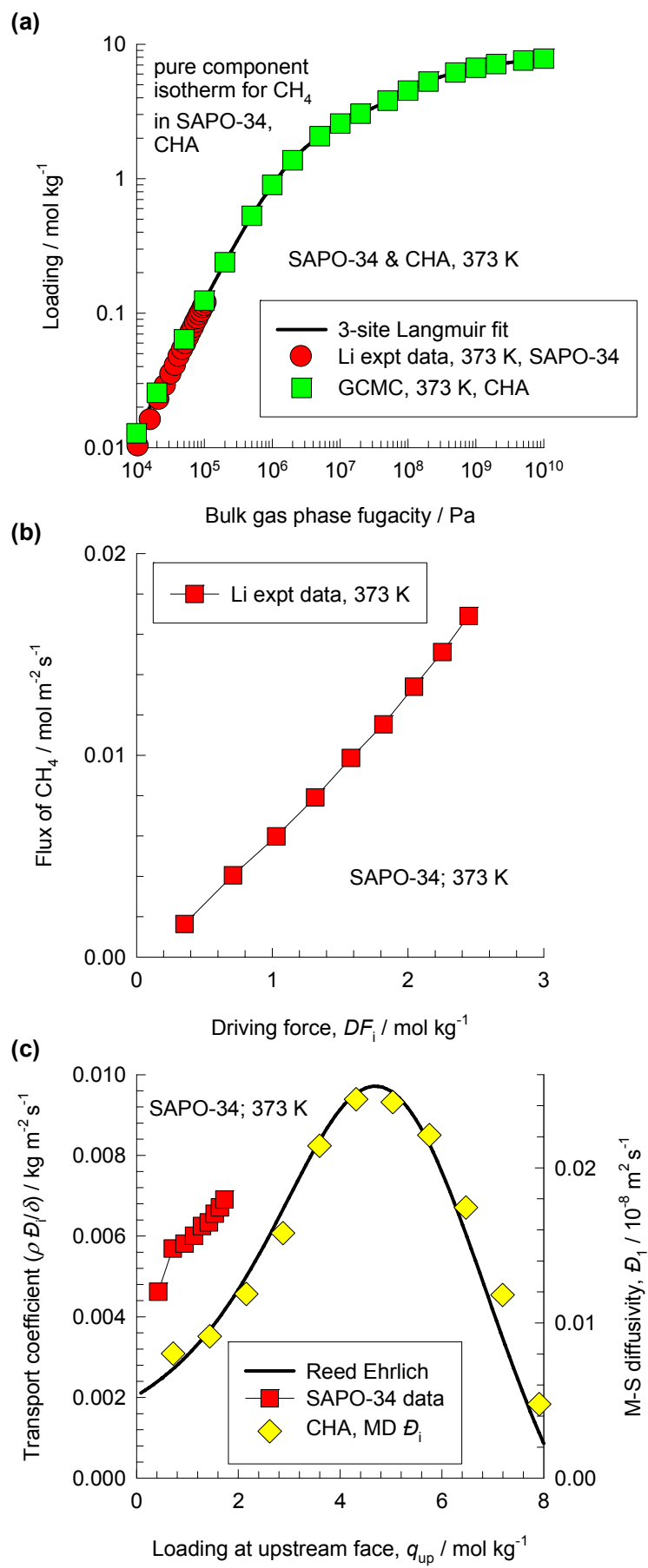


Figure 4

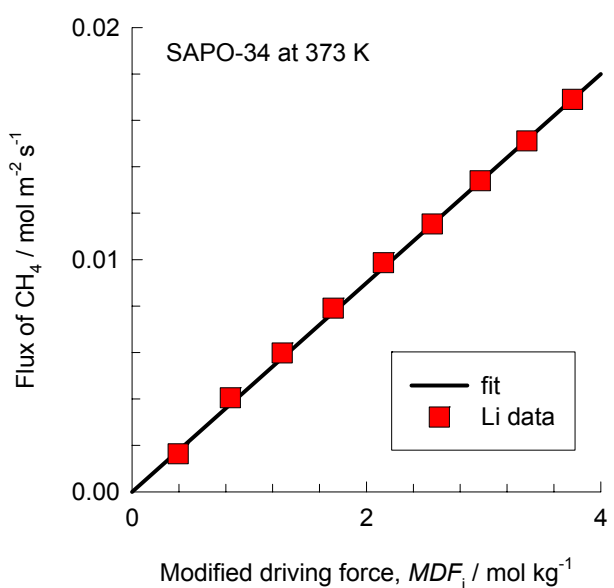


Figure 5

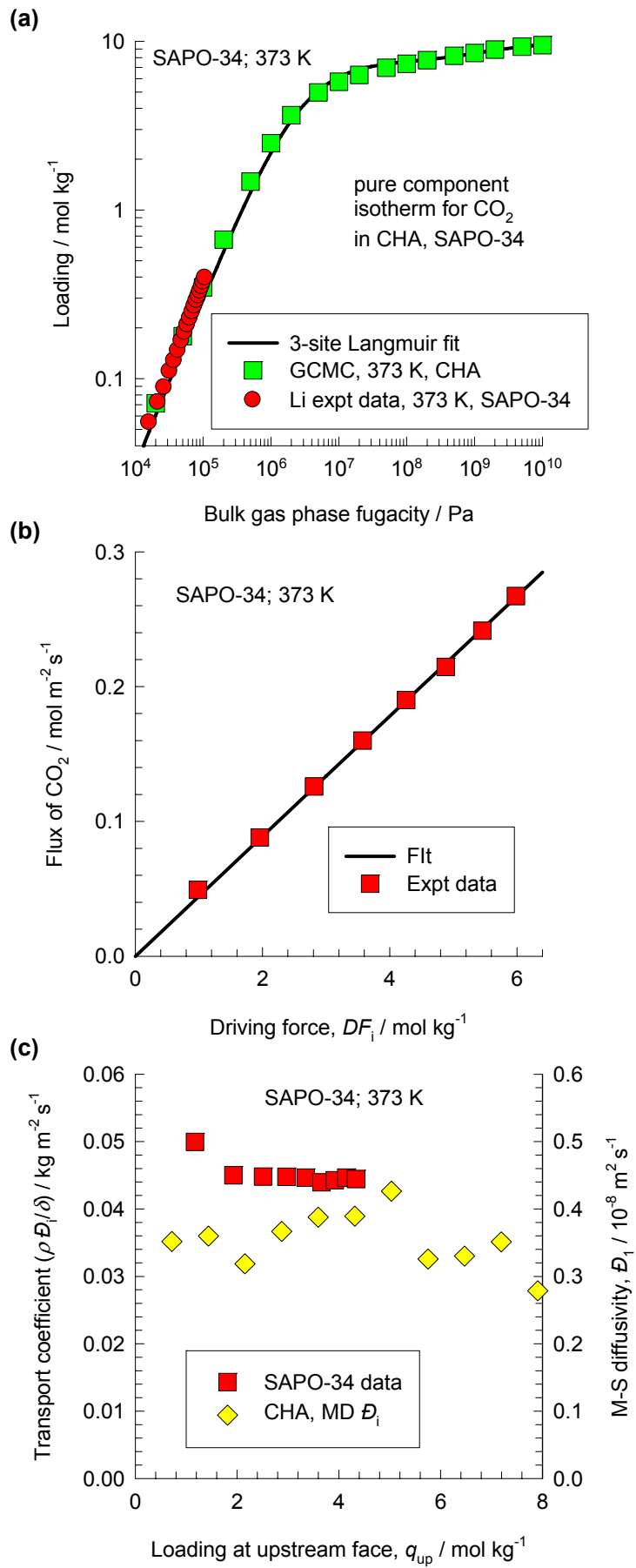


Figure 6

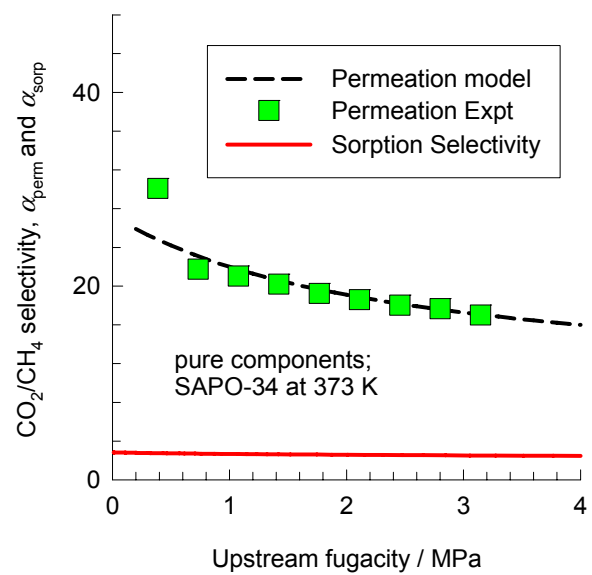


Figure 7

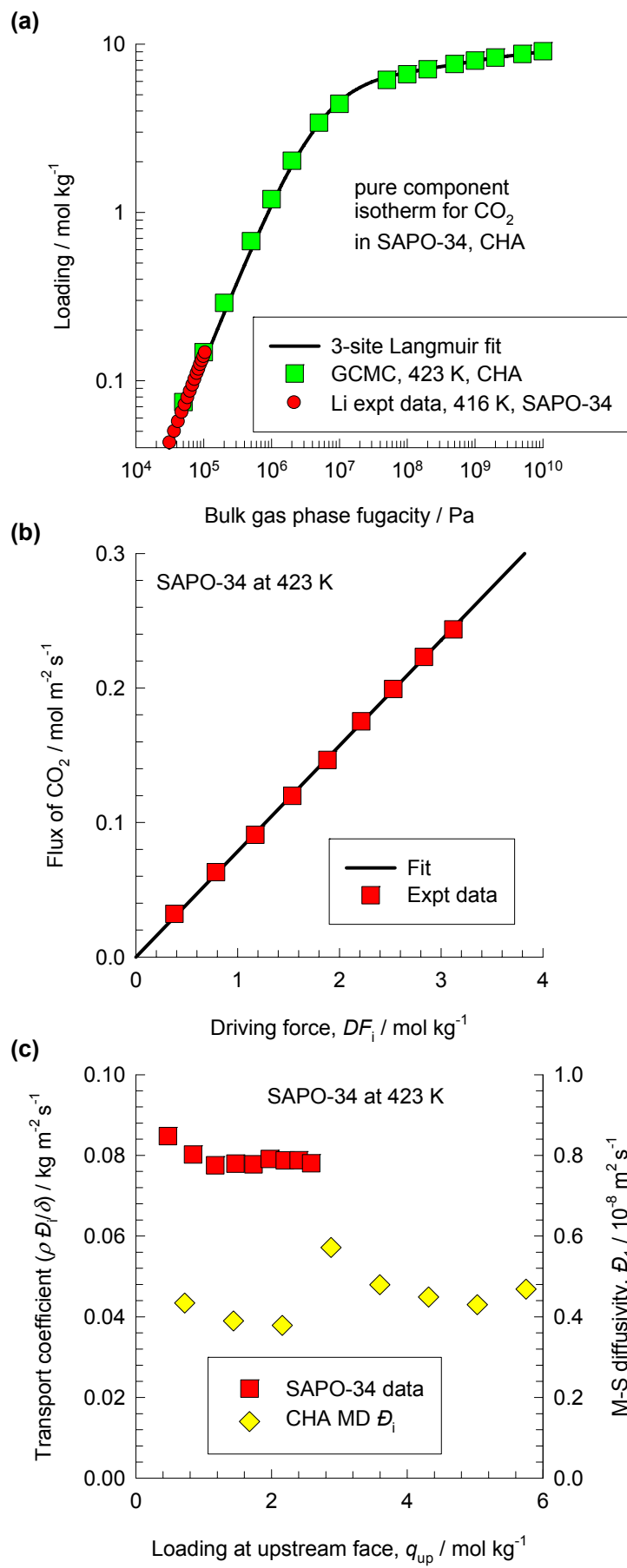


Figure 8

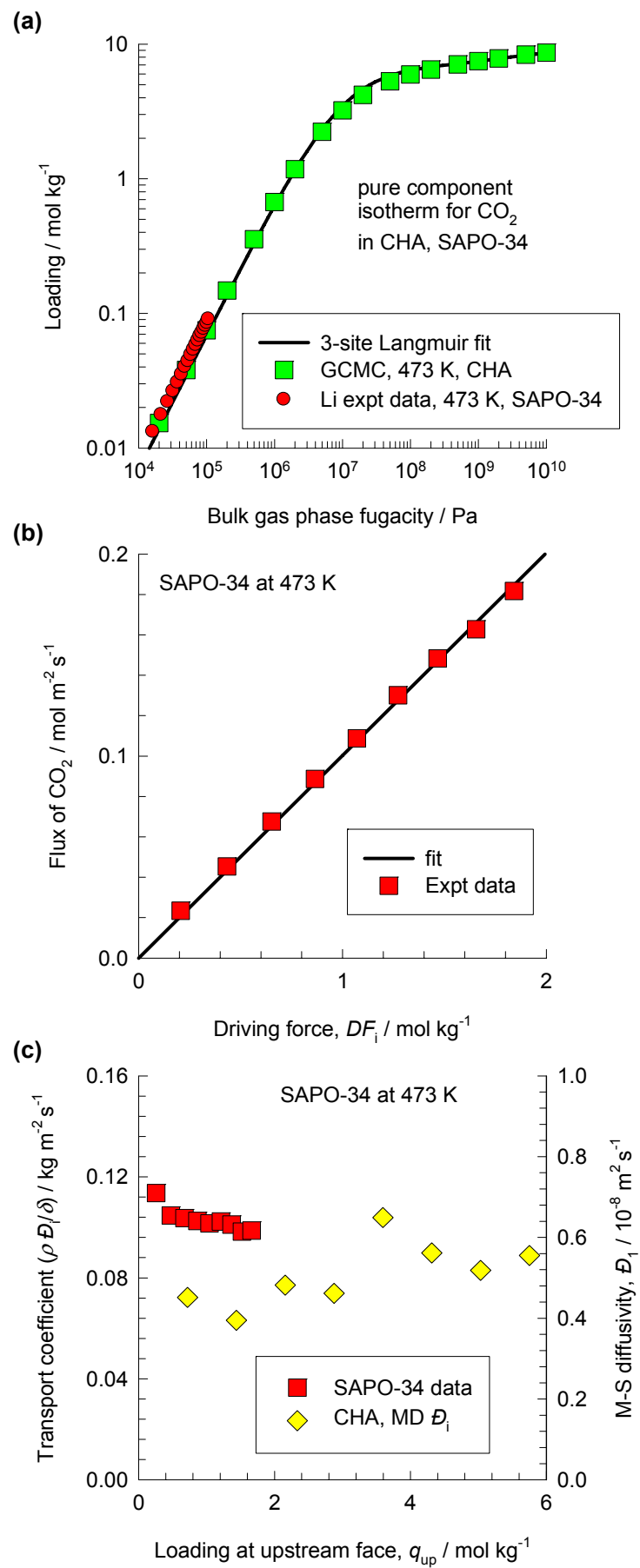


Figure 9

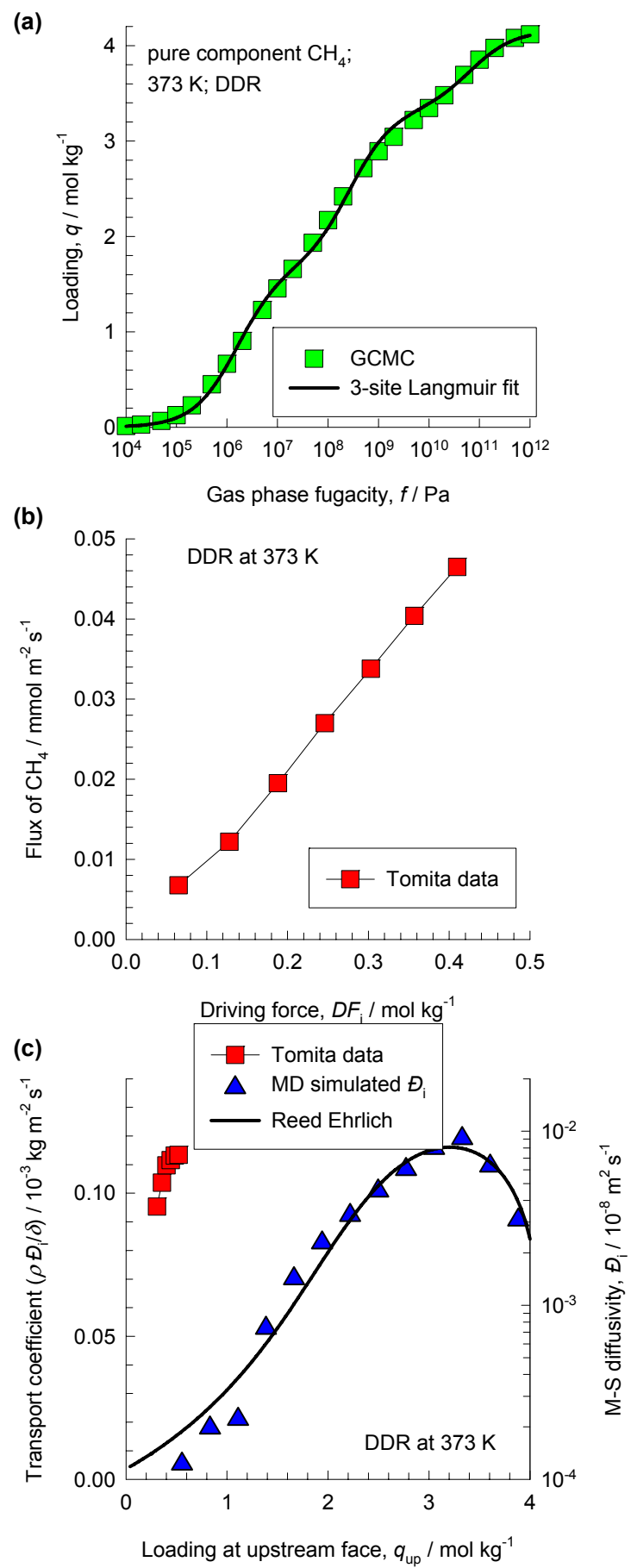


Figure 10

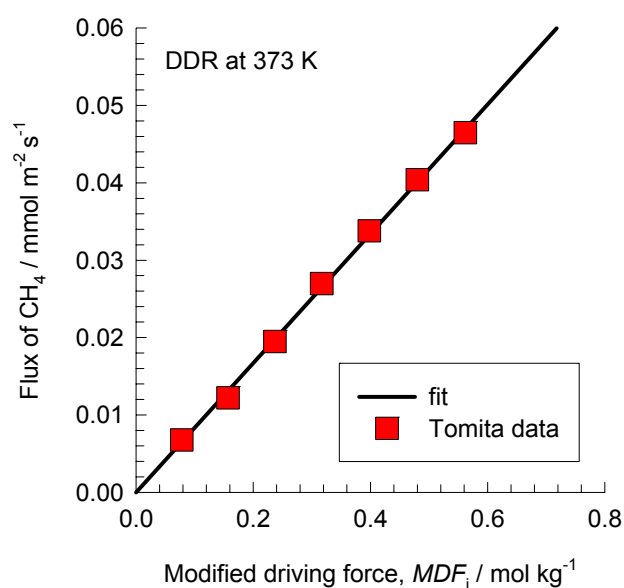


Figure 11

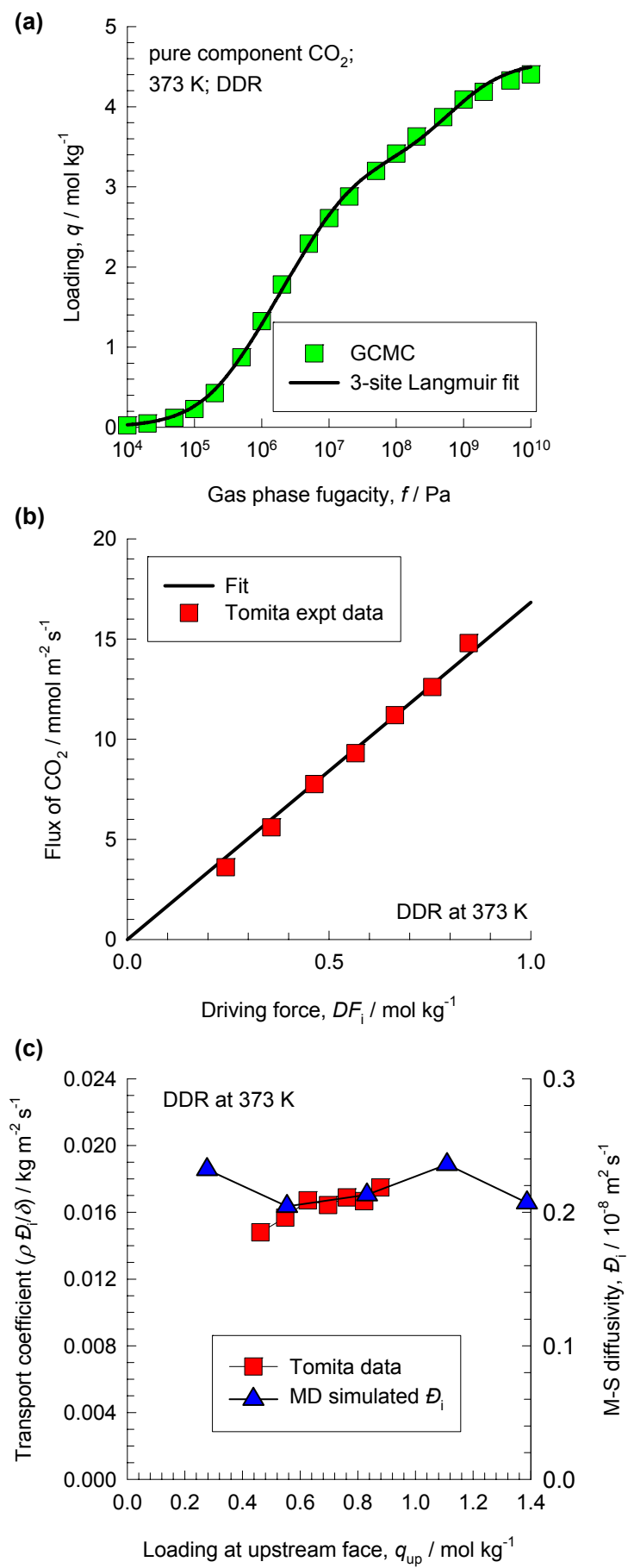


Figure 12

